Journal of Modeling & Simulation in Electrical & Electronics Engineering (MSEEE)

Semnan University

Volume 5, Issue 4 - Serial Number 22, December 2025, Pages 1-53

Contents

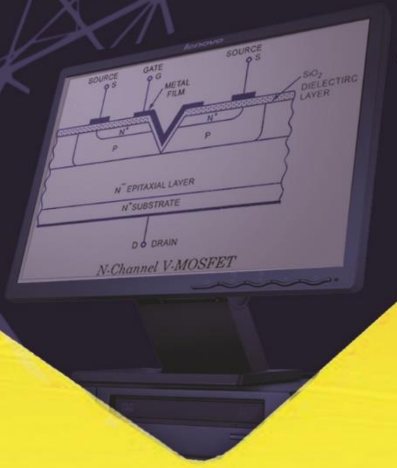

- **Publisher**
  Semnan University Press

- **Frequency** Quarterly
- **Online ISSN** 2821-0786

Editor’s Note

Journal of Modeling & Simulation in Electrical and Electronics Engineering

The *Journal of Modeling & Simulation in Electrical and Electronics Engineering* is a key platform for the advancement of research in electrical and electronics engineering. Whether we are developing reliable power systems, designing efficient electronic circuits, or analyzing complex electromagnetic environments, these tools allow us to predict performance, reduce risk, and optimize solutions long before they are implemented in the real world.

In this issue, we highlight the growing importance of simulation-driven engineering. Our articles explore the practical methods, software tools, and analytical approaches that support engineers in tackling today’s challenges—from system-level modeling and control design to circuit behavior analysis and emerging digital-twin applications.

As technology evolves and engineering problems become more interdisciplinary, the ability to model accurately and simulate effectively becomes even more essential. We hope the content in this edition encourages deeper understanding, inspires innovation, and strengthens the connection between theory, experimentation, and practical application.

Thank you for your continued support and engagement. Your feedback and participation help us maintain the quality and relevance of this publication.

Sincerely,

Editor-in-Chief MSEEE

Contents

Journal of Modeling & Simulation in Electrical & Electronics Engineering Vol 5 (4). 1-8.

Semnan University

Journal of Modeling & Simulation in Electrical & Electronics Engineering (MSEEE)

Journal homepage: **https://mseee.semnan.ac.ir/**

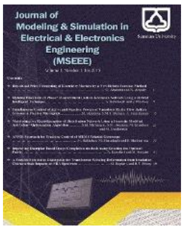

ISSN: 2821-0786

Design and Validation of a Pressure-Based Insole for the Quantitative Assessment of Gait Abnormalities

Maryam Farivar[1*], Hadi Soltanizadeh[2] and Mohammad Zahrayee[3]

***Abstract*—This study presents the design and validation of a wearable in-shoe system for real-time monitoring and quantitative analysis of plantar pressure distribution during walking. The system incorporates ten force-sensitive resistor (FSR) sensors strategically placed at key anatomical regions of each foot, enabling high-resolution pressure mapping. Data acquisition and wireless transmission are managed via an ESP32 microcontroller using TCP/IP protocol, with onboard microSD storage for redundancy. A custom graphical user interface (GUI), developed in Delphi, enables live visualization and recording. It also supports signal processing techniques, including dynamic time warping (DTW) for temporal alignment and signal averaging for noise reduction. Experimental trials were conducted on four adult participants (aged 22–45), including one individual with a normal gait and three with abnormal patterns, such as internal rotation, external rotation, and supination. Each participant completed multiple walking trials on a treadmill at a constant speed for a duration of 1 minute under standardized footwear conditions. The results confirmed that the system achieved high accuracy in distinguishing gait abnormalities, validated through quantitative metrics and visual pressure profiles. The proposed system provides a low-cost, portable, and clinically relevant solution for early detection of gait disorders and long-term rehabilitation monitoring. Its modular architecture and real-time performance demonstrate its potential as an effective tool for both clinical and remote rehabilitation monitoring.**

***Index Terms*--biomechanics, DTW, FSR sensor, Gait Analysis, Plantar Pressure Distribution, Postural Disorders, Rehabilitation Monitoring, Wearable Systems, Wireless Sensor Networks, Motion Impairment Detection**

NOMENCLATURE

FSR	Force Sensitive Resistor
PCA	Principal Component Analysis
SVM	Support Vector Machine
DTW	Dynamic Time Warping

I. INTRODUCTION

GAIT abnormalities are often early indicators of underlying neuromuscular, orthopedic, or metabolic disorders. If left undetected, they can lead to chronic pain, reduced mobility, and increased healthcare costs. Early diagnosis and continuous monitoring of gait patterns are therefore essential for effective rehabilitation and prevention of secondary injuries [1]. Among various biomechanical parameters, plantar pressure distribution provides valuable insights into foot function and postural control during walking.

Since the introduction of plantar pressure measurement systems in the 1960s [2], technological advancements have enabled more precise and dynamic assessment of gait. In-shoe pressure sensors, particularly force-sensitive resistors

---

Received; 2025-05-24 Revised; 2025-08-23 Accepted; 2025-09-24

[1] .Technical and Vocational Training Organization, Isfahan, Iran.
[2] .Electrical and Computer Engineering Faculty, Semnan University, Semnan, Iran.
[3] .Shahid Beheshti University, Medical Science, Tehran, Iran.

- Corresponding author Email: farivar_maryam@semnan.ac.ir

Cite this article as:
Farivar, M., Soltanizadeh, H, and Zahrayee, M. (2025). Design and Validation of a Pressure-Based Insole for the Quantitative Assessment of Gait Abnormalities. *Journal of Modeling & Simulation in Electrical & Electronics Engineering (MSEEE), 5*(4), 1-8.

DOI:https://doi.org/10.22075/MSEEE.2025.37831.1214

(FSRs), have proven effective in capturing gait-related data in both clinical and non-clinical environments [3].

Factors such as age, neuromuscular conditions, joint pathologies, and walking speed influence gait dynamics. Moreover, plantar pressure distribution depends on foot structure and postural control, playing a vital role in gait evaluation. The gait cycle encompasses multiple stages, beginning with heel strike and continuing until the same foot returns to ground contact (Fig. 1) [1], [4], [5].

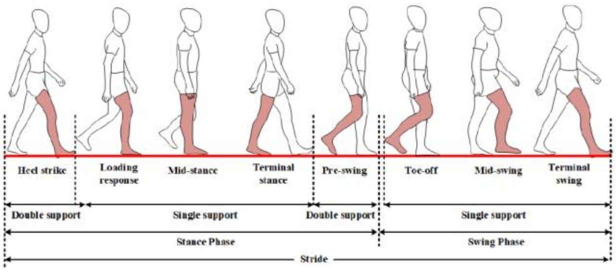

Fig. 1. A stride consists of multiple actions of the legs and feet [1]

Continuous gait monitoring, especially during rehabilitation, can accelerate recovery and reduce the risk of further injury. Pressure-sensing systems have been widely applied to assess motor impairments such as flatfoot, foot deformities, and neuropathies. However, many existing systems suffer from limitations, including bulky design, low accuracy, high energy consumption, and dependence on laboratory-grade setups [5].

In addition to hardware design, plantar pressure sensors can capture the distribution of forces across the foot in both static and dynamic conditions. The collected data can be analyzed using machine learning techniques to extract patient-specific patterns and strategies [6].

To address these challenges, we propose a lightweight, low-cost, and portable in-shoe system for real-time gait analysis. Unlike commercial platforms that often require specialized environments and complex configurations, our system is designed for ease of use in everyday settings. It operates reliably on flat surfaces or treadmills, with the latter offering speed consistency for enhanced measurement accuracy. The system uses a standardized shoe and elastic upper to minimize variability caused by footwear differences, ensuring consistent gait data across participants. Compared to existing commercial systems, which often require laboratory-grade setups and trained personnel, our platform emphasizes accessibility and ease of deployment in real-world scenarios.

Our platform integrates ten FSR sensors per insole, strategically positioned at key anatomical locations to capture high-resolution pressure data. Data acquisition and wireless transmission are managed via an ESP32 microcontroller using TCP/IP protocol, with onboard microSD storage for redundancy. A custom graphical user interface (GUI), developed in Delphi, enables live visualization, recording, and signal processing—including dynamic time warping (DTW) for temporal alignment and signal averaging for noise reduction.

This study presents the design, implementation, and experimental validation of the proposed system, highlighting its potential for clinical gait assessment, remote rehabilitation monitoring, and early diagnosis of movement disorders. The system offers several key features:

- Real-time data acquisition and analysis;
- Simultaneous measurement of both feet for bilateral gait analysis;
- Dynamic data collection during natural walking or treadmill use;
- Thin and lightweight insoles that do not interfere with walking;
- A custom-designed printed circuit board (PCB) with embedded sensors, eliminating wiring to enhance durability, data precision, and user safety;
- A compact electronics module mounted on the front of the shoe to avoid discomfort;
- High-speed wireless data transmission via Wi-Fi for user convenience;
- Intuitive usability without the need for user training;
- Usability in non-laboratory and non-clinical settings;
- An adjustable, elastic upper design accommodating men’s shoe sizes 39 to 43.

Compared to existing commercial insoles and laboratory-grade pressure mats, which often suffer from high cost, limited portability, dependence on controlled environments, and proprietary licensed software, our system represents a significant advancement in usability and accessibility. It eliminates the need for specialized equipment or trained personnel, supports real-time bilateral gait analysis, and enables remote monitoring in everyday settings. By combining lightweight hardware, standardized footwear, and a fully customizable and intuitive software platform that can be tailored to meet the specific needs of each patient, individual user, or intended usage environment, the proposed platform addresses key limitations of previous systems—namely cost, bulkiness, data inconsistency, restricted deployment, and software accessibility—making it a practical and scalable solution for clinical and home-based rehabilitation.

II. RESEARCH OVERVIEW

Numerous studies have investigated plantar pressure measurement systems for applications such as gait analysis, detection of foot abnormalities, and rehabilitation monitoring. Over the years, these systems have progressed from simple wired configurations to advanced wireless platforms incorporating integrated sensors and intelligent algorithms. This section provides a structured overview of major developments in the field, emphasizing technological innovations, diagnostic applications, and the growing role of machine learning techniques. By reviewing existing approaches and their limitations, we highlight the motivation for the proposed system and its anticipated contributions to both clinical practice and remote gait assessment.

The following subsections present a categorized review of prior research, organized thematically to highlight historical milestones, technological innovations, and diagnostic methodologies relevant to plantar pressure analysis and gait assessment.

A. Historical Evolution of In-shoe Systems

Applications of plantar pressure measurement date back to 1963, when Bowman and Brend used basic devices to assess footwear in patients with leprosy [2]. Early systems were wired and limited in mobility. In 1997, Lawrence and Schmidt introduced the first wireless in-shoe system for analyzing gait in both healthy and paraplegic individuals. A persistent challenge in these systems has been sensor slippage, emphasizing the need for precise sensor placement [7].

B. Commercial Systems and Limitations

Advanced commercial platforms, such as Pedar and Tekscan, offer high-resolution data and robust performance. However, their high cost, reliance on numerous sensors, and need for controlled environments limit their accessibility and scalability. These systems are often confined to laboratory settings and require trained personnel, making them impractical for widespread clinical or home-based use.

C. Emergence of FSR-Based Solutions

Force-sensitive resistors (FSRs) have gained attention as a cost-effective alternative for plantar pressure measurement. Studies have demonstrated their stability under static conditions and feasibility in low-cost setups using FSR406, Arduino, and LCD modules [8]. For example, Wei-Chun Hsu et al. used five FSR sensors to correlate plantar pressure with the Arch index, showing strong performance in both static and dynamic conditions [9].

D. Foot Arch Classification and Pressure Mapping

Several studies have explored detecting foot arch types (flat, normal, high). One investigation combined plantar pressure data with webcam images for flatfoot analysis. Another study examined how arch types influence pressure distribution during running, revealing increased heel pressure at a higher speed [10]. A stair-climbing study showed unexpected lateral pressure shifts in flat-footed individuals, suggesting compensatory mechanisms for balance [11].

E. Machine Learning Integration in Smart Insoles

Recent systems have integrated machine learning algorithms to enhance diagnostic capabilities. For instance, a smart insole with seven FSRs and a BLE transmission achieved 63% accuracy in pressure pattern classification [12]. Sonaria et al. developed footwear with 12 sensors (FSRs, accelerometers, gyroscopes) and applied PCA, Random Forest, and SVM to detect gait abnormalities. Another expert system combined FSRs with image processing to generate personalized treatment reports [13].

F. Sensor Density and Diagnostic Accuracy

Studies have experimented with varying sensor counts. A system with 30 FSRs revealed peak pressure in the heel region, while another with 15 sensors predicted flatfoot risk with over 80% accuracy [14]. Protective layering and anatomical sensor placement were used to enhance durability and precise position [15]. The most recent research utilized ResNet50 with CBAM attention modules to analyze plantar pressure images, achieving 96.6% classification accuracy [16].

G. Recent Innovations and Mobile Integration

The I-shoe project introduced a smart insole equipped with eight FSRs and a low-power microcontroller, paired with a mobile application that visualizes real-time pressure data and heatmaps. Machine learning algorithms were used to detect flatfoot and gait imbalance, with successful testing across multiple individuals. The system demonstrated potential for diabetic foot detection, rehabilitation, and athlete monitoring [17].

In summary, while prior research has demonstrated the feasibility of FSR-based systems for gait analysis and foot abnormality detection, challenges remain in achieving high-resolution data, ergonomic design, and clinical applicability. The proposed system in this study builds upon these foundations by integrating optimized sensor placement, standardized footwear, and real-time wireless transmission—aiming to bridge the gap between laboratory-grade accuracy and everyday usability.

In the following section, we present the design and implementation details of the proposed system, outlining its hardware architecture, sensor configuration, and data acquisition methodology.

III. MATERIALS AND METHODS

This section presents the overall architecture of the proposed system along with its hardware components, including the insole sensor module. In addition, the design and implementation of the graphical user interface (GUI) for data visualization, as well as the experimental protocol used for data collection, are described in detail.

A. System Architecture

The proposed system consists of a central workstation that wirelessly communicates with a set of wearable sensors. This workstation is responsible for executing processing algorithms and displaying real-time data. The overall system architecture is designed to enable seamless integration of hardware and software components for acquiring, transmitting, and analyzing plantar pressure data in real time. The analysis results are visually presented to the user via an intuitive graphical user interface. The system architecture is illustrated in Fig.2. The system architecture consists of three primary components: (1) a set of force-sensitive resistor (FSR) sensors embedded in the insole to capture plantar pressure data, (2) an ESP32-based microcontroller responsible for data acquisition and wireless transmission, and (3) a graphical user interface (GUI) developed in Delphi for real-time visualization and analysis. This modular design ensures seamless integration between hardware and software, enabling efficient monitoring and interpretation of gait patterns.

Fig.2. System Architecture Diagram

The data acquisition hardware includes a customized insole equipped with 10 force-sensitive resistor (FSR) sensors strategically placed at key points under the foot. These sensors measure pressure distribution across various regions of the foot during different phases of the gait cycle, enabling more precise analysis of walking patterns.

The ESP32 module has been selected as the central control unit due to its versatile features and high compatibility with wearable systems. In addition to supporting wireless communication via Wi-Fi and Bluetooth, the ESP32 offers adequate processing power, low energy consumption, and a compact size, making it ideal for portable applications. Its dual-core architecture, support for the TCP/IP protocol, and ability to maintain real-time communication with a host computer make it a suitable choice for collecting and transmitting multisensory data. Moreover, its ease of programming and availability of extensive development resources significantly accelerate system development and implementation.

Each shoe is equipped with a dedicated microcontroller, with the ESP32 module embedded in the right shoe functioning as the master unit and the module in the left shoe serving as the slave. Each insole is powered by a 700 mAh lithium-ion battery, providing approximately four hours of continuous operation per charge. The total weight of the embedded electronics is 85 grams per shoe. Preliminary tests demonstrated that an additional weight of up to 300 grams on the shoe system did not cause any observable interference with the natural gait pattern [18]. These findings confirm that the hardware configuration does not disrupt locomotion and is well-suited for wearable gait monitoring applications.

This design results in a lightweight, ergonomic, and wearable platform capable of effectively monitoring foot abnormalities in real time and analyzing the performance of the musculoskeletal system. Fig.3(a) shows an overview of the designed shoe, while Fig.3(b) illustrates the positioning of the electronic board and control module.

Fig. 3(a). Overview of the designed shoe: The custom-designed footwear integrates a sensorized insole equipped with 10 force-sensitive resistors (FSRs) strategically placed to capture plantar pressure data. The image illustrates the ergonomic layout of the sensors within the shoe, ensuring minimal interference with natural gait mechanics. The design prioritizes comfort, wearability, and accurate data acquisition during walking trials.

Fig. 3(b). Positioning of the electronic board and control module: The image shows the internal layout of the electronic components embedded within the shoe, including the ESP32 microcontroller, Li-ion battery (700 mAh), and supporting circuitry. The compact and lightweight arrangement ensures minimal interference with foot movement and maintains user comfort during walking trials. The modular placement facilitates easy maintenance and future upgrades.

Fig. 3 (a). Overview of the designed shoe

Fig. 3 (b). Positioning of the electronic board and control module

B. Insole Shoe

In this study, customized insoles were employed to enable precise analysis of gait patterns and plantar pressure distribution for detecting motor abnormalities and asymmetries in bilateral foot function. Each insole is equipped with 10 force-sensitive resistors (FSRs), strategically positioned in anatomically significant and distinguishable regions of the foot, as commonly adopted in clinical gait analysis protocols [19].

The choice of 10 FSR sensors per insole was based on a trade-off between spatial resolution, system cost, and ergonomic feasibility. Pilot tests with fewer sensors (e.g., 6 or 8) showed reduced sensitivity in detecting localized pressure variations, while configurations with more than 10 sensors increased system complexity and user discomfort. This configuration is consistent with sensor mapping strategies used in prior gait analysis research [19], ensuring coverage of key anatomical regions while maintaining wearability. Additionally, these locations were carefully selected to effectively capture pressure variations caused by body weight during the gait cycle and to be responsive to common foot abnormalities.

The selected sensors are thin, flexible, and lightweight, ensuring minimal interference with the user's walking mechanics and making them well-suited for wearable systems. The sensor layout was designed to capture pressure signals from the most functionally relevant areas of the foot that contribute to gait dynamics. This configuration enables detailed analysis of pressure distribution and facilitates the identification of abnormalities such as flat feet, pronation, supination, and foot instability. The sensor placement is illustrated in Fig. 4.

Gait analysis serves as an effective tool for the early detection of locomotor disorders, as these conditions, if not diagnosed and addressed in time, can lead to chronic pain, fatigue, and musculoskeletal injuries. Traditional assessment methods primarily rely on clinical observations and expert opinion, which may lack precision and objectivity. Therefore, developing systems capable of accurately measuring plantar pressure and algorithmically analyzing the data to provide objective classification of foot disorders is essential. This design supports continuous gait monitoring and enables early detection of foot-related motor disorders through detailed plantar pressure analysis.

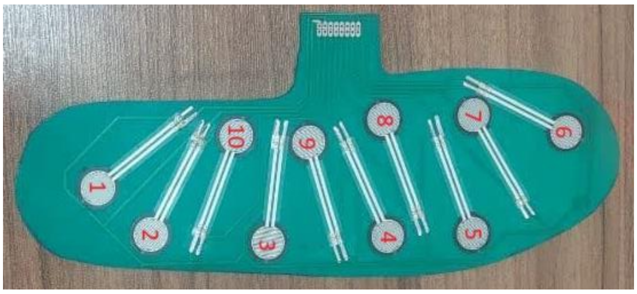

Fig.4. Sensor placement in insole shoe

C. Graphical User Interface

The software infrastructure of this system includes a graphical user interface (GUI) that provides functionalities such as real-time data visualization, pressure chart plotting, and data export. The GUI was developed using Delphi, a robust object-oriented programming language known for its rapid application development capabilities and native Windows support. This choice enabled efficient implementation of interactive features and ensured compatibility with the system's hardware architecture. Unlike commercial software packages often imposing rigid structures and licensing constraints, this GUI was fully developed in-house, allowing seamless customization based on user-specific requirements. Its modular codebase enables tailored adaptations for diverse clinical or research applications, offering a flexible alternative to proprietary platforms. Once collected, the incoming data undergoes processing for various analyses, including assessing pressure distribution. The results of these analyses are presented as graphs that illustrate pressure variations across different plantar regions throughout the gait cycle. The modular design of both hardware and software components enables future system scalability and integration with machine learning algorithms. This architecture not only supports clinical evaluations and rehabilitation monitoring but also offers a cost-effective platform for continuous at-home monitoring of plantar dysfunctions.

Fig. 5. View of the developed graphical user interface (GUI).

The GUI displays real-time pressure data from all 10 sensors embedded in each insole, with separate plots for the left and right foot. Each chart illustrates pressure variations across the gait cycle, enabling visual comparison between healthy and pathological gait patterns. In addition to graphical plots, the GUI supports numerical summaries of key gait parameters, Fourier analysis, and additional features such as data storage and printing, thereby enhancing clinical interpretability. The central schematic of foot anatomy aids in sensor localization, while the modular layout supports intuitive navigation and data export. This interface facilitates clinical interpretation and remote monitoring of plantar pressure dynamics in real-world settings.

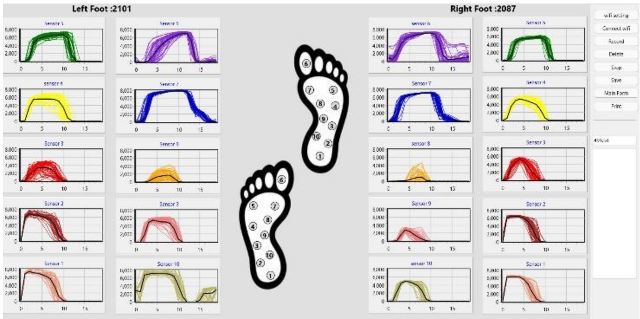

Fig.5. View of GUI

D. Experimental Protocol

To evaluate the performance of the developed system, data were collected from four male participants: one with a normal gait pattern and three with foot abnormalities, including external rotation, internal rotation, and supination. Participants ranged in age from 22 to 45 years, with BMIs between 22 and 25. Aside from the observed gait abnormalities, none of the participants reported any history of neurological or musculoskeletal disorders.

The participants had shoe sizes ranging from 39 to 43 and body weights between 70 and 80 kilograms.

All participants wore the custom-designed shoes, and the sensors were positioned according to the key pressure regions of the plantar surface. All walking trials were conducted in a controlled indoor environment with uniform lighting and temperature. Participants walked on a treadmill while wearing identical shoes. The walking speed was the same for all individuals, and no external distractions were present during data collection. No external distractions were present during data collection.

Before data recording began, participants were asked to walk on the treadmill to establish a natural and steady gait pattern. Once a natural and unconstrained walking rhythm was achieved, plantar pressure data were recorded for one minute under these controlled conditions. The primary objective of this experiment was to analyze the gait pattern across different conditions with high precision. For this purpose, the recorded signals were first segmented, and individual gait cycles were identified. In this study, a gait cycle was defined as the time interval between heel-off and subsequent heel contact. This method allows for analyzing various gait cycle components, such as the heel-strike phase, without the need for precise event detection, while preserving temporal coherence within each cycle. In addition to pressure signals, derived gait parameters such as contact duration and step length were extracted to support comprehensive gait analysis.

Next, the DTW algorithm was employed to perform temporal alignment of the gait cycles. DTW was selected over traditional Euclidean distance methods due to its robustness in handling temporal variations and proven effectiveness in gait analysis applications. DTW, a widely used technique for time-series analysis, enables the comparison of sequences with varying lengths or speeds by establishing a nonlinear alignment between them.

After alignment, point-wise averaging was applied to the time-normalized gait cycles to generate a representative signal for each individual or condition. This process reduced intra-subject variability and noise, enhancing the clarity of the final signal. Only gait cycles with successful alignment and comparable normalized durations were included in this step. The outcome was a smooth and stable signal that accurately reflected the average gait pattern while minimizing the influence of outlier steps or transient noise [1], [11].

This methodological framework ensures accurate acquisition and analysis of plantar pressure data, laying the foundation for reliable gait assessment and early detection of foot abnormalities. While the sample size was limited to four participants, the protocol was designed to ensure consistency and reliability. Future studies with larger and more diverse populations are planned to validate and generalize the findings.

IV. EXPERIMENTAL RESULTS

The data collected from the designed shoe demonstrates the system's high performance in accurately reconstructing plantar pressure patterns under various conditions. The graphs obtained from the sensor data clearly confirm the system's ability to distinguish pressure variations across different regions of the foot, which is consistent with the findings of previous studies [20]. Figures 6 to 9 illustrate the average pressure patterns recorded by each sensor for four participants: a healthy individual, a subject with an external rotation deformity, a subject with an internal rotation deformity, and a subject with supination. As observed, the average gait pattern for all participants corresponds to the fundamental gait cycle during the stance phase, ensuring reliable segmentation and extraction of gait cycles for subsequent analysis. For a more precise comparison, the right and left foot patterns are shown in blue and red, respectively.

Figure 6 illustrates the gait pattern of the healthy subject. Across all 10 sensors, it is evident that the pressure distribution and step length in both feet are nearly identical, and the red and blue waveform signals exhibit good coordination. The slight difference in signal amplitude may result from greater pressure applied to one foot during stepping, which is a natural characteristic of human gait.

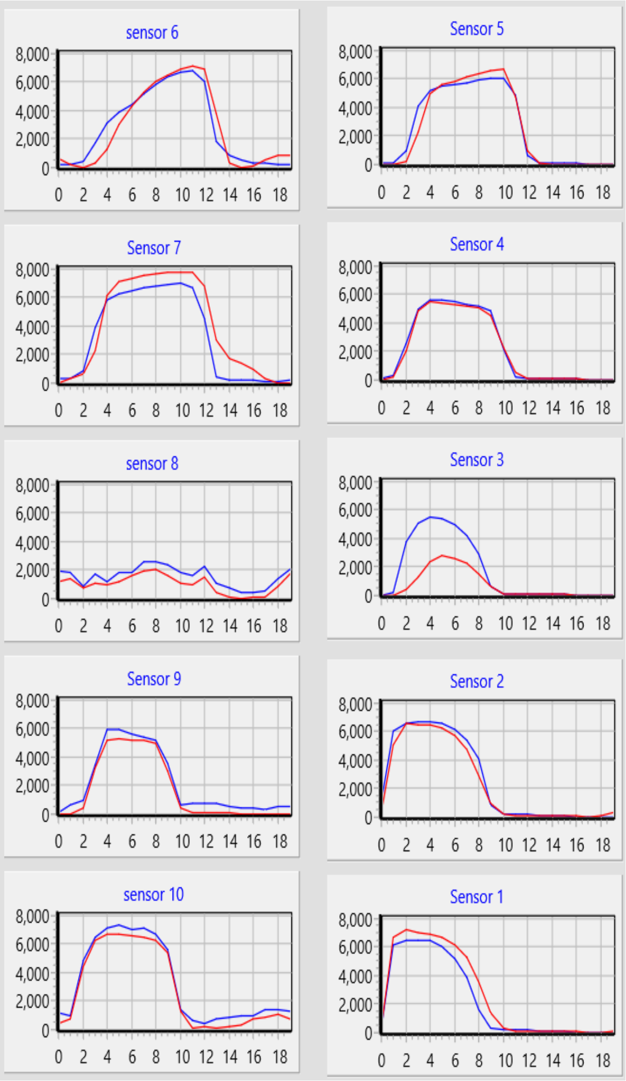

Fig. 6. Gait pattern of a healthy subject

Fig. 7 illustrates the gait pattern of a subject with an external rotation deformity. This condition, characterized by the outward deviation of the foot's motion axis (commonly referred to as out-toeing), has resulted in a shorter step length for the right foot compared to the left. This observation indicates that the subject spent a longer duration in the weight-bearing phase on the left foot. Nevertheless, a relative symmetry between the two feet is still maintained, suggesting that the gait mechanics are not severely disrupted despite the deformity.

Fig. 8 corresponds to the subject with an internal rotation deformity, a condition in which the toes point inward during walking (in-toeing). In this case, there is no significant difference in step length between the two feet; however, sensor number 7, located in the forefoot region, has recorded higher pressure in one foot. This observation suggests increased force application in that area due to the internal rotation of the foot, resulting in concentrated pressure on the anteromedial (front-inner) region of the plantar surface.

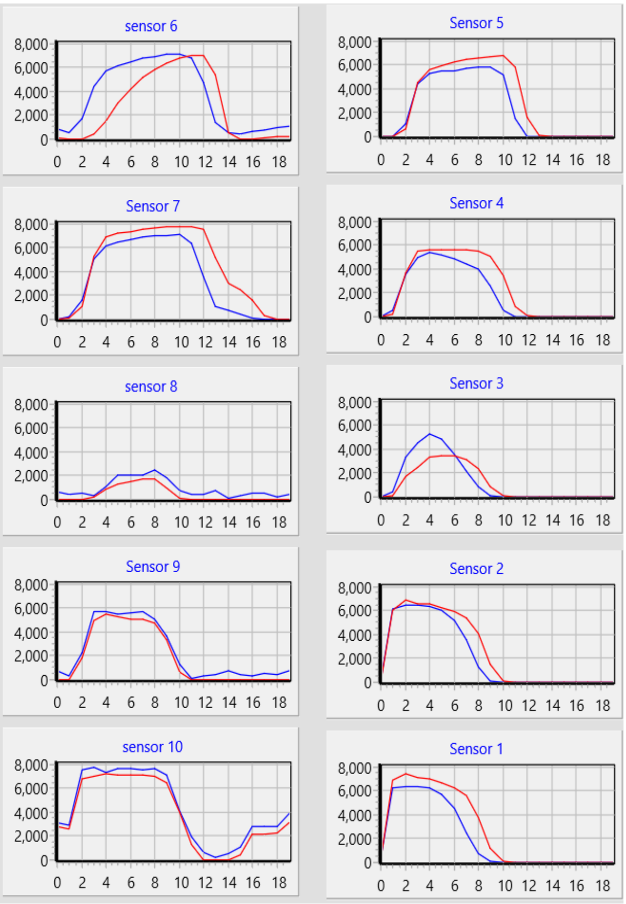

Fig. 7. Gait pattern of the external rotation subject

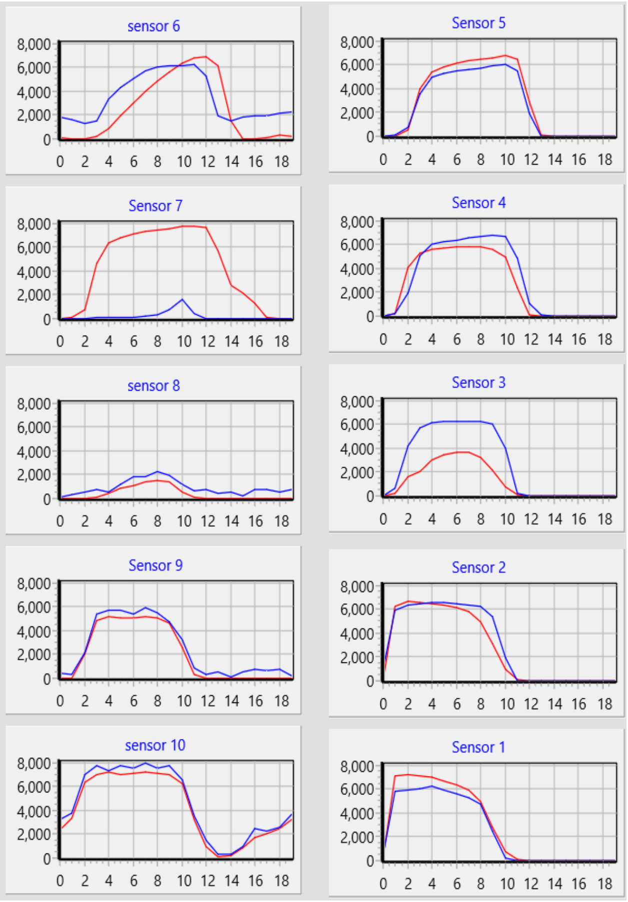

Fig. 8. Gait pattern of the internal rotation subject

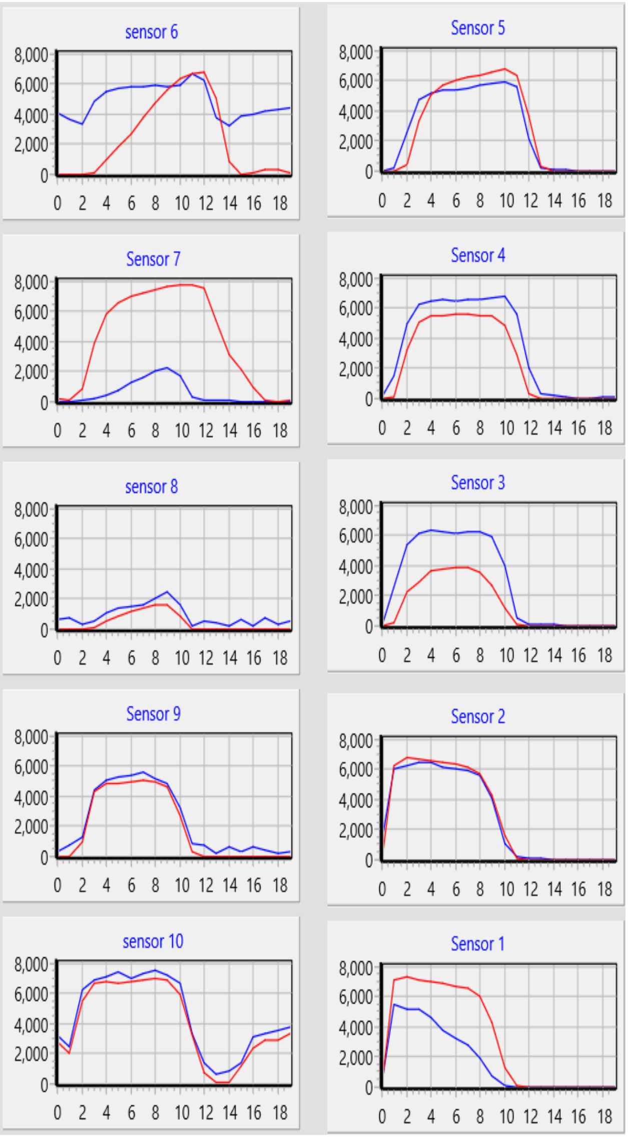

Fig. 9. Gait pattern of a supination subject

Fig. 9 presents the gait pattern of a subject with a supination deformity. This condition, marked by the outward rotation of the ankle and increased pressure on the outer edge of the foot, has led to noticeable alterations in the patterns recorded by specific sensors. Notably, sensors 6 and 7, positioned in the anterior and lateral regions of the foot, exhibit significant deviations. These findings are consistent with the biomechanical characteristics of supination, wherein body weight is asymmetrically distributed toward the lateral side of the foot. Such load distribution may contribute to long-term functional issues if not addressed.

The peak pressure values were calculated for different plantar regions, and the results for the four participants (healthy, external rotation deformity, internal rotation deformity, and supination) are presented in Table 1. This table allows for a detailed comparison of pressure across each foot region and facilitates the analysis of gait-related abnormalities. The headings S1 to S10 correspond to sensors numbered 1 through 10, respectively. The sensor locations can be seen in Fig. 4.

As shown in Table I, the peak pressure values recorded by sensors S1 through S10 reveal distinct gait characteristics across participants, enabling detailed analysis of plantar load distribution and associated abnormalities.

TABLE I
Peak Pressure Values (N/cm^2) Across Plantar Regions for Four Participants

Foot Region	Healthy	External Rotation	Internal Rotation	Supination
S1	7.5	7.8	7.2	8.0
S2	7.2	7.9	7.1	8.3
S3	6.0	6.5	5.8	8.5
S4	5.8	6.7	6.0	8.2
S5	5.5	5.0	5.2	6.0
S6	5.4	5.1	5.3	6.1
S7	11.2	10.0	11.0	10.5
S8	10.8	10.2	11.3	10.7
S9	2.0	2.2	1.8	2.0
S10	1.8	2.3	2.0	2.2

- **Healthy Participant**: Pressure values are relatively balanced across all regions. Sensors S7 and S8, located in the forefoot area, show the highest readings, which align with the natural weight transfer during the propulsion phase of gait.
- **External Rotation Deformity**: Slightly elevated pressure is observed in the lateral regions (S1–S4), indicating a shift in weight toward the outer edge of the foot due to the outward deviation of the motion axis. Reduced pressure in the midfoot (S5 and S6) may reflect compromised central stability.
- **Internal Rotation Deformity**: Sensor S7 records notably higher pressure in one foot, suggesting increased force concentration in the anteromedial region of the plantar surface. This pattern is consistent with inward toe positioning and altered load distribution.
- **Supination**: This participant exhibits elevated pressure values in the lateral and anterior regions (S3–S4 and S6–S8), consistent with the sensor-based observations illustrated in Figure 9. This asymmetric load distribution, typical of supination, may contribute to long-term structural or functional complications if left unaddressed.

The numerical differences across participants reveal that each deformity induces distinct and quantifiable shifts in plantar pressure distribution. These variations are not only evident in peak values but also in spatial pressure patterns. The data serve as quantitative indicators for early detection of gait abnormalities and can be instrumental in monitoring rehabilitation progress or tailoring clinical interventions.

Overall, the experimental data collected using the proposed system validate its strong capability in accurately detecting and differentiating gait features, reinforcing its clinical applicability in gait assessment and rehabilitation monitoring.

V. DISCUSSION AND FUTURE WORKS

In this study, a wearable foot pressure monitoring system based on a wireless architecture was successfully designed and implemented. The system integrates modular hardware components and an advanced graphical user interface for real-time data visualization. Experimental results demonstrated that the proposed system possesses high accuracy in capturing pressure variations across different regions of the foot and can provide meaningful insights into gait patterns under both normal and pathological conditions. This performance is particularly notable in distinguishing subtle gait deviations, as evidenced by the system's ability to detect asymmetries in supination and internal rotation cases.

The analysis of pressure sensor data enabled the identification of gait components and the visualization of plantar pressure distribution throughout different phases of walking. This capability not only facilitates the detection of abnormalities such as flatfoot, internal and external rotation, or supination but also serves as an effective tool for tracking patients' rehabilitation progress during treatment. The developed platform also holds promise for clinical and home-based applications, particularly for continuous monitoring of motor performance in patients and the elderly. Although the system shows promise for home-based use, its performance under uncontrolled environmental conditions remains to be validated.

Despite the promising results, the system still faces certain limitations. One major challenge is the latency in data processing, mainly due to the high volume of sensor input and limited computational resources on the client side. This latency occasionally affects real-time responsiveness, particularly during prolonged walking sessions or high-frequency sampling. Optimizing data structures and improving the processing algorithms could significantly mitigate these delays.

Future research will focus on leveraging this platform for the early detection of foot-related functional disorders and assessing movement impairments associated with ankle joint conditions. Future work will explore convolutional neural networks (CNNs) for automated gait classification and test the system in post-stroke patients to assess rehabilitation outcomes. Integrating machine learning algorithms for more precise classification of gait patterns, expanding the participant population to enhance generalizability, and developing lighter and more portable system versions will further broaden this platform's clinical and practical applications.

ACKNOWLEDGMENTS

The Authors would like to thank all patients who freely participated in this study.

FUNDING STATEMENT

None of the authors received any financial support or funding from public, commercial, or non-profit organizations for the research, authorship, or publication of this article.

CONFLICTS OF INTEREST

The authors declare that they have no known competing financial interests or personal relationships that could have appeared to influence the work reported in this paper.

AUTHORS' CONTRIBUTIONS

Data collection and experimentation: (Maryam Farivar, Hadi Soltanizadeh, Mohammad Zahrayee)

Data analysis and interpretation: (Maryam Farivar, Hadi Soltanizadeh, Mohammad Zahrayee)

Manuscript writing and editing: (Maryam Farivar, Hadi Soltanizadeh

Supervision and project administration: (Maryam Farivar, Hadi Soltanizadeh

STATEMENT ON THE USE OF GENERAL AI

We used AI as a tool for language editing.

References

[1] U. Pant, S. Baral, A. Gupta, and P. L. Shrestha, "Design of Force Sensitive Resistor (FSR) embedded insole for phase detection during human gait and its classification."

[2] J. A. Ramirez-Bautista, J. A. Huerta-Ruelas, S. L. Chaparro-Cárdenas, and A. Hernández-Zavala, "A Review in Detection and Monitoring Gait Disorders Using In-Shoe Plantar Measurement Systems," Aug. 30, 2017, *Institute of Electrical and Electronics Engineers*. doi: 10.1109/RBME.2017.2747402.

[3] A. M. Shayan, A. Khazaei, A. Hamed, A. Amralizadeh, and M. T. Masouleh, "ShrewdShoe, a smart pressure sensitive wearable platform," in *Proceedings of the 6th RSI International Conference on Robotics and Mechatronics, IcRoM 2018*, Institute of Electrical and Electronics Engineers Inc., Jul. 2018, pp. 458–463. doi: 10.1109/ICRoM.2018.8657559.

[4] A. M. Shayan, A. Khazaei, A. Hamed, A. Amralizadeh, and M. T. Masouleh, "ShrewdShoe, a smart pressure sensitive wearable platform," in *Proceedings of the 6th RSI International Conference on Robotics and Mechatronics, IcRoM 2018*, Institute of Electrical and Electronics Engineers Inc., Jul. 2018, pp. 458–463. doi: 10.1109/ICRoM.2018.8657559.

[5] J. Pacheco-Chérrez, J. C. Tudon-Martinez, and J. J. de Lozoya-Santos, "Recent Advances in Pediatric Wearable Lower-Limb Exoskeletons for Gait Rehabilitation: A Systematic Review," 2025, *Institute of Electrical and Electronics Engineers Inc.* doi: 10.1109/ACCESS.2025.3552757.

[6] M. Muñoz-Organero, C. Littlewood, J. Parker, L. Powell, C. Grindell, and S. Mawson, "Identification of walking strategies of people with osteoarthritis of the knee using insole pressure sensors," *IEEE Sens J*, vol. 17, no. 12, pp. 3909–3920, Jun. 2017, doi: 10.1109/JSEN.2017.2696303.

[7] A. H. Abdul Razak, A. Zayegh, R. K. Begg, and Y. Wahab, "Foot plantar pressure measurement system: A review," Jul. 2012. doi: 10.3390/s120709884.

[8] A. Jor, S. Das, A. S. Bappy, and A. Rahman, "Foot Plantar Pressure Measurement Using Low Cost Force Sensitive Resistor (FSR): Feasibility Study," *Journal of Scientific Research*, vol. 11, no. 3, pp. 311–319, Sep. 2019, doi: 10.3329/jsr.v11i3.40581.

[9] W. C. Hsu, T. Sugiarto, J. W. Chen, and Y. J. Lin, "The design and application of simplified insole-based prototypes with plantar pressure measurement for fast screening of flat-foot," *Sensors (Switzerland)*, vol. 18, no. 11, 2018, doi: 10.3390/s18113617.

[10] N. K. Madzhi, A. Asraf, B. Muhamad, @ Mhd, and E. Abdullah, "Preliminary Investigation on the Effect of Speed Variation to Pressure Distribution for Flat, Medium and High Foot Arch." [Online]. Available: https://www.tarjomano.com

[11] D. Price, "Midfoot pressure analysis in individuals with flat feet while climbing stairs using a pressure sensing system," *American Journal of Student Research*, 2025.

[12] M. J. Domínguez-Morales, F. Luna-Perejón, L. Miró-Amarante, M. Hernández-Velázquez, and J. L. Sevillano-Ramos, "Smart footwear insole for recognition of foot pronation and supination using neural networks," *Applied Sciences (Switzerland)*, vol. 9, no. 19, Oct. 2019, doi: 10.3390/app9193970.

[13] P. ; P. V. B. ; R. M. ; M. B. ; K. R. S. ; R. J. R. F. Vigneshwaran, "Development of an expert system for advanced podiatric treatments and ergonomics," 2025, pp. 924–930.

[14] Z. ; L. Y. ; C. X. ; W. H. ; L. J. Zhang, "Insole systems for disease diagnosis and rehabilitation: A review," 2023.

[15] Y. ; W. X. ; L. H. ; C. Y. ; Z. L. Zhao, "A deep learning method for foot-type classification using plantar pressure images," vol. 11, 2023.

[16] S. ; W. Y. ; L. Z. ; X. L. Wu, "Toward automated foot type diagnosis: A deep learning approach with attention mechanism and Grad-CAM interpretability," Institute of Electrical and Electronics Engineers (IEEE), 2024.

[17] A. S. ; M. R. K. ; D. S. V. Patel, "i-Shoe: A Smart Insole System for Gait Imbalance Detection Using FSR Sensors and Mobile Integration," Springer, 2024, pp. 245–258.

[18] J. A. Ramirez-Bautista, J. A. Huerta-Ruelas, S. L. Chaparro-Cárdenas, and A. Hernández-Zavala, "A Review in Detection and Monitoring Gait Disorders Using In-Shoe Plantar Measurement Systems," Aug. 30, 2017, *Institute of Electrical and Electronics Engineers*. doi: 10.1109/RBME.2017.2747402.

[19] J. ; B. J. M. Perry, *Gait Analysis: Normal and Pathological Function*, 2nd ed. SLACK Incorporated, 2010.

[20] M. Adnan *et al.*, "IDC pressure sensors enabled smart footwear system for in vitro detection and monitoring of diabetic foot ulcer," *Sens Actuators A Phys*, vol. 388, Jul. 2025, doi: 10.1016/j.sna.2025.116489.

Semnan University

Journal of Modeling & Simulation in Electrical & Electronics Engineering (MSEEE)
Journal homepage: **https://mseee.semnan.ac.ir/**

ISSN: 2821-0786

A Highly Efficient Nanoscale Demultiplexer Architecture based on Quantum-Dot Cellular Automata

Hamidreza Ghaemi Peykani[1], Morteza Dorrigiv[2] and Mohammad Danaie[3]*

***Abstract*-This paper presents the design of a demultiplexer (DMUX) structure using Quantum-dot Cellular Automata (QCA) technology. A demultiplexer is a fundamental circuit that receives information from a single input line and routes it to one of several output lines, with the selected output determined by the control inputs. Widely employed in communication systems, demultiplexers enable the transformation of serial data streams into parallel outputs. In this work, an optimized architecture for a 1:2 QCA demultiplexer is proposed, characterized by simplicity, efficiency, and reliability, with the added capability of implementing a wide range of logical functions. Furthermore, a novel 1:4 QCA demultiplexer is developed based on the proposed structure, eliminating the need for coplanar cells or crossover wires. Simulation results confirm the superior performance of the proposed architectures in terms of reduced cell count, area, and latency. Specifically, the 1:2 design requires only 17 QCA cells, occupies 0.01 µm², and exhibits a delay of 0.25 clock cycles, while the 1:4 demultiplexer requires 74 QCA cells, occupies 0.07 µm², and achieves a delay of 3 clock cycles.**

***Index Terms*- Demultiplexer, Majority voter, Quantum-dot Cellular Automata, Crossover, Coplanar**

I. INTRODUCTION

Quantum-dot cellular automata (QCA) is an emerging nanotechnology that offers a promising alternative to conventional CMOS technology for implementing digital circuits at the nanoscale. First introduced in the early 1990s, QCA exploits the position of electrons within quantum-dot cells to represent binary information, thereby eliminating the need for current flow as in traditional transistor-based logic. Instead of relying on transistors, QCA uses the Coulombic interactions between neighboring cells to perform computation and signal transmission, enabling ultra-low power consumption and extremely high device density. With feature sizes potentially scaling down to a few nanometers, QCA has gained significant attention in recent decades as one of the most viable post-CMOS computing paradigms.

Due to its inherent advantages, QCA has been extensively explored for a wide range of applications, including logic gates, arithmetic circuits, memory elements, and complex architectures such as multiplexers, demultiplexers, and processors. Its potential for ultra-fast switching, reduced interconnect delay, and energy-efficient operation makes it highly relevant for the design of nanoscale computing systems where conventional CMOS faces scaling and power dissipation challenges. Moreover, the ability of QCA to implement highly compact, regular, and fault-tolerant architectures positions it as a key enabler for next-generation nano-electronic systems. In this context, designing efficient QCA-based demultiplexers is particularly important, as they are essential building blocks for signal routing, data distribution, and communication in nanoscale circuits.

Due to its advantages, such as rapid speed, small size, and low energy consumption, QCA technology stands out as one of the selected methods for addressing the challenges faced by nanometer-scale CMOS devices. Some of these obstacles encompass high power density levels, elevated leakage currents, and substantial lithography costs. In QCA circuits, which are being explored as potential substitutes for CMOS technology, information processing revolves around cell polarization, which is subsequently communicated to neighboring cells through Coulomb contact. The high device density [1], ultra-low power efficiency [2], and rapid computing performance [3-6] exhibited by these nanostructures have been extensively demonstrated.

Received; 2025-04-23 Revised; 2025-09-26 Accepted; 2025-10-14

[1] Faculty of Electrical and Computer Engineering Faculty, Semnan University, Semnan, Iran.
[2] Faculty of Electrical and Computer Engineering Faculty, Semnan University, Semnan, Iran.
[3] Faculty of Electrical and Computer Engineering Faculty, Semnan University, Semnan, Iran.
*Corresponding author: danaie@semnan.ac.ir

Cite this article as:
Ghaemi Peykani, H., Dorrigiv M.& Danaie M. (2025). A Highly Efficient Nanoscale Demultiplexer Architecture based on Quantum-Dot Cellular Automata. *Journal of Modeling & Simulation in Electrical & Electronics Engineering (MSEEE)*. Semnan University Press . *5 (4),* 9-15.
DOI: https://doi.org/10.22075/mseee.2025.37506.1206

Consequently, QCA-based logic circuits have garnered significant attention in recent years.

Numerous endeavors have been undertaken to utilize these nanostructures for implementing crucial components of Combinational Circuits, including XOR, X-NOR gates [7–11], multiplexers, demultiplexers [12–18], Adders, Subtractors, RAM cells, and ALU units.

Among the various circuit architectures explored using QCA, demultiplexers play a crucial role as fundamental data-routing elements in communication and computing systems. They are widely used in memory addressing, signal distribution, and interconnection networks, where efficient and reliable data transfer is essential. As the demand for nanoscale integration grows, QCA-based demultiplexers have been the subject of extensive research aimed at reducing circuit area, minimizing latency, and improving overall stability. Several designs have been proposed in the literature with varying trade-offs between complexity, performance, and robustness. Demultiplexer is one of the important parts of the nano-router building blocks and to imitate the calculator circuit, a demultiplexer combines adder, subtractor, multiplexer, and divider circuits into a single circuit. The data is taken via input lines, and sent to the 2N output at a time, based on N selector signals. Output equation of 1:2 demultiplexer is Out0 = $\bar{S}$.IN, Out1 = S.IN, where S = 0 means the input data transferred to output 0 and if S = 1 means the input data is sent to the output 1. In QCA technology, several designs and architectures for demultiplexers have been published.

A systematic review of the existing demultiplexer architectures is necessary to highlight their strengths and limitations, and to position the proposed nanoscale demultiplexer within the context of ongoing advancements in QCA-based circuit design. In [19], the authors propose a fault-tolerant 1:2 QCA demultiplexer using an inverter and a two-input AND gate. The design leverages cell redundancy to enhance robustness against common defects such as missing, dislocated, extra, and misaligned cells. However, the approach remains limited in scalability, as it only addresses a basic 1:2 demultiplexer structure rather than larger and more complex architectures. The demultiplexing method presented in [20] focuess on energy dissipation and cost metrics, using QDE and QCAPro simulation tools. Results show that the proposed designs achieve very low energy dissipation and favorable cost functions, highlighting their efficiency for nanoscale systems. However, the work is limited to small-scale blocks and relies on simulations at low operating temperatures (2 K), which may restrict practical applicability.

Khan an Arya have proposed QCA layouts for a 1:2 multiplexer and 1:2 demultiplexer, showing low energy dissipation and evaluated through both QDE and QCAPro with multiple cost functions [21, 22]. Meanwhile, Sharma and Kaushil have proposed a novel area-efficient 1:2 QCA demultiplexer using only 11 cells, achieving significant reductions in layout area, cost, and power dissipation compared to prior designs [23]. While their results demonstrate strong efficiency and energy savings, the study is limited to a basic 1:2 architecture, leaving scalability to larger demultiplexers unexplored. Similar structures have been proposed in [24-30].

This study provides a 1:2 demultiplexer with an optimum structure and suggested architecture is used to implement the 1:4 demultiplexer. Concerning size, speed, and intricacy, the suggested architecture provides several advantages over the topologies reported in the literature. The novelty of this work lies in proposing an optimum QCA-based demultiplexer architecture that is both simple and highly efficient, requiring fewer cells, smaller area, and lower latency than existing designs. Unlike many prior approaches, the 1:4 demultiplexer is implemented without coplanar cells or crossover wires, significantly improving reliability and scalability. Additionally, the architecture is versatile, as it can be extended to generate a range of logical functions, making it a flexible building block for nanoscale communication systems.

II. QCA BASIC ELEMENTS

The basic structure of a QCA cell is illustrated in Figure 1 [31, 32]. Each cell consists of four quantum dots arranged in a square configuration and two mobile electrons, which can tunnel between the quantum dots. Due to electrostatic repulsion, the electrons occupy antipodal sites within the cell. Unlike conventional electronics, where current flow represents information transfer, QCA operates through Coulombic interactions, whereby the state of one cell influences its neighboring cells, enabling data propagation. The system has two energetically stable configurations, as shown in Figure 1, corresponding to distinct electron arrangements. The polarization of a QCA cell, defined by Equation (1), determines whether the cell represents a binary “0” (−1 polarization) or binary “1” (+1 polarization) based on the positions of the electron pair [33, 34].

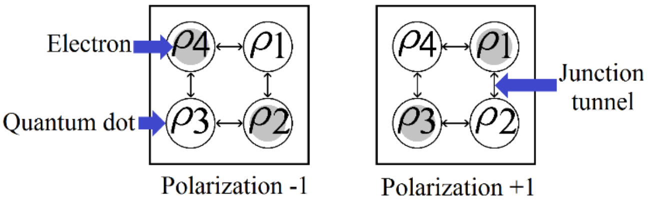

(a) (b)

Fig. 1. Structure of a basic QCA cell and cells polarization in QCA technology (a) Polarization -1 refers to 0 (b) Polarization +1 refers to 1.

TABLE I
Three-input Majority Voter Truth Table

IN			OUT
Z	Y	X	**O**
0	0	0	**0**
0	0	1	**0**
0	1	0	**0**
0	1	1	**1**
1	0	0	**0**
1	0	1	**1**
1	1	0	**1**
1	1	1	**1**

The fundamental building blocks of QCA technology are the majority voter (MV) gate, the inverter gate, and the binary wire. The MV is a three-input device realized with a five-cell configuration, as illustrated in Figure 2(a). Inputs are applied through cells A, B, and C, while the central cell acts as the device cell, adopting the polarization of the majority of the inputs. The output cell (O), positioned on the right, replicates the polarization of the device cell. The complete truth table of the MV gate is presented in Table I, while Figures 2(b) and 2(c) demonstrate how the MV can be configured to implement 2-input AND and OR logic functions, thereby covering all possible input–output combinations of the majority voter.

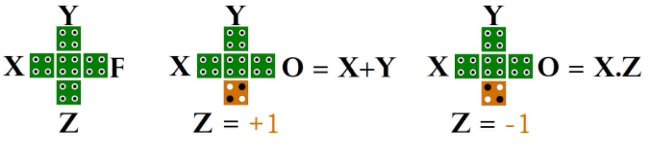

(a) (b) (c)

Fig. 2. Structure of (a) Majority voter (b) Majority voter as an AND logic gate (c) Majority voter as an OR logic gate.

The QCA wire is shown in two different configurations in Figure 3. Although in QCA technology wires contribute to information transfer from one part of the circuit to another, they can conduct certain computations on the data to be sent. The other basic logic gate in QCA is the inverter gate. It takes the logic from the input and creates the logic's complement on the output. The output equation of the inverter gate is $A = \bar{A}.Clk$. Inverter gates can be layout in a variety of methods, but the structures depicted in Figure 4 are regarded to be as reliable as inverter gates.

(a) (b)

Fig. 3. Schematic of a) Normal wire built with normal cells, (b) Rotated wire built of rotate cells.

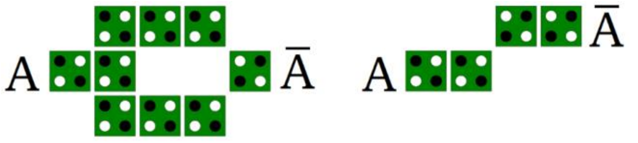

(a) (b)

Fig. 4. Structure of a (a) QCA inverter gate with two paths, (b) QCA operational inverter gate.

III. CLOCKING IN QCA

In conventional CMOS technology, the clock is employed to control the timing of sequential circuits. In QCA, however, the clock not only governs switching but also provides the necessary output gain [35, 36]. Clock signals regulate electron tunneling by modulating the potential barriers between quantum dots, and they are generated using electric fields supplied through CMOS or carbon nanotube (CNT) wires embedded beneath the QCA surface [37]. The maximum number of cells that can be assigned to a single clocking zone is determined by Eq. (1), where E_k denotes the kink energy, k_B is the Boltzmann constant, and TTT is the operating temperature in Kelvin. [34].

$$Number\ of\ Cells \leq e^{(Ek/KB.T)} \tag{1}$$

As indicated in Figure 5, the clocking technique is made up of four clock pulses with the same frequency that one clock signal is regarded as the reference (clock = 0), while the others are delayed one-quarter of the period. Each clock pulse has four phases: switch, hold, release, and relax. With a phase shift of 90 degrees. Clocking is accomplished by electrostatically switching the cell from its null state, in which it contains no binary data. The condition of a cell is dictated by its surroundings. The whole QCA circuit is separated into clock zones, with each clock signal assigned to its zone. The cells of each clock zone transit through all four phases of that clock zone during the communication process. After these four processes, the information is sent.

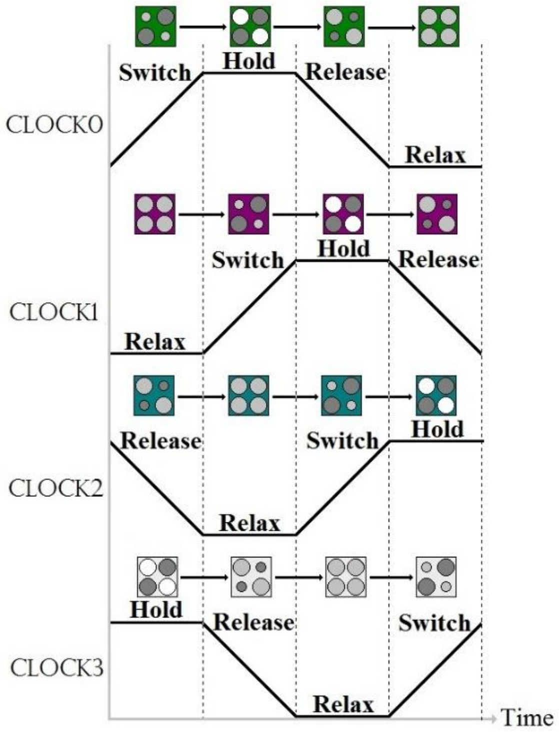

Fig. 5. Clocking schemes and a variety type of cells in QCA technology that use for information transfer.

IV. PREVIOUS WORKS

Different architectures and implementations for QCA-dependent demultiplexers have been discussed in this section. Demultiplexer circuit takes information from its input and sends them to the output lines, where at each time one of the 2N outputs depending on N selector signals receives input data. In [35] proposed a new modular approach for designing a 1:2N demultiplexer. This method simplifies the process of designing high-order demultiplexers. As a building block, 1:2 QCA demultiplexer architectures are supplied, followed by 1:4 and 1:8 demultiplexers. Any 1:2N demultiplexer that has been schematized using the recommended approach may easily be upgraded to a bigger 1:2N demultiplexer. A lesser cell count and a smaller area are used in this suggested technique.

A QCA 1:4 demultiplexer is a necessary component of a QCA nano-router device suggested in [32]. A large number of gates are used in the implementation of this circuit. To deal with the problem of line crossing, a design with several layers was used, with no interference from cells. This design allows the nano-router to communicate at a faster rate. Ahmad [37] has presented a unique notion of a 1:2n demultiplexer based on QCA technology. The present execution is primarily focused on improving efficiency and reducing circuit complexity. Two inverters and four three-input AND gates were required to create an optimum 1:4 demultiplexer using this layout. The suggested designs have evolved in terms of space utilization and complexity.

Many other topologies have been presented in the literature [38-44]. For instance, to make a QCA-based Nano-calculator, Chakrabarty et al. built a 1:4 demultiplexer [41]. To imitate the calculator circuit, this demultiplexer combines adder, subtractor, multiplexer, and divider circuits into a single circuit. Three clock zones are employed to complete a full cycle in the described demultiplexer, which is dependent on a multilayer crossover method. The suggested configuration has a larger overall area and a greater QCA cell number. 1:2 demultiplexers have two majority voters, and one to four demultiplexers have eight majority voters in this configuration. The multilayer crossover was avoided in the suggested designs.

V. THE PROPOSED TOPOLOGIES

Table II and Figure 6 show the truth table and configuration of the recommended one-to-two demultiplexer respectively. The suggested structure utilizes two majority gates with AND logic implementations to optimize device density, layout area, number of QCA cells, and computation velocity in a single layer. There is no need to rotate or crossover cells and the suggested arrangement is single-layer and consists of 17 QCA cells, with a total size of 0.01 µm2. Furthermore, it utilizes one phase of the clock for producing valid output. The layout of the proposed structure demonstrates in Figure 7.

TABLE II
Truth Table for QCA-DMUX of 1:2.

S	IN	Out1	Out0
0	0	0	0
0	1	0	1
1	0	0	0
1	1	1	0

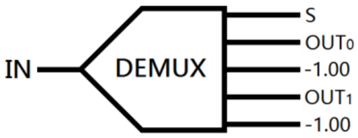

Fig. 6. Schematic circuit of the proposed 1:2 QCA-DMUX.

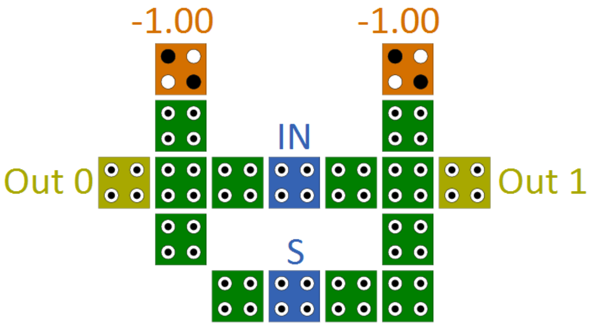

Fig. 7. The layout circuit of the proposed 1:2 QCA-DMUX.

Four outputs (Out0, Out1, Out2, and Out3), 1 input (IN), and 2 selector lines (S0S1) make up the 1:4 DEMUX. The suggested structure employs three 1:2 demultiplexer blocks, as shown above. Table III shows the truth table of a 1:4 demultiplexer, when S0S1=00, 01, 10, and 11, the Out0, Out1, Out2, and Out3 get the input data respectively. The 1:4 demultiplexer architecture is implemented in a single layer without the application of crossover or rotate cells, and the suggested structure has 74 QCA cells and takes up 0.07 µm2 of space. Furthermore, it makes utilization of three phases of the clock to provide legitimate output. Figure 8 and Figure 9 shows the schematic and the configuration of the suggested demultiplexer architecture respectively.

TABLE III
Truth Table for QCA-DMUX of 1:4.

S0	S1	IN	Out3	Out2	Out1	Out0
0	0	0	0	0	0	0
0	0	1	0	0	0	1
0	1	0	0	0	0	0
0	1	1	0	0	1	0
1	0	0	0	0	0	0
1	0	1	0	1	0	0
1	1	0	0	0	0	0
1	1	1	1	0	0	0

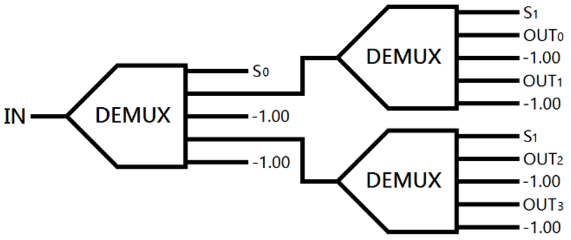

Fig. 8. Schematic circuit of proposed 1:4 QCA-DMUX.

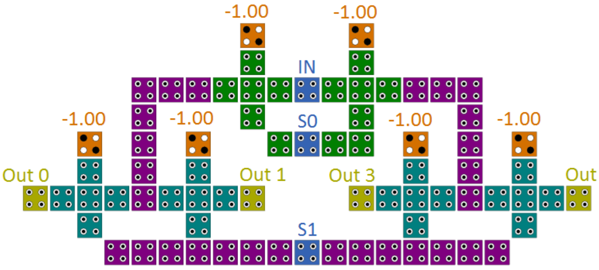

Fig. 9. Layout structure of proposed 1:4 QCA-DMUX.

VI. RESULTS AND COMPARISONS

The input and output waveform simulations of the proposed 1:2 and 1:4 demultiplexers illustrate in Figure 10 and Figure 11 respectively. Table IV and Table V provide a comparison of performance between the proposed design and earlier designs. QCA Designer tool and Bistable Approximation engine by the default settings were used to create all of the proposed circuits and results. In QCA circuits, information propagates as the polarization of one cell influences its neighboring cells. At certain points, wire crossings are required to facilitate signal routing. The primary crossover techniques in QCA include planar, multi-layer, and logical crossovers. Planar crossovers typically employ a combination of regular and rotated cells, multi-layer crossovers rely on multiple physical layers, and logical crossovers achieve wire intersection by utilizing non-consecutive clock phases. To evaluate the designing efficiency, the cost function known as the generalized cost function for semiconductor QCA is used, where the number of majority gates (M), inverter gates (I), latency (T), and the number of wire crossing (C) coplanar crossing Ccp or multilayer crossing Cml are considered as an evaluation parameter. The generalized QCA evaluation cost function is determined using Eq. (3). The weight metrics for majority gate, wire crossing, and delay, respectively, are the exponential values α, β, and δ Which are considered 2. The cost of multilayer crossing Cml is three times higher than the cost of coplanar crossing Ccp when the manufacturing complexity is taken into account. Table IV displays the results of comparing the proposed 1:1 demultiplexer to its existing counterparts, while Table V shows the results of comparing the proposed 1:4 demultiplexer to its current equivalents [34].

$$Cost_{QCA} = (M^{\alpha} + I + C^{\beta}) \times T^{\sigma},\ \alpha, \beta, \sigma \geq 1 \qquad (2)$$

Based on the comparison given, the offered designs achieve superior results in terms of the number of cells and betterment in the occupied area. Additionally, as compared to its competitors, the provided one to four demultiplexers has a lower QCA cost. Using the same approach, proposed optimum architectures may be utilized to construct higher-order demultiplexers to tackle the problem of latency.

TABLE IV
Performance comparison of the proposed 1:2 Demultiplexer with related works.

1:2 DMUX	**Number of cells**	**Area (μm^2)**	**Crossover type**	**Clock zone**	**Cost**	**Delay**
[39]	56	0.08	Coplanar	4	144	1
[31]	27	0.04	Coplanar	2	24	0.5
[35]	23	0.03	Without	2	20	0.5
[27]	21	0.03	Without	2	20	0.5
[33]	21	0.03	Without	2	20	0.5
[26]	21	0.02	Without	2	20	0.5
Proposed	17	0.01	Without	1	5	0.25

TABLE V
Comparison of the proposed 1:4 Demultiplexer in terms of performance with the previous works.

1:4 DMUX	**Number of cells**	**Area (μm^2)**	**Crossover type**	**Clock zone**	**Cost**	**Delay**
[43]	404	0.60	Coplanar	9	1053	2.25
[44]	212	0.31	Coplanar	8	1056	2
[40]	188	0.22	Coplanar	4	2096	1
[38]	149	0.19	Multilayer	8	3520	2
[41]	110	0.14	Multilayer	3	900	0.75
[42]	125	0.15	Without	6	—	1. 5
[37]	187	0.18	Coplanar	7	1421	1.75
[36]	92	0.12	Coplanar	4	656	1
Proposed	74	0.07	Without	3	351	0.75

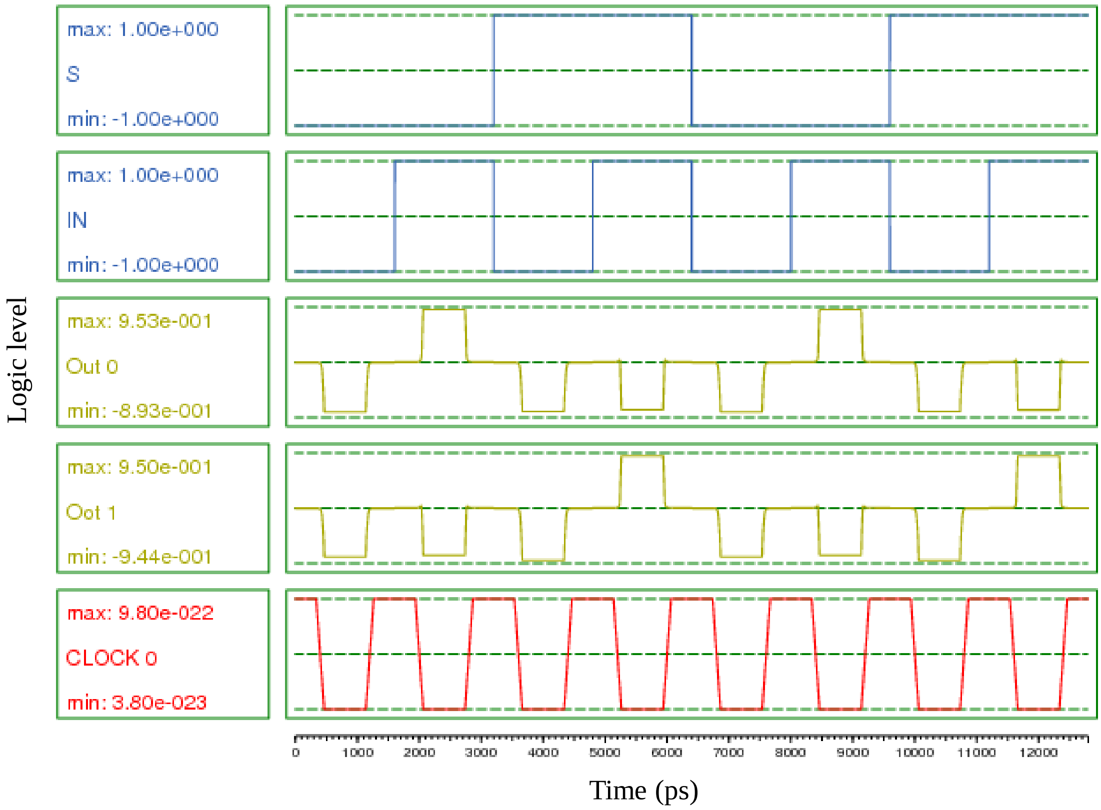

Fig. 10. The proposed 1:2 QCA-DMUX simulation result.

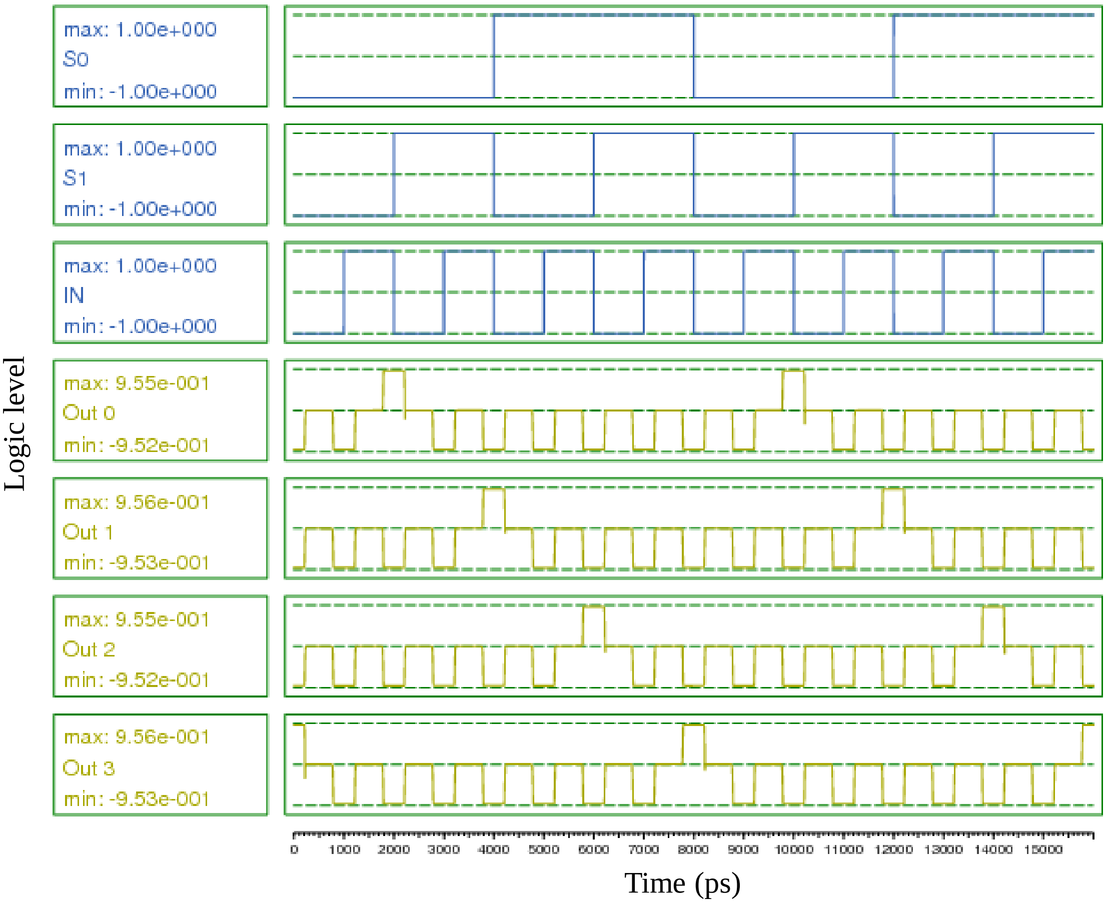

Fig. 11. The proposed 1:4 QCA-DMUX simulation result.

VII. CONCLUSION

This research presented an optimized design for a 1:2 QCA demultiplexer, which serves as the foundation for constructing a novel 1:4 demultiplexer architecture using the Bistable Approximation engine. The proposed circuits were modeled and validated with the QCADesigner tool. A key advantage of both designs is their ability to achieve correct functionality without the need for crossover wires, coplanar arrangements, or rotated cells, thereby enhancing reliability and simplicity. Compared to existing demultiplexer implementations, the proposed architectures are more cost-effective and less complex, while simulation results confirm significant improvements in terms of cell count, latency reduction, and elimination of wire crossings.

FUNDING STATEMENT

This research received no specific grant from any funding agency in the public, commercial, or not-for-profit sectors."

CONFLICTS OF INTEREST

The author declares that there is no conflict of interest regarding the publication of this article.

AUTHORS' CONTRIBUTIONS

Each author’s contributions should be clearly stated using their initials. Contributions may include, but are not limited to:

Conceptualization and study design: Hamidreza Ghaemi Peykani

Manuscript writing and editing: All authors contributed equally to this work.

Supervision and project administration: Morteza Dorrigiv; Mohamad Danaie

STATEMENT ON THE USE OF GENERATIVE AI

AI tools were used to improve the grammatical and English content of this paper.

REFERENCES

[1] DeHon, André, and Michael J. Wilson. "Nanowire-based sublithographic programmable logic arrays." Proceedings of the 2004 ACM/SIGDA 12th international symposium on Field programmable gate arrays. 2004.
[2] Ma, Xiaojun, Jing Huang, and Fabrizio Lombardi. "A model for computing and energy dissipation of molecular QCA devices and circuits." ACM Journal on Emerging Technologies in Computing Systems (JETC) 3.4 (2008): 1-30.
[3] Seminario, Jorge M., et al. "A molecular device operating at terahertz frequencies: theoretical simulations." IEEE Transactions on Nanotechnology 3.1 (2004): 215-218.
[4] Sabbaghi-Nadooshan, Reza, and Moein Kianpour. "A novel QCA implementation of MUX-based universal shift register." Journal of Computational Electronics 13.1 (2014): 198-210.
[5] Rashidi, Hamid, Abdalhossein Rezai, and Sheema Soltany. "High-performance multiplexer architecture for quantum-dot cellular automata." Journal of Computational Electronics 15.3 (2016): 968-981.
[6] Ahmad, Firdous, Ghulam Mohiuddin Bhat, and Peer Zahoor Ahmad. "Novel adder circuits based on quantum-dot cellular automata (QCA)." Circuits and Systems 2014 (2014).

[7] Beigh, Mohammad Rafiq, Mohammad Mustafa, and Firdous Ahmad. "Performance evaluation of efficient XOR structures in quantum-dot cellular automata (QCA)." (2013).

[8] Ajitha, D., K. Venkata Ramanaiah, and V. Sumalatha. "An efficient design of xor gate and its applications using qca." i-Manager's Journal on Electronics Engineering 5.3 (2015): 22.

[9] Singh, Gurmohan, R. K. Sarin, and Balwinder Raj. "A novel robust exclusive-OR function implementation in QCA nanotechnology with energy dissipation analysis." Journal of Computational Electronics 15.2 (2016): 455-465.

[10] Bahar, Ali Newaz, et al. "A novel 3-input XOR function implementation in quantum dot-cellular automata with energy dissipation analysis." Alexandria Engineering Journal 57.2 (2018): 729-738.

[11] Poorhosseini, Mehrdad, and Ali Reza Hejazi. "A fault-tolerant and efficient XOR structure for modular design of complex QCA circuits." Journal of Circuits, Systems and Computers 27.07 (2018): 1850115.

[12] Vankamamidi, Vamsi, Marco Ottavi, and Fabrizio Lombardi. "Clocking and cell placement for QCA." 2006 Sixth IEEE Conference on Nanotechnology. Vol. 1. IEEE, 2006.

[13] Asfestani, Mazaher Naji, and Saeed Rasouli Heikalabad. "A unique structure for the multiplexer in quantum-dot cellular automata to create a revolution in design of nanostructures." Physica B: Condensed Matter 512 (2017): 91-99.

[14] Ahmad, Firdous. "An optimal design of QCA based 2n: 1/1: 2n multiplexer/demultiplexer and its efficient digital logic realization." Microprocessors and Microsystems 56 (2018): 64-75.

[15] Hashemi, Sara, Mostafa Rahimi Azghadi, and Ali Zakerolhosseini. "A novel QCA multiplexer design." 2008 International Symposium on Telecommunications. IEEE, 2008.

[16] Sen, Bibhash, et al. "Modular design of testable reversible ALU by QCA multiplexer with increase in programmability." Microelectronics Journal 45.11 (2014): 1522-1532.

[17] Goswami, Mrinal, et al. "Efficient realization of digital logic circuit using QCA multiplexer." 2014 2nd International Conference on Business and Information Management (ICBIM). IEEE, 2014.

[18] Sen, Bibhash, et al. "Multilayer design of QCA multiplexer." 2013 Annual IEEE India Conference (INDICON). IEEE, 2013.

[19] Seyedi, Saeid, Nima Jafari Navimipour, and Akira Otsuki. "Design and analysis of fault-tolerant 1: 2 demultiplexer using quantum-dot cellular automata nano-technology." Electronics 10.21 (2021): 2565.

[20] Khan, Angshuman, and Rajeev Arya. "Towards cost analysis and energy estimation of simple multiplexer and demultiplexer using quantum dot cellular automata." International Nano Letters 12.1 (2022): 67-77.

[21] Khan, Angshuman, and Rajeev Arya. "Towards the Design and Analysis of Multiplexer/Demultiplexer using Quantum dot Cellular Automata for Nano Systems." *Journal of New Materials for Electrochemical Systems* 25.1 (2022).

[22] Khan, Angshuman, and Rajeev Arya. "Optimal demultiplexer unit design and energy estimation using quantum dot cellular automata." Journal of Supercomputing 77.2 (2021).

[23] Sharma, Vijay Kumar, and Neeraj Kaushik. "Ultra-optimized demultiplexer unit design in quantum-dot cellular automata nanotechnology." e-Prime-Advances in Electrical Engineering, Electronics and Energy 7 (2024): 100445.

[24] Jeon, Jun-Cheol, and Changho Seo. "Quantum-dot cellular automata demultiplexer with minimum design costs with energy dissipation analysis and physical proof for reliable nano-communication systems." *Heliyon* 10.16 (2024).

[25] Aswathy, N., and NM Siva Mangai. "Optimising energy consumption in Nano-cryptography: Quantum cellular automata-based multiplexer/demultiplexer design." IET Quantum Communication 5.4 (2024): 632-640.

[26] Vaid, Nandan, Vijay Kumar Sharma, and Prashant Kumar. "Fundamental 1: 2 demultiplexer design in Quantum-Dot cellular automata Nanotechnology." e-Prime-Advances in Electrical Engineering, Electronics and Energy 8 (2024): 100600.

[27] Afrooz, Sonia, and Nima Jafari Navimipour. "An effective nano design of demultiplexer architecture based on coplanar quantum-dot cellular automata." IET Circuits, Devices & Systems 15.2 (2021): 168-174.

[28] Abdullah-Al-Shafi, Mohammad. "RAM, DEMUX and ALU in nanoscale: a quantum-dot cellular automata-based architecture." Discover Electronics 2.1 (2025): 26.

[29] Vahabi, Mohsen, et al. "Design of an energy efficient approximate BinDCT module in quantum cellular automata." Scientific Reports 15.1 (2025): 19744.

[30] Reshi, Javeed Iqbal, Farooq A. Khanday, and M. Tariq Banday. "Optimized Nanoscale Adder-Subtractor Design Architectures Utilizing Quantum Dot Cellular Automata." Russian Microelectronics 54.4 (2025): 400-426.

[31] Ganesh, E. N., Lal Kishore, and M. J. S. Rangachar. "Implementation of quantum cellular automata combinational and sequential circuits using majority logic reduction method." International Journal of Nanotechnology and Applications 2.1 (2008): 89-106.

[32] Lent, Craig S., and P. Douglas Tougaw. "Lines of interacting quantum-dot cells: A binary wire." Journal of applied Physics 74.10 (1993): 6227-6233.

[33] Huang, Jing, et al. "Tile-based QCA design using majority-like logic primitives." ACM Journal on Emerging Technologies in Computing Systems (JETC) 1.3 (2005): 163-185.

[34] Prasanna, J. Lakshmi, et al. "Design of BCD Adder using Quantum Cellular Automata." International Journal of Advanced Trends in Computer Science and Engineering 9.1 (2020): 574-578.

[35] Vankamamidi, Vamsi, Marco Ottavi, and Fabrizio Lombardi. "Two-dimensional schemes for clocking/timing of QCA circuits." IEEE Transactions on Computer-Aided Design of Integrated Circuits and Systems 27.1 (2007): 34-44.

[36] Afrooz, Sonia, and Nima Jafari Navimipour. "An effective nano design of demultiplexer architecture based on coplanar quantum-dot cellular automata." IET Circuits, Devices & Systems 15.2 (2021): 168-174.

[37] Ahmad, Firdous. "An optimal design of QCA based 2n: 1/1: 2n multiplexer/demultiplexer and its efficient digital logic realization." Microprocessors and Microsystems 56 (2018): 64-75.

[38] Sardinha, Luiz HB, et al. "Nanorouter: a quantum-dot cellular automata design." IEEE Journal on Selected Areas in Communications 31.12 (2013): 825-834.

[39] Nanditha, V. M., et al. "Design and analysis of digital circuits using quantum cellular automata and verilog." 2020 7th International Conference on Computing for Sustainable Global Development (INDIACom). IEEE, 2020.

[40] Iqbal, J., F. A. Khanday, and N. A. Shah. "Design of Quantum-dot Cellular Automata (QCA) based modular 2 n− 1− 2 n MUX-DEMUX." IMPACT-2013. IEEE, 2013.

[41] Chakrabarty, Ratna, et al. "Nano-Calculator using Quantum Dot Cellular Automata (QCA)." 2017 1st International Conference on Electronics, Materials Engineering and Nano-Technology (IEMENTech). IEEE, 2017.

[42] Das, Badhan, et al. "An effective design of 2: 1 multiplexer and 1: 2 demultiplexer using 3-dot QCA architecture." 2019 International Conference on Robotics, Electrical and signal Processing Techniques (ICREST). IEEE, 2019.

[43] Ganesh, E. N., Lal Kishore, and M. J. S. Rangachar. "Implementation of Quantum cellular automata combinational and sequential circuits using Majority logic reduction method." International Journal of Nanotechnology and Applications 2.1 (2008): 89-106.

[44] Shah, N. A., et al. "Design of quantum-dot cellular automata (QCA) based modular 1 to 2n demultiplexers." Int. J. Nontechnology App 5.1 (2011): 47-58.

Semnan University

Journal of Modeling & Simulation in Electrical & Electronics Engineering (MSEEE)

Journal homepage: **https://mseee.semnan.ac.ir/**

ISSN: 2821-0786

Predictive Modeling of NFT Adoption for Enhancing FinTech Applications in Iran’s Banking Sector

Ali Haghi Nojehdeh[1], Mansour Esmaeilpour[2]*, Behrooz Bayat[3] and Alireza Isfandyari Moghaddam[4]

***Abstract*— This research proposes a data-driven modeling framework for the expansion of financial technology (FinTech) in Iran’s banking system through the integration of non-fungible tokens (NFTs). Using a data-mining approach, the study analyzes behavioral data collected from customers of Iranian cryptocurrency exchanges from 2020 to 2025. After preprocessing, the dataset was evaluated with decision trees, Naïve Bayes, neural networks, and rough set algorithms. The results demonstrate that the rough set model achieved the highest predictive accuracy (0.98) in identifying user behavior patterns and the principal factors influencing NFT adoption.**

From a banking and policy-making perspective, the findings highlight the potential of NFT-enabled FinTech platforms to offer innovative tools for digital asset management, enhance transparency, reduce transaction costs, and promote financial inclusion. At the same time, risks such as regulatory uncertainty, cyber fraud, and price volatility emphasize the urgent need for tailored supervisory and governance frameworks that are suited to Iran’s economic environment.

The originality of this study lies in offering a quantitative and simulation-oriented model that bridges theoretical insights with practical applications. By doing so, it provides actionable guidance for the Central Bank of Iran, financial institutions, and regulators to strengthen the digital financial ecosystem and advance the transition toward smart banking.

Keywords: FinTech, NFT, Data Mining, Smart Banking, Blockchain

I. INTRODUCTION

The rapid advancement of information and communication technologies, along with widespread internet penetration, has transformed global economic structures and underscored the need for innovation in financial and banking systems. Financial Technology FinTech, a synthesis of finance and technology emerging from the Fourth Industrial Revolution, plays a central role in reshaping financial business models and facilitating digital transformation within banks. FinTech companies enhance transaction speed, reduce operational costs, and improve the accessibility and quality of financial services [1].

Technologies such as artificial intelligence (AI), blockchain, big data analytics, the Internet of Things (IoT), and cloud computing have revolutionized the delivery of financial services and opened new pathways for innovation in the banking industry [2], [3]. The core objective of FinTech is to provide transparent, efficient, and automated services that expand access to financial resources and promote inclusion across diverse customer segments.

Recent industry analyses predict that digital finance could add more than USD 3.7 trillion to global economic output by 2025 [10], with global FinTech investments surpassing USD 120 billion annually. The 2023 KPMG Pulse of FinTech Report further confirms the sector’s robust growth, particularly in blockchain-based banking services [10].

While FinTech firms were once viewed as competitors to traditional banks, current evidence suggests a complementary

Received; 2025-10-03 Revised; 2025-11-26 Accepted; 2025-12-03

1. Department of Management, Ha.C., Islamic Azad University, Hamedan, Iran.
2. Department of Computer Engineering, Ha.C., Islamic Azad University, Hamedan, Iran.
3. Department of knowledge and information science, Ha.C., Islamic Azad University, Hamedan, Iran.
4. Department of knowledge and information science, Ha.C., Islamic Azad University, Hamedan, Iran.
*Corresponding author: esmaeilpour@iau.ac.ir

Cite this article as:
Haghi Nojehdeh, A., Esmaeilpour M., Bayat, B., and Isfandyari Moghaddam, AR.. (2025). Predictive Modeling of NFT Adoption for Enhancing FinTech Applications in Iran’s Banking Sector. *Journal of Modeling & Simulation in Electrical & Electronics Engineering (MSEEE)*. Semnan University Press . 5 (4), 17-24.
DOI: https://doi.org/10.22075/MSEEE.2025.39256.1230

relationship that strengthens the efficiency and innovation capacity of the financial ecosystem [6], [11]. Consequently, policymakers in both developed and developing economies are increasingly prioritizing the integration of FinTech to enhance monetary effectiveness and financial stability.

In Iran, where the banking sector remains the most dominant financial intermediary, the transition toward FinTech and digital assets presents both substantial opportunities and significant challenges. This study aims to explore data-driven FinTech expansion in Iran's banking sector, emphasizing the emerging role of non-fungible tokens (NFTs) as a tool for financial innovation and inclusion.

II. PROBLEM STATEMENT

The future of Iran's banking industry and the effectiveness of its monetary policies increasingly depend on the successful adoption of FinTech innovations. While global investment in FinTech rose from only USD 800 million in 2008 to over USD 67 billion in 2019 [7], Iran's financial institutions have yet to fully harness these opportunities.

Recent empirical evidence demonstrates that FinTech development significantly affects the liquidity, credit, and market risk measures of Iranian banks (Azari et al. [8]). NFTs, due to their characteristics of digital scarcity, verifiable ownership, and tradeability, offer unique potential for developing asset-backed financing tools, improving liquidity, and diversifying financial portfolios [9], [13].

However, challenges such as legal ambiguity, price volatility, and cyber risks have hindered NFT adoption in Iran. The absence of a localized regulatory and technological framework further limits the integration of NFT-based financial solutions. Therefore, there is an urgent need to design a predictive, data-driven model to identify behavioral factors influencing NFT adoption and to guide the strategic implementation of FinTech solutions in the Iranian banking context.

This research addresses that gap by analyzing user behavior data from Iranian cryptocurrency exchanges (2020–2025) to construct a quantitative model that predicts and enhances NFT adoption as a driver for smart banking development.

III. LITERATURE REVIEW

A. *Theoretical Background*

FinTech represents one of the most transformative developments in the modern digital economy. Its fundamental goal is to deliver faster, cheaper, and more transparent financial services through technology-driven innovation [4], [5]. By integrating blockchain, AI, machine learning, IoT, and cloud computing, FinTech firms now provide diverse services in payments, lending, risk management, and investment.

From a macroeconomic perspective, FinTech reduces transaction costs, increases transparency, enhances operational efficiency, and broadens access to financial resources [8], [32]. However, its adoption brings new challenges, including cybersecurity threats, digital fraud, and regulatory uncertainty [20], [34].

NFTs have recently emerged as a significant element within the FinTech ecosystem. Initially associated with digital art and collectibles, NFTs now serve as financial assets capable of representing ownership rights, collateralizing loans, and creating new financial instruments [35], [41]. The convergence of FinTech, NFTs, and decentralized finance (DeFi) presents new opportunities for innovation but also raises concerns regarding legal frameworks, valuation stability, and data privacy.

B. *Prior Studies*

1) Domestic Studies

Iranian research on FinTech has primarily focused on structural and institutional issues within the banking system. Qazi-Dezfouli [4] conceptualized FinTech as an intersection of financial, legal, and technological dimensions. Ghaemi et al. [5] identified startups as key players in modernizing Iran's banking services, while Madanlou Jouybari et al. [6] emphasized the role of FinTech startups in reducing traditional banking intermediation.

Mohaqer et al. [7] highlighted the dependence of FinTech progress on macroeconomic readiness and interinstitutional cooperation. Recent empirical research, such as that by Mohammadi et al. [8], demonstrated that FinTech development reduces banking risks in Iranian financial institutions. Similarly, Aminipour et al. [8] found that blockchain adoption improves transparency and liquidity control.

Jafari (2024) analyzed the Central Bank's efforts toward national cryptocurrency initiatives, while Asgari et al. (2024) stressed the need for strategic leadership in promoting smart contracts. Importantly, Haghi Nojehdeh et al. [27], [28] introduced process-mining and AI-based modeling frameworks to enhance FinTech operations in Iranian banks, providing methodological precedents that the present study extends.

2) International Studies

International research presents a broad and evolving perspective on FinTech innovation. Abubakar [9] and Milian et al. [23] classified FinTech challenges into business models, data governance, and regulatory adaptation. Svensson et al. [25] examined FinTech–bank collaborations that strengthen legitimacy and competitiveness. Priem [24] explored distributed ledger risks, and Teresiene et al. [21] analyzed the synergy between banking institutions and FinTech platforms.

Recent studies have increasingly explored NFT–FinTech integration. Henrique et al. [14] showed that blockchain-based systems can improve transparency and predictive modeling, while Wu et al. [17] applied fractal and wavelet analyses to NFT price series and identified nonlinear dynamics and abnormal trading patterns that point to potential market-manipulation risks. [19] detected abnormal trading and market-manipulation risk in NFT markets, Xiong & Luo [20] reviewed the global regulatory landscapes for crypto-assets and highlighted persistent legal uncertainty.

The latest empirical and methodological contributions include Jayasuriya and Sims [29], who developed a valuation framework for NFTs; Klein et al. [30], who examined return dynamics of secondary Ethereum-based NFT markets; and Bai et al. [31], who investigated how content characteristics influence customer purchase behavior. In the domain of system security and risk, Das et al. [33] analyzed vulnerabilities within the NFT ecosystem, while Ma et al. [34] provided a systematic review of security challenges related to non-fungible tokens. Furthermore, Fridgen et al. [32] analyzed pricing dynamics and herding behavior in NFT markets. Lastly, Kim et al. [35] proposed a multi-attention recommender system model specialized for NFT markets.

Together, these studies underpin the empirical foundation of our FinTech–NFT modeling approach.

Collectively, these studies provide both theoretical grounding and empirical evidence that justify a data-driven predictive modeling approach tailored to Iran's banking sector.

Synthesis and Research Gap

The review of existing literature indicates that domestic studies on FinTech in Iran have largely concentrated on institutional, regulatory, and structural perspectives, while international research has primarily focused on technological innovations, global risks, and market opportunities. However, despite the rapid expansion of FinTech and the growing significance of digital assets, a substantial research gap remains: the specific role of non-fungible tokens (NFTs) in shaping monetary and banking policies in Iran has not been adequately addressed.

This gap is particularly critical given the increasing convergence of FinTech, NFTs, and decentralized finance (DeFi), which are now recognized as key pillars of the digital economy. Addressing this issue is not only theoretically relevant but also of high practical importance for policymakers, financial institutions, and regulators in Iran.

The present study contributes to filling this void by developing a data-driven, simulation-oriented model based on data mining of Iranian cryptocurrency exchange users. Unlike prior research that has remained descriptive or conceptual, this work employs quantitative modeling and predictive analysis to identify behavioral patterns and adoption drivers of NFTs in Iran's financial ecosystem. By doing so, it provides an empirically grounded framework that can guide the Central Bank and financial institutions in policy design, risk management, and the strategic integration of FinTech and NFTs into the national banking system.

IV. Research Methodology

A research methodology provides the structural foundation for conducting a scientific investigation, ensuring that the process follows systematic, validated, and replicable procedures. In this study, an experimental–quantitative framework based on data-mining techniques is adopted to identify behavioral patterns and key determinants influencing NFT adoption among Iranian cryptocurrency exchange users.

The methodology consists of three core components:
(1) data collection and preprocessing,
(2) predictive modeling framework, and
(3) implementation of selected algorithms.

A. Statistical Population

Data were collected from verified Iranian cryptocurrency exchanges under confidentiality and data-sharing agreements covering the period 2020-2025. All datasets were anonymized prior to analysis to comply with ethical and privacy guidelines.

The final dataset includes 800 anonymized user profiles, consisting of:

- Demographic attributes: gender, age, user type (investor/trader)
- Transactional features: price, trading volume, time, volatility
- Behavioral indicators: NFT purchase frequency, token preferences, holding duration

Standard preprocessing procedures, including normalization, outlier removal, and mean-based missing-value imputation, were applied. The final dataset was divided into 70% training and 30% testing subsets for predictive analysis.

B. Sampling Method

The statistical population consists of active participants in Iran's cryptocurrency ecosystem-investors, traders, financial analysts, and blockchain developers. A stratified random sampling strategy was used to ensure proportional representation across demographic and behavioral categories.

The sample size of 800 users was determined based on data availability and statistical adequacy for predictive model development. As illustrated in Fig. 1, the gender distribution of the sample shows that male users constitute the majority of cryptocurrency exchange participants. Fig. 2 presents the NFT purchase behavior of users, indicating that a considerable proportion of participants have prior experience with NFT transactions. Furthermore, Fig. 3 demonstrates the cross-distribution of gender and NFT purchase decisions, highlighting observable differences in adoption behavior between male and female users.

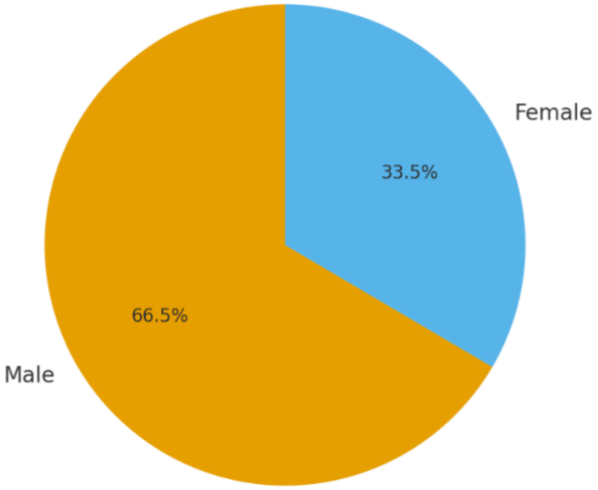

Fig 1. Sample size by gender(531 males, 267 females)

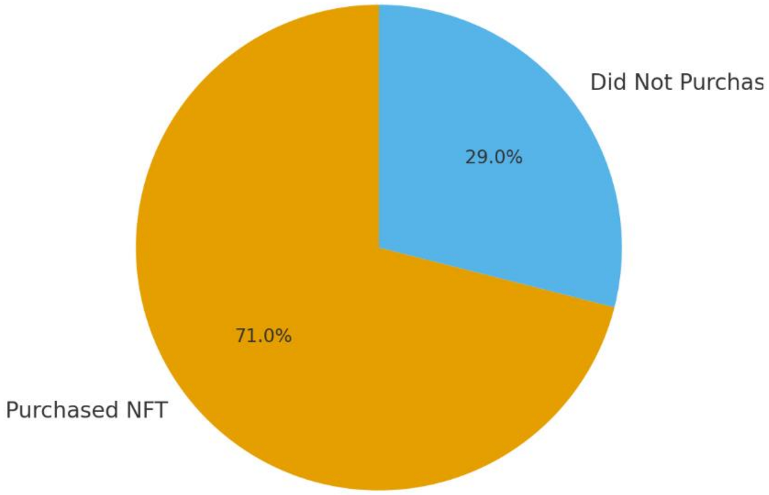

Fig 2. NFT purchase behavior (503 buyers, 205 non-buyers)

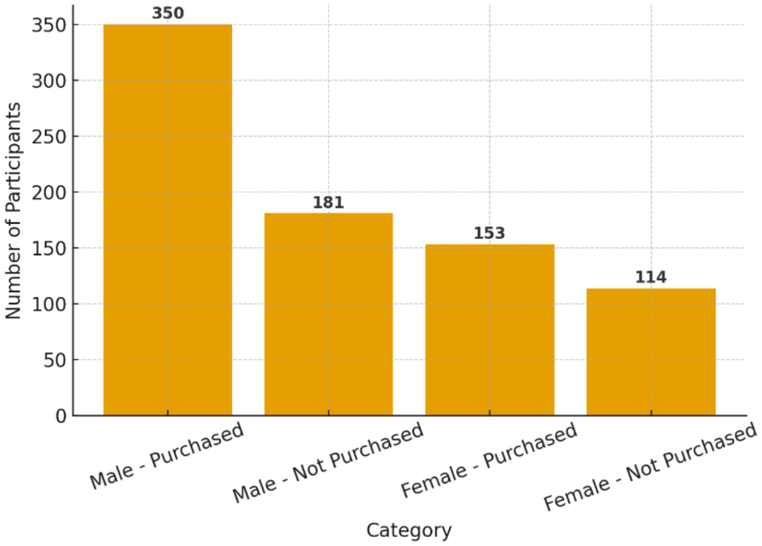

Fig 3. Cross-distribution of gender and NFT purchase decision

C. Predictive Modeling Framework

Predictive modeling was performed to identify behavioral determinants of NFT adoption. Several data-mining algorithms were tested, and four models were selected due to their predictive accuracy and computational efficiency:

- Decision Tree (J48)
- Naïve Bayes
- Rough Set Model
- Artificial Neural Network (ANN)

Decision-tree and rough-set approaches are widely used for classification and pattern-extraction tasks due to their interpretability and robustness [37].

All models were implemented using WEKA 3.9 and Rosetta 1.4.5, following a 10-fold cross-validation protocol.

For the ANN, parameter tuning included:
– 100 hidden neurons,
– learning rate = 0.3,
– momentum = 0.2.

Algorithms that did not contribute to the final analytical process were excluded to maintain methodological clarity and focus.

V. DATA ANALYSIS

This section presents the data analysis procedures and findings derived from the implemented data-mining algorithms. The goal is to extract meaningful patterns that explain the behavioral determinants of NFT adoption within Iran’s FinTech ecosystem. All analyses were performed using WEKA 3.9 and Rosetta 1.4.5. The preprocessed dataset was divided into training (70%) and testing (30%) subsets to evaluate model performance and generalizability.

A. Evaluation Metrics

To ensure consistent comparison across models, standard machine-learning evaluation metrics were used:

- **Accuracy**

Accuracy = (TP+TN) / (TP + FP + TN + FN)

- Sensitivity (Recall)

Recall=TP / (TP + FN)

- **Precision (PPV)**
- Precision (PPV) = TP / (TP + FP)2020–2025F1-Score

F1 Score = 2 × ((Precision*Recall) / (Precision+Recall))

- **Error Rate**

Error Rate=FP+FN / (TP+TN+FP+FN)

- **Negative Predictive Value (NPV)**

NPV=TN / (TN + FN)

- **Specificity**

Specificity=TN / (TN + FP)

Confusion Matrix Used in Calculations

TABLE I

Confusion Matrix for NFT Adoption Classification

	Predicted Negative	**Predicted Positive**
Actual Positive	16	784
Actual Negative	0	179

The confusion matrix used for calculating the evaluation metrics is presented in Table I.

Although specificity is low due to limited negative cases, high accuracy, recall, precision, and F1-score collectively indicate robust model performance.

B. Pattern Discovery Using Rough Set Model

The Rough Set model extracted transparent rule sets based on demographic and behavioral attributes. It revealed strong associations involving age group, gender, financial literacy, and prior market experience.

- Achieved highest accuracy: 0.98
- Identified financial literacy and market experience as the most influential determinants
- Produced interpretable rule structures suitable for FinTech policy design

C. Pattern Discovery Using Genetic Algorithm (GA)

A Genetic Algorithm was applied to optimize and refine the large rule base produced by the Rough Set model.

- Over 2,000 initial rules generated
- High-confidence optimized rules emphasized:
  - financial literacy
  - risk tolerance
  - previous trading experience

Users with a university education, moderate risk tolerance, and prior exposure to digital markets showed the highest NFT adoption likelihood.

D. Pattern Discovery Using Decision Tree (J48)

The J48 decision tree provided a clear hierarchical rule structure:

- Financial literacy was the strongest predictor
- Followed by the monthly trading volume and the age group

Results showed:

- 486 financially literate users purchased NFTs,
- while most users lacking literacy did not.

Accuracy achieved: 0.977

E. Pattern Discovery Using Naïve Bayes

Naïve Bayes achieved an accuracy of 0.977, consistent with the decision tree.

Findings demonstrated that:

- Experienced male investors aged 30–45
- With strong financial literacy
- And moderate risk perception

had the highest predicted probability of NFT adoption.

F. Pattern Discovery Using Artificial Neural Networks (ANN)

The ANN model captured nonlinear interactions among behavioral variables.

Network structure:

- 1 input layer
- 2 hidden layers
- 1 output layer

Training parameters:

- learning rate = 0.3
- momentum = 0.2

Accuracy: 0.938

Although lower than rule-based models, ANN identified complex relationships, particularly interactions involving financial literacy, transaction frequency, and income.

TABLE II

Comparative Performance of Data-Mining Algorithms

Algorithm	**Accuracy**	**Key Predictors Identified**
Rough Set Model	**0.980**	Financial literacy, trading experience, and age
Decision Tree (J48)	**0.977**	Financial literacy, transaction volume, risk tolerance
Naïve Bayes	**0.977**	Financial literacy, prior experience, and income
Neural Network (ANN)	**0.938**	Nonlinear behavioral and demographic interactions

Table II summarizes the comparative performance of all implemented algorithms in terms of predictive accuracy and key behavioral determinants.

The Rough Set model offered the best balance of accuracy and interpretability.

G. Summary of Findings

Across all models, four variables consistently emerged as the strongest predictors of NFT adoption:

- Financial literacy
- Risk tolerance
- Prior market experience
- Transaction volume

These findings support the use of data-driven strategies for designing NFT-based financial services and for guiding digital transformation initiatives in Iran’s banking sector.

IV. CONCLUSION

This study applied four advanced data-mining algorithms-Decision Tree (J48), Naïve Bayes, Neural Networks, and the Rough Set model-to analyze behavioral data from 800 users of Iranian cryptocurrency exchanges. The aim was to identify key demographic and behavioral determinants of NFT adoption and develop a predictive framework to support FinTech expansion in Iran's banking sector.

Comparative results showed that the Rough Set model achieved the highest predictive accuracy (0.98), outperforming the Decision Tree (0.977), Naïve Bayes (0.977), and Neural Network (0.938). These findings highlight the importance of appropriate data preprocessing, model selection, and interpretability-oriented analytical methods for behavioral prediction in digital asset markets.

The overall predictive accuracy of the applied models is reported in Table III.

TABLE III

Predictive Accuracy of the Applied Models

Algorithm	**Accuracy**
Rough Set Model	**0.980**
Decision Tree (J48)	0.977
Naïve Bayes	0.977
Neural Networks	0.938

The results confirm that rule-based models, particularly the Rough Set approach, offer an effective balance between predictive accuracy and interpretability, making them suitable for banking policymakers and financial analysts who require transparent and data-driven decision-support tools.

A. Discussion

The models consistently identified financial literacy, risk tolerance, previous market experience, and transaction volume as the most influential factors affecting NFT purchase decisions.

The Rough Set model provided the clearest and most interpretable rules, enabling policymakers to understand how demographic and behavioral variables combine to drive adoption. While neural networks captured nonlinear interactions, their limited interpretability reduces their direct applicability in regulatory or banking environments where transparency is essential.

Overall, the findings demonstrate that data-mining methods are powerful tools for analyzing emerging digital-finance behaviors and can assist banks in designing targeted, customer-centric FinTech services, particularly in the rapidly evolving domains of NFTs and decentralized finance (DeFi).

B. Comparative Insights with Prior Research

The findings align with and extend recent studies in the fields of FinTech, user behavior, and predictive analytics:

1. Machine Learning in Finance

Prior studies, such as those by Kim (2003) and Henrique et al. (2019), demonstrated the strong predictive capabilities of AI-based algorithms. The present study supports these results while emphasizing the added interpretability of Rough Set rules in policy settings.

2. Behavioral Segmentation

Research by Sujatha et al. (2023) showed that segmenting users by financial literacy improves personalization. This study confirms similar segmentation potential using rule-based methods.

3. FinTech Innovation and Adoption

Results are consistent with Mohammadi et al. (2023) and Ali Haghi Nojehdeh et al. (2023), who found that data-driven approaches enhance FinTech development and behavioral prediction.

4. Hybrid Modeling

Echoing Subbarao et al. (2020), future frameworks may benefit from combining interpretable rule-based approaches with nonlinear neural models to improve performance.

5. Behavioral and Regulatory Context

Recent studies (e.g., Waliullah et al., 2025; Chandrasekaran, 2025) emphasize risk perception and regulatory clarity as key determinants of digital asset adoption—a pattern also observed in the Iranian context.

C. Policy Implications

The findings provide several practical insights for Iranian banking policymakers and FinTech regulators:

- Enhancing Financial Literacy

Education programs should be prioritized to increase awareness, trust, and responsible participation in digital asset markets.

- Supporting Smart Banking Initiatives

Data-mining models can help identify customer groups with high NFT adoption potential, enabling targeted product development.

- Strengthening Risk-Management Systems

Rule-based models, such as Rough Set, can inform risk assessments by highlighting behavioral indicators of high-risk or high-value customers.

- Developing Regulatory Infrastructure

Clear legal frameworks for NFTs and digital assets will support secure and transparent FinTech expansion.

D. Recommendations for Future Research

Future studies can extend the present work in several directions:

1. Hybrid Model Development

Integrate Rough Set models with advanced neural architectures to balance interpretability and nonlinear accuracy.

2. Sentiment Analysis

Examine social-media sentiment and psychological factors affecting NFT investment behavior.

3. Cross-Domain Application

Test the predictive framework in other FinTech areas such as decentralized lending, insur-tech, or digital payment systems.

4. Longitudinal Studies

Use multi-year datasets to analyze evolving behavioral and market dynamics over time.

E. Final Remarks

This study demonstrates that AI-driven and data-mining models can play a transformative role in supporting

FinTech development in emerging economies. By prioritizing financial literacy, risk assessment, and data-driven decision-making, Iranian banking institutions can accelerate the transition toward smart banking and a sustainable digital financial ecosystem.

F. Ethical and Privacy Compliance

All user data were fully anonymized prior to analysis and handled in accordance with national data-protection regulations and generally accepted ethical research standards. No identifiable or sensitive personal information was collected at any stage of the study.

ACKNOWLEDGMENTS

The authors would like to express their sincere appreciation to the Iranian cryptocurrency exchanges that cooperated by providing anonymized data for this study. The authors also thank the anonymous reviewers and the editorial team for their valuable comments and constructive suggestions, which significantly contributed to improving the quality of the manuscript.

FUNDING STATEMENT

This research received no specific grant from any funding agency in the public, commercial, or not-for-profit sectors.

CONFLICTS OF INTEREST

The authors declare that there is no conflict of interest regarding the publication of this article.

AUTHORS' CONTRIBUTIONS

The first author primarily contributed to the conceptualization, data analysis, and development of the core research content. The corresponding author was responsible for overall supervision, research framework design, and coordination of the study. The third and fourth authors contributed through academic guidance, methodological support, and critical review of the manuscript. All authors read and approved the final version of the manuscript.

STATEMENT ON THE USE OF GENERATIVE AI

The authors confirm that generative artificial intelligence tools were used solely for language editing and improving the clarity of the manuscript. All content was carefully reviewed and validated by the authors, who take full responsibility for the accuracy, integrity, and originality of the work.

REFERENCES

[1] M. Asadollah, R. Sanavifard, and A. Hamidizadeh, "Electronic banking business model based on the emergence of FinTechs and financial startups," Technology Development Management, vol. 7, no. 2, pp. 195–248, 2019 (in Persian).

[2] H. Danaeifard, S. M. Alvani, and A. Azar, Qualitative Research Methodology in Management: A Comprehensive Approach. Tehran: Safar Publications, 2011 (in Persian).

[3] A. Rubini, FinTech at a Glance: Financial Technology in Simple Language (Transl. E. Rouhi, R. Ghorbani). Tehran: Shabakeh Rah-e Pardakht, 2017 (in Persian).

[4] S. Ghazi-Dezfouli, "Introduction to the emerging FinTech industry," 2016. [Online]. Available: https://www.aparat.com/v/qFcKd (in Persian).

[5] M. Ghaemi, M. A. Dehghan-Dehnavi, and N. Sadat-Moradi, "Examining the status of banking startups in the field of modern banking services (Case study: Iranian banking system)," Islamic Economics and Banking, vol. 17, no. 20, pp. 119–139, 2017 (in Persian).

[6] A. Modanlou-Jouibari, M. Kazemnejad, and S. A. Kazemnejad, "Concepts, fields, activities and the FinTech startup industry in Iran and the world," Proc. 1st Conf. Electrical and Computer Engineering, Qaemshahr, Iran, 2018 (in Persian).

[7] A. Mohaqer, F. Seghafi, N. Mokhtarzadeh, and M. Azadeganmehr, "Predicting the technological transformation pattern in Iran's financial services sector based on a multi-level transition approach," Science and Technology Policy, vol. 11, no. 4, pp. 77–98, 2019 (in Persian).

[8] Azari, M., Gholizadeh, M. H., Jamshidi, R., & Sadeghi, M. E., "Examining the impact of fintech on liquidity, credit, and market risks in the banking industry," International Journal of Innovation in Engineering, vol. 3, no. 4, pp. 13–27, 2023. doi: 10.59615/ijie.3.4.13.

[9] A. Bakkar, "FinTech and the future of finance," 2019. [Online]. Available: https://www.hlb.global/fintech-and-the-future-of-finance

[10] Capgemini, World FinTech Report, 2020.

[11] R. Chen, C. Huiwen, J. Chenglu, and Y. Lean, "Linkages and spillovers between internet finance and traditional finance: Evidence from China," Emerging Markets Finance and Trade, vol. 56, pp. 1196–1210, 2020.

[12] P. Gomber, J. A. Koch, and M. Siering, "Digital finance and FinTech: Current research and future research directions," Journal of Business Economics, vol. 87, no. 5, pp. 537–580, 2017.

[13] A. Guadamuz, "The treachery of images: Non-fungible tokens and copyright," Journal of Intellectual Property Law & Practice, vol. 16, no. 12, pp. 1367–1386, 2021.

[14] B. M. Henrique, V. A. Sobreiro, and H. Kimura, "Literature review: Machine learning techniques applied to financial market prediction," Expert Systems with Applications, vol. 124, pp. 226–251, 2019.

[15] J. Liu, X. Li, and S. Wang, "What have we learnt from 10 years of FinTech research? A scientometric analysis," Technological Forecasting and Social Change, vol. 155, pp. 1–13, 2020.

[16] M. Nadini, L. Alessandretti, F. Di Giacinto, M. Martino, L. M. Aiello, and A. Baronchelli, "Mapping the NFT revolution: Market trends, trade networks, and visual features," Scientific Reports, vol. 11, no. 1, pp. 1–11, 2021.

[17] H. Wu, Y. Zhang, and J. Li, "Nonlinear dynamics of NFT global prices: Evidence from fractal and wavelet analysis," Finance Research Letters, vol. 61, 105511, 2024.

[18] I. Pollari and A. Ruddenklau, The Pulse of FinTech 2018: Biannual Global Analysis of Investment in FinTech, KPMG International Cooperative, 2019.

[19] Mingxiao Song, Yunsong Liu, Agam Shah, Sudheer Chava, 'Abnormal Trading Detection in the NFT Market,' arXiv preprint, 2023, DOI:10.48550/arXiv.2306.04643

[20] X. Xiong & J. Luo, 'Global Trends in Cryptocurrency Regulation: An Overview,' arXiv preprint, 2024, DOI:10.48550/arXiv.2404.15895

[21] D. Teresiene, R. Pu, I. Pieczulis, J. Kong, and X. Yue, "The interaction between banking sector and financial technology companies: Qualitative assessment – A case of Lithuania," Risks, vol. 9, no. 10, p. 21, 2021.

[22] M. Magomedov, N. Reshetnikova, and D. Buklanov, "Digital finance technologies: Threats and challenges to the global and national financial security," IOP Conf. Ser.: Earth Environ. Sci., vol. 666, p. 062139, 2021.

[23] E. Z. Milian, M. d. M. Spinola, and M. M. Carvalho, "FinTechs: A literature review and research agenda," Electronic Commerce Research and Applications, 2019. [Online]. Available: https://doi.org/10.1016/j.elerap.2019.100833

[24] R. Priem, "Distributed ledger technology for securities clearing and settlement: Benefits, risks, and regulatory implications," Journal of Financial Innovation, vol. 6, no. 11, pp. 1–25, 2020.

[25] C. Svensson, J. Udesen, and J. Webb, "Alliances in financial ecosystems: A source of organizational legitimacy for FinTech startups and incumbents," Technology Innovation Management Review, vol. 9, no. 1, pp. 20–32, 2019.

[26] P. S. Rao, K. Srinivas, and A. K. Mohan, "A survey on stock market prediction using machine learning techniques," in Proc. 1st Int. Conf. on Data Science, Machine Learning and Applications (ICDSMLA 2019), Springer, pp. 923–931, 2020.

[27] A. Haghi Nojehdeh, M. Esmaeilpour, B. Bayat, and A. Isfandyari Moghaddam, "Improving Financial Technology (FinTech) in Banks Using Process Mining Algorithms," Modeling and Simulation in Electrical and Electronics Engineering, vol. 3, no. 3, pp. 41–50, 2023.

[28] A. Haghi Nojehdeh, M. Esmaeilpour, B. Bayat, and A. Isfandyari Moghaddam, "Investigating Factors Affecting the Cost of Money in

Iranian Banks Based on Artificial Intelligence and Using Data Mining," Modeling and Simulation in Electrical and Electronics Engineering, vol. 3, no. 1, pp. 37–45, 2023.

[29] D. Jayasuriya and A. Sims, "Not so new kid on the block: Accounting and valuation aspects of non-fungible tokens (NFTs)," Journal of Risk and Financial Management, vol. 16, no. 11, p. 465, 2023. DOI: 10.3390/jrfm16110465

[30] Niklas Konstantin Klein, Fritz Lattermann, Dirk Schiereck, "Investment in non-fungible tokens (NFTs): the return of Ethereum secondary market NFT sales," Journal of Asset Management, vol. 24, no. 4, 2023. DOI: 10.1057/s41260-023-00316-1

[31] Z. H. Bai, C. Xu, and S. E. Cho, "Content characteristics and customer purchase behaviors in non-fungible token digital artwork trading," Journal of Theoretical and Applied Electronic Commerce Research, vol. 20, no. 2, art. 65, 2025.

[32] Fridgen, G., Kräussl, R., Papageorgiou, O., & Tugnetti, A. (2025). Pricing dynamics and herding behaviour of NFTs. European Financial Management, 31(2), 670-710.

[33] Dipanjan Das, Priyanka Bose, Nicola Ruaro, Christopher Kruegel, Giovanni Vigna, "Understanding Security Issues in the NFT Ecosystem," arXiv, 2022. DOI: 10.48550/arXiv.2111.08893

[34] Kai Ma, Jintao Huang, Ningyu He, Zhuo Wang, Haoyu Wang, "SoK: On the Security of Non-Fungible Tokens," arXiv, 2025.

[35] Kim, S., Lee, Y., Kim, Y., Hong, J., & Lee, Y, "NFTs to MARS: Multi-Attention Recommender System for NFTs," Expert Systems with Applications, vol. 225, 120142, 2023.

[36] S. Barua, "Implications of NFT as a sustainable fintech innovation for sustainable development and entrepreneurship," *Journal of Sustainable Finance & Investment*, vol. 15, no. 2, pp. 210–228, 2025.

[37] A. Abrishami, Artificial Intelligence Techniques in Economic and Financial Forecasting. Tehran: Negahe Danesh Press, 2006 (in Persian).

Journal of Modeling & Simulation in Electrical & Electronics Engineering Vol 5 (4). 25-34.

Semnan University

Journal of Modeling & Simulation in Electrical & Electronics Engineering (MSEEE)

Journal homepage: **https://mseee.semnan.ac.ir/**

ISSN: 2821-0786

Fractional Fuzzy Adaptive Methodology for Fractional-order Non-Affine Nonlinear Systems: Application to Gyroscope

Reza Ghasemi[1*], Bita Sadat Ghazanfarpour[2] Farideh Shahbazi[3] and Mahmood Mahmoodi[4]

***Abstract*— This study employs a fractional fuzzy adaptive methodology to design procedures for fractional-order non-affine nonlinear systems. The significant evolution of fractional-order calculus in science and engineering has made this area one of the most widespread fields, particularly in control engineering. Fractional-order fuzzy adaptive controller (FAC) has involved numerous scientists to improve appropriate controllers for non-affine nonlinear systems because of: 1) reconfigurable framework, the performance of the FAC is superior to that of the fuzzy controllers, 2) using the experts' data, FAC can apply the expert knowledge in the controller procedure rather than adaptive ones, and 3) enhancement of the controller routine instead of the integer-order one. In addition, this approach can control nominal systems in the presence of both external disturbances and uncertainties. The fractional-order adaptation laws are developed to guarantee the stability of the closed-loop system using a fractional-order Lyapunov approach. Unlike other research that focuses on fractional-order affine nonlinear systems, our approach specifically addresses fractional-order nonaffine nonlinear systems. Finally, the performance of the proposed methodology on chaotic systems, a gyroscope, and an inverted pendulum indicates the capability of the proposed scheme.**

Keywords— Non-Affine Nonlinear System, Adaptive Control, Fractional Order (FO) Systems, Fractional-Order Lyapunov Stability, Fuzzy System.

I. INTRODUCTION

Fractional Order Calculus (FOC), despite a history of over years in mathematics, has recently received much attention as a new subject in engineering and basic sciences. FOC, which has a greater degree of freedom than integer-order calculus by generalizing derivative and integral order to real numbers, has a variety of applications in electronics, telecommunications, control, mechanics, physics, and even medicine [4]. FOC has a noticeable advantage over integer order calculations, as is investigated in various studies for heat transfer process modeling [4], electrochemical processes [4], biological systems [5], diffusion procedure in batteries [6], dielectric polarization, viscoelastic systems, and electromagnetic waves [7].

Furthermore, fractional-order controllers have shown a more significant performance than integer-order controllers. For the first time, Oustaloup provided a new way for fractional-order calculations to enter control by introducing a robust fractional-order controller called commande robuste d'ordre non entier (CRONE) [8]. Consequently, many articles and research were presented to control fractional-order systems or introduce new procedures in fractional-order controllers. These include fractional-order Proportional-Integral-derivative (PID) controllers [9]-[10], fractional-order model reference controllers [11]-[12], and synchronization of chaotic fractional-order nonlinear systems [13]-[16]. Also, due to differences in the concept of energy in fractional and integer order systems, new ideas of stability of

Received; 2025-07-13 Revised; 2025-12-06 Accepted; 2025-12-27

1. Department of Electrical Engineering, University of Qom, Qom, Iran.
2. Department of Electrical Engineering, University of Qom, Qom, Iran.
3. Department of Mathematics, University of Qom, Qom, Iran.
4. Department of Mathematics, University of Qom, Qom, Iran.
*Corresponding author: r.ghasemi@qom.ac.ir, reghasemi@gmail.com

Cite this article as:

Ghasemi, R., Ghazanfarpour, B. S., Shahbazi, F., and Mahmoodi, M.(2025). Fractional Fuzzy Adaptive Methodology for Fractional-order Non-Affine Nonlinear Systems: Application to Gyroscope. *Journal of Modeling & Simulation in Electrical & Electronics Engineering (MSEEE)*. Semnan University Press . 5 (4), 25-34.

DOI: https://doi.org/10.22075/MSEEE.2025.38323.1218

fractional order systems and Lyapunov theory have been introduced and considered in [17]-[18].

In [19], a novel terminal sliding mode observer is developed using neural networks for a nonlinear system. Moreover, authors in [20] deal with fractional nonsingular terminal sliding mode controllers for nonlinear fractional-order chaotic systems.

On the other hand, fuzzy systems are valuable for employing expert knowledge and have received considerable attention within the control field in the last two decades [1]. The importance of fuzzy systems lies in designing controllers based on experts' knowledge. Also, it has been proven that if the required conditions are met, fuzzy systems are comprehensive approximators and can estimate any continuous nonlinear function of any degree. They are also referred to as model-independent control methods. In addition, fuzzy logic has been able to open its place in adaptive control with different structures, and adaptive fuzzy control has shown promising performance.

Since fractional order calculus has recently developed in control systems, the combination of fractional order systems and adaptive fuzzy controllers is considered a novel field in intelligent control engineering and research. The first fractional order fuzzy adaptive controller was presented by Onder Efe in 2008 to guide a two-degree-of-freedom robot arm with an integer dynamic model [21]. The study [22] covers the sliding mode and indirect fuzzy adaptive controller to synchronize fractional-order nonlinear chaotic systems. Also in [23], the H^∞fuzzy adaptive controller is designed to synchronize the fractional-order nonlinear system. In [24], an adaptive fuzzy controller and sliding mode approach are used for fractional-order time-delayed nonlinear systems. However, the disadvantage of [22]-[24] is the lack of sufficient accuracy in fractional-order mathematical calculations, which makes the results unusable. The authors in [25]-[27] propose a fractional-order nonlinear system based on a hybrid fuzzy adaptive controller, which uses improper fractional-order calculus equations. Furthermore, [27] uses integer-based Lyapunov's theorem to prove fractional-order systems incorrectly.

In [30], an interval type-2 fuzzy adaptive controller is presented for both synchronization and stabilization of chaotic nonlinear fractional-order systems. In [31], a fuzzy adaptive controller is applied to synchronize and stabilize fractional-order nonlinear systems in the presence of uncertainties. Sliding mode control is a common technique to control fractional-order systems with uncertainty and external disturbances [34]-[35]. In [36], the adaptive fuzzy controller has been applied to fractional order uncertain systems in the presence of input constraints. The adaptive fuzzy approach can also be used for time-delayed systems [37]. Various adaptive methods have been proposed for fault tolerance in fractional-order systems [38]-[39]. Authors in [42] deal with a fuzzy adaptive consensus controller for a class of incommensurate fractional-order systems. The FO sliding mode controller is developed for a class of affine nonlinear systems in [43].

The primary disadvantages of the proposed method are two-fold:

1) Neither of the referenced studies examines fractional nonaffine nonlinear systems.

2) In designing an adaptive controller for an unknown nonlinear system, most sources rely on approximating the unknown functions of the system using a fuzzy system based on the Lyapunov theorem. This approach significantly increases the computational burden.

The present article proposes a fractional-order adaptive fuzzy strategy that controls uncertain nonlinear fractional-order systems in the presence of disturbances. The advantage of the proposed method is that it overcomes the uncertainty and external disturbance in the nonlinear fractional model. A Fuzzy system is considered to estimate the control input as a universal approximator and to apply the experts' knowledge in designing controller procedures. The closed-loop stability is guaranteed in the sense of Lyapunov.

The organization of the paper is explained as follows: a review of the preliminary concepts of fractional calculus and the fuzzy system is provided in Section 2. The problem statement is presented in Section 3. The design of fractional fuzzy adaptive control is proposed in Section 4. Section 5 is dedicated to illustrating the numerical simulations. Eventually, a brief summarization is presented in the last section.

II. PRELIMINARIES

The present section intends to discuss the pivotal preliminary, stability definitions, the fractional calculus, which relies on Mittag-Leffler theory, and fuzzy logic systems.

Fractional Calculus

For a better understanding of fractional-order systems, this section briefly examines these systems.

A critical role is associated with fractional calculus in recent contexts. The differential equations of fractional order are applied to describe the control system. The arbitrary orders of derivatives and integrals are indeed allowed by fractional calculus. The definition of a general calculus operator (comprising both fractional and integral orders) is presented as [40]:

$$
{}_aD_t^q = \begin{cases} \dfrac{d^q}{dt^q}, & q > 0 \\ 1, & q = 0 \\ \displaystyle\int_a^t (d\tau)^{-q}, & q < 0 \end{cases}
$$

Where q and a are arbitrary real numbers. Below, the description of three common definitions for the fractional derivative and integral is presented.

Definition 1: [28] The q-order Grunwald - Letnikov (GL), Riemann-Liouville (RL), and Caputo(C) derivatives of the function $f(t)$ are described as:

$$
{}_a^{GL}D_t^q f(t) = \lim_{N\to\infty}\left[\frac{t-a}{N}\right]^{-q}\sum_{j=0}^{N-1}(-1)^j q_j\ f\left(t-j\left[\frac{t-a}{N}\right]\right)
$$

$$
{}_a^{RL}D_t^q f(t) = \frac{1}{\Gamma(1-q)}\frac{d}{dt}\int_a^t (t-\tau)^{-q} f(\tau)d\tau
$$

$$
{}_a^{C}D_t^q f(t) = \frac{1}{\Gamma(1-q)}\int_a^t (t-\tau)^{-q}\dot{f}(\tau)d\tau \tag{1}
$$

where $0 < q < 1$ and $\Gamma(.)$ is the Gamma function.

Definition 2: [28] The q- order Riemann-Liouville fractional integral of $f(t)$ is defined as:

$$
{}_aD_t^{-q} f(t) = \frac{1}{\Gamma(q)}\int_a^t (t-\tau)^{q-1} f(\tau)d\tau. \tag{2}
$$

Definition 3: [28] The Mittag-Leffler function for solving fractional order systems is defined likewise the exponential function applied to solving integer-order systems, as follows:

$$E_{\alpha}(z) = \sum_{k=0}^{\infty} \frac{z^k}{\Gamma(\alpha k+1)} \tag{3}$$

where $\alpha > 0$.

The next equation explains the Mittag-Leffler function in terms of two parameters:

$$E_{\alpha,\beta}(z) = \sum_{k=0}^{\infty} \frac{z^k}{\Gamma(\alpha k+\beta)} \tag{4}$$

where $\alpha > 0$ and $\beta > 0$. For $\beta = 1$, we have $E_{\alpha,1}(z) = E_{\alpha}(z)$. Also $E_{1,1}(z) = e^z$.

According to various references, the most suitable definition for engineering applications is the Caputo (C) approach.

Definition 4: [28] (Mittag-Leffler Stability) The solution of ${}_{0}^{C}D_{t}^{q}x(t) = f(x,t)$ is considered to be Mittag-Leffler stable if

$$\| x(t) \| \leqslant \left\{m[x(t_0)](t-t_0)^{-\gamma}E_{\alpha,1-\gamma}(-\lambda(t-t_0)^{\alpha})\right\}^{b} \tag{5}$$

where $\alpha \in (0,1)$, $\gamma \in [0,1-\alpha]$, $b > 0$, $m(0) = 0$, $m(x) \geq 0$, $m(x)$ is locally Lipschitz on $x \in B \subseteq \mathbb{R}^n$ with Lipschitz constant, and t_0 is the initial time.

Theorem 1: [28] Let $x = 0$ be an equilibrium point for the system ${}_{0}^{C}D_{t}^{q}x(t) = f(x,t)$ and $D \subseteq \mathbb{R}$ be a domain containing zero. Let $V\big(t,x(t)\big)\colon [0,\infty) \times D \to \mathbb{R}$ be a continuously differentiable function and locally Lipschitz with respect to in order that

$$\begin{gathered} \alpha_1 \| x \|^{a} \leq V(t,x(t)) \leq \alpha_2 \| x \|^{ab} \\ {}_{0}^{C}D_{t}^{\beta}V(t,x(t)) \leq -\alpha_3 \| x \|^{ab} \end{gathered} \tag{6}$$

where $t \geq 0$, $x \in D$, $\beta \in (0,1)$, α_1, α_2, α_3, a and b are arbitrary positive constants. Then, the origin is Mittag-Leffler stable. In the case that assumptions hold globally on $\mathbb{R}^n$, it could be deduced that the origin is globally Mittag-Leffler stable.

The common Asymptotic stability is implied by Mittag-Leffler stability.

Lemma 1: [29] Suppose that $x(t) \in \mathbb{R}$ is a derivable and continuous function. Hence, at each time instant $t \geq t_0$ it is deduced that:

$$\frac{1}{2}\left({}_{t_0}^{C}D_{t}^{q}x^2(t)\right) \leq x(t)\,{}_{t_0}^{C}D_{t}^{q}x(t) \qquad \forall q \in (0,1) \tag{7}$$

The main tool in the present study includes Caputo fractional order operators.

Fuzzy System

As the proposed method uses fuzzy systems as a general approximator, this section briefly discusses these relationships.

The fuzzy logic system is concisely illustrated in Fig. 1 [1]. The primary configuration of this system consists of a fuzzifier, a defuzzifier, and an engine for fuzzy inferences. This engine is made up of some IF-THEN rules to create a $U = [U_1 \times U_2 \times \ldots \times U_n]$ to $\mathbb{R}$ mapping, in which $X = [x_1, x_2, \ldots, x_n] \in \mathbb{R}^n$ denotes a linguistic input vector, and the output of the fuzzy logic system is denoted by the linguistic variable $y \in \mathbb{R}$ [1]. The l^{th} fuzzy rule is denoted by:

$$R^l\colon If\ x_1\ is\ F_1^l\ and\ x_n\ is\ F_n^l\ then\ y\ is\ B^l \tag{8}$$

where F_i^l and B^l are the labels of the input and output fuzzy sets, respectively. Suppose l to be the number of fuzzy IF-THEN rules and consider i as the number of inputs of the fuzzy logic system. The fuzzy system output value would equal the following equation by applying product inference, singleton fuzzification, and center average defuzzification:

$$y(x) = \frac{\sum_{l=1}^{M} y^l \prod_{i=1}^{n} \mu_{F_i^l}(x_i)}{\sum_{l=1}^{M} \prod_{i=1}^{n} \mu_{F_i^l}(x_i)} \tag{9}$$

where the membership function for the linguistic variable x_i is denoted by $\mu_{F_i^l}(x_i)$, and the crisp value y^l is the value of y corresponding to the maximum value of the Gaussian membership function μ_{B^l} [3]. Hence, Equation (9) can result in the following by applying the fuzzy basis function (FBF) [1]:

$y(x) = \theta^T \xi(x)$ (10)

where $\theta = [y^1, y^2, \ldots, y^M]^T$ is a parameter vector and $\xi(x) = [\xi^1(x), \xi^2(x), \ldots, \xi^M(x)]^T$ is the fuzzy basis functions set definable by:

$$\xi^l(x) = \frac{\prod_{i=1}^{n} \mu_{F_i^l}(x_i)}{\sum_{l=1}^{M} \prod_{i=1}^{n} \mu_{F_i^l}(x_i)}. \tag{11}$$

Equation (9) is regarded as a universal approximator in terms of a fuzzy system if its parameters are chosen properly [2].

Lemma 2: [32] Assume $f\colon \Omega \to R$ is Lipschitz continuous for each $x \in C^1(I;\Omega)$ and $\epsilon > 0$, there would be a fuzzy logic system of (10) in a way that $sup|f(x(t)) - \theta^T\xi(x)| \leqslant \epsilon$ holds.

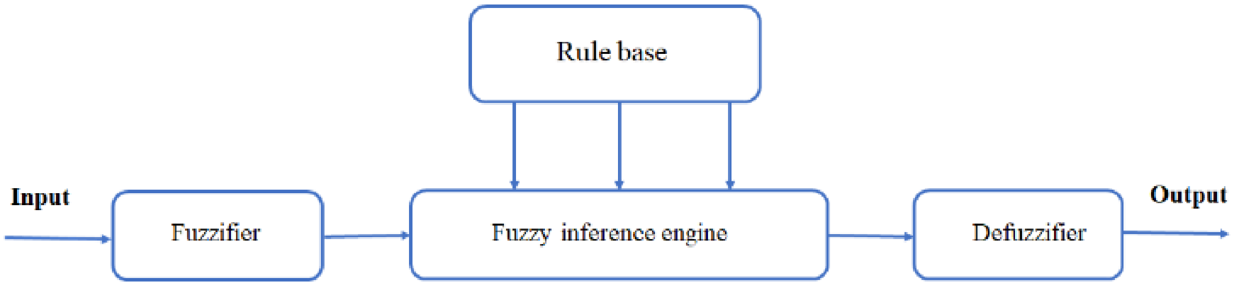

Fig. 1: Graph of the fuzzy logic system

Both Equation (11) and Lemma 2 are essential for understanding fuzzy systems as universal approximators.

III. PROBLEM STATEMENT

In the present study, the general form of the non-affine fractional-order system is considered below:

$$\begin{cases} D^q x_1 = x_2 \\ D^q x_2 = f(x,u) + \sigma(t) \\ y = x_1 \end{cases} \tag{12}$$

where $X = [x_1, x_2]^T$ is the state variable, $f(x,u)$ shows an unknown nonlinear function, $\sigma(t)$ is the bounded disturbance, and u presents the control input. The main control objective for the system in Equation (12) is to design a fuzzy adaptive fractional-order controller in a way that the system output $y(t)$ tracks a desired trajectory $y_d(t)$. In the meantime, all closed-loop system signals remain bounded. Concerning the system in Equation (12) and the desired trajectory, the next assumption should be considered.

Assumption 1: It is assumed that the nonzero function $f_u(x,u) = \frac{\partial f(x,u)}{\partial u}$ satisfies the following inequality, without loss of generality.

$$f_u(x,u) \geq F > 0 \tag{13}$$

in which F ∈ ℝ is constant and known.

Assumption 2: The nonzero function $f_u(x,u)$ is supposed to fulfil the next inequality.

$$D^q(\frac{1}{f_u}) = -\frac{D^q f_u}{f_u} \leq 0 \tag{14}$$

Assumption 3: The boundary of the external disturbance is regarded as:

$$|\sigma(t)| \leqslant D. \tag{15}$$

Assumption 4: An arbitrary trajectory $y_d(t)$ as well as all its fractional time derivatives $D^q y_d(t)$ are bounded and smooth.

The tracking error is defined as:

$$e = [e_1, e_2]^T \tag{16}$$

where $e_1 = y_d - y$. By q-order time differentiating of Equation (16), we obtain:

$$\begin{cases} D^q e_1 & = D^q y_d - D^q y = D^q y_d - D^q x_1 \\ & = D^q y_d - x_2 = e_2 \\ D^q e_2 & = D^{2q} y_d - D^q x_2 \\ & = D^{2q} y_d - f(x,u) - \sigma(t) \end{cases} \tag{17}$$

So, Equation (17) can be rewritten as Equation (18).

$$D^q e = A_1 e + B[(D^{2q} y_d - f(x,u) - \sigma(t)] \tag{18}$$

where $A_1 = \begin{bmatrix} 0 & 1 \\ 0 & 0 \end{bmatrix}$ and $B = [0 \quad 1]^T$.

Consider $A = A_1 - BK^T$ be Hurwitz, for $K = [k_1, k_2]^T$. Hence, according to the next equation, each symmetric positive definite matrix Q has a unique symmetric positive definite solution P such that [41]:

$$A^T P + PA = -Q \tag{19}$$

Let w be defined as

$$w = D^{2q} y_d + K^T e + \alpha tanh(\frac{B^T Pe}{\varepsilon}) + w' \tag{20}$$

ε denotes a small positive constant, α denotes a large positive constant, and $tanh(.)$ is the hyperbolic tangent function, and w' stands for the adaptive term that describes later. If the term $K^T e + \alpha tanh(\frac{B^T Pe}{\varepsilon}) + w'$ is added and subtracted to the right-hand side of Equation (18), it leads to:

$$D^q e = Ae - B[f(x,u) - w + \sigma(t) + \alpha tanh(\frac{B^T Pe}{\varepsilon}) + w'] \tag{21}$$

Using Assumption 1, the next inequality is true for the signal, which is not explicitly dependent on the control input u:

$$\frac{\partial(f(x,u) - w)}{\partial u} = \frac{\partial f(x,u)}{\partial u} > 0 \tag{22}$$

Based on the implicit function theorem, the nonlinear algebraic equation $f(x,u) - w = 0$ is locally solvable for an arbitrary input (x,u). Hence, for any $(x,w) \in R^2 \times R$, some ideal controller $u^*(x,w)$ exists such that fulfills the next equality:

$$f(x,u^*) - w = 0 \tag{23}$$

Using the mean value theorem, a constant $\mu \in (0,1)$ exists in a way that the nonlinear function $f(x,u)$ is expressed around u^* as:

$$f(x,u) = f(x,u^*) + (u - u^*) f_{u_\mu} = f(x,u^*) + e_{u_\mu} f_{u_\mu} \tag{24}$$

where

$$\begin{cases} f_{u_\mu} = \frac{\partial(f(x,u))}{\partial u}|_{u=u_\mu} \\ u_\mu = u\mu + (1-\mu)u^* \end{cases} \tag{25}$$

By replacing Equation (24) into the error Equation (21), we have:

$$D^q e = Ae - B[e_{u_\mu} f_{u_\mu} + \sigma(t) + \alpha tanh(\frac{B^T Pe}{\varepsilon}) + w'] \tag{26}$$

Nonetheless, the existence of the ideal controller $u^*(x,w)$ for the system (23) is just assured according to the implicit function theory, but no solution technique is recommended yet. The next section deals with obtaining the unknown ideal control.

IV. FRACTIONAL ORDER FUZZY ADAPTIVE CONTROLLER

The previous section discusses the existence of an ideal controller for control objectives. This section focuses on developing a fuzzy system for the adaptive approximation of the unknown ideal controller. The ideal controller u^* is denoted as below.

$$u^* = f(z) + \epsilon \tag{27}$$

where $f(z) = \theta^{*T}\xi(z)$; θ^* and $\xi(z)$ are parameters and fuzzy basis functions, respectively. ϵ denotes an approximation error that fulfills $|\epsilon| \leq \lambda$. Unknown parameter θ^* is calculated via the next optimization.

$$\theta^* = arg_\theta min[sup|\theta^T\xi(z) - f(z)|] \tag{28}$$

The approximation of θ^* is denoted by θ and u_{rob} is a robust controller used for compensating uncertainties, approximation error, interconnection term, and disturbance. The controller (27) is rewritten as:

$$u = \theta^T\xi(z) + u_{rob} \tag{29}$$

In which $\theta^T\xi(z)$ is the ideal controller approximation, and u_{rob} is defined below.

$$u_{rob} = \frac{|B^TPe|}{FB^TPe}(Fu_r + Fu_c + \widehat{w}'). \tag{30}$$

where u_c is a compensation for uncertainties and approximation errors, $\widehat{w}'$ estimates w, and u_r recompensates bounded external disturbances.

Using parameter error as $\hat{\theta} = \theta - \theta^*$, Equations (29) and (30), Equation (26) becomes:

$$D^qe = Ae - B[\hat{\theta}^T\xi(z) + u_{rob} - \epsilon)f_{u_\mu} + \sigma(t) + \alpha tanh(\frac{B^TPe}{\varepsilon}) + w'] \tag{31}$$

Consider the following update laws [20]:

$$\begin{cases} D^q\theta = \beta_1B^TPe\xi(z) \\ D^qu_r = \beta_2|B^TPe| \\ D^qu_c = \beta_3|B^TPe| \\ D^qw' = \beta_4|B^TPe| \end{cases} \tag{32}$$

where $\beta_i > 0$, $i = 1,\dots,4$, are constant values. The updating laws will be derived later from the Lyapunov theorem, based on Theorem 2.

The block diagram of the overall controller is shown in Fig. 2.

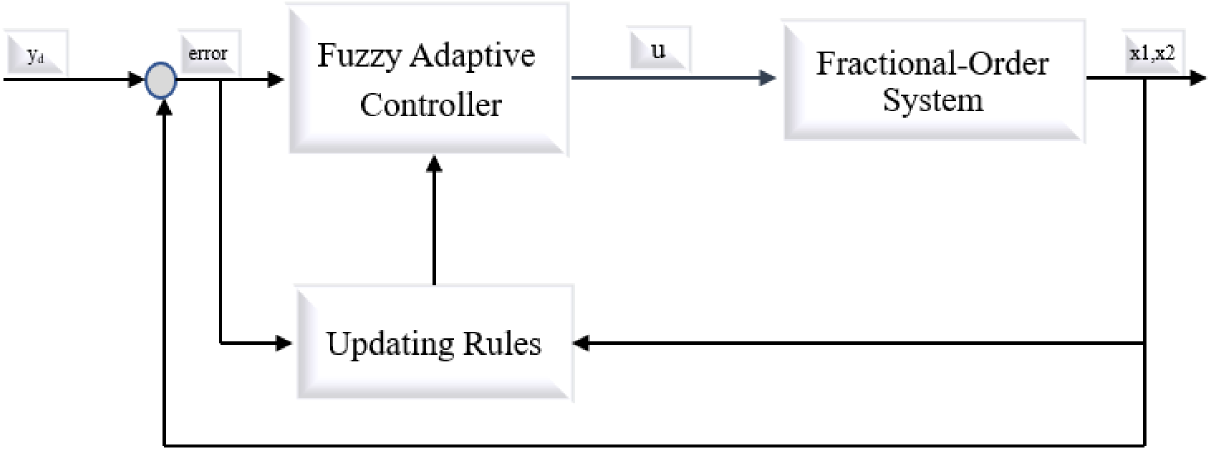

Fig. 2: The block diagram of the overall closed-loop system.

Theorem 2: Assume the error dynamical system of (31) and the external disturbances fulfilling Assumption 3. The controller structure described by Equations (29) and (30), along with the adaptation rules in Equation (32), ensures that the tracking error asymptotically converges to a neighborhood of zero and bounds all closed-loop system signals.

Proof: The following Lyapunov function is the starting point for proving the convergence of the tracking error, as well as the error of the parameters being bound to the neighborhood of the origin.

$$V = \frac{1}{2}[\frac{1}{f_u}e^TPe + \bar{\theta}^T\beta_1^{-1}\bar{\theta} + \frac{\bar{u}_r^2}{\beta_2} + \frac{\bar{u}_c^2}{\beta_3} + \frac{\bar{w}'^2}{\beta_4}] \tag{33}$$

where $\bar{\theta} = \theta - \theta^*$, $\bar{u}_r = u_r - \frac{D}{F}$, $\bar{u}_c = u_c - \epsilon$, and $\bar{w}' = w - w'$. According to Lemma 1, the q-order time derivative of the Lyapunov function becomes.

$$D^qV \leq \frac{1}{2}[\frac{1}{f_u}(e^TPD^qe + D^qe^TPe) + D^q(\frac{1}{f_u})e^TPe] + \bar{\theta}^T\beta_1^{-1}D^q\bar{\theta} + \frac{\bar{u}_rD^q\bar{u}_r}{\beta_2} + \frac{\bar{u}_cD^q\bar{u}_c}{\beta_3} + \frac{\bar{w}'D^q\bar{w}'}{\beta_4} \tag{34}$$

By substituting the error dynamics Equation (31) into Equation (34), we derive the following results:

$$D^qV \leq \frac{1}{2}[\frac{1}{f_u}e^T(A^TP + PA)e - (\frac{D^qf_u}{f_u})e^TPe] - \frac{1}{f_u}B^TPe[(\hat{\theta}^T\xi(z) + u_{rob} - \epsilon)f_{u_\mu} + \sigma(t) + \alpha tanh(\frac{B^TPe}{\varepsilon}) + w'] + \bar{\theta}^T\beta_1^{-1}D^q\bar{\theta} + \frac{\bar{u}_rD^q\bar{u}_r}{\beta_2} + \frac{\bar{u}_cD^q\bar{u}_c}{\beta_3} + \frac{\bar{w}'D^q\bar{w}'}{\beta_4} \tag{35}$$

Using the $B^TPe.tanh(\frac{B^TPe}{\varepsilon}) = |B^TPe|$ and Equation (19), Equation (35) can be rewritten as (36).

$$D^qV \leq \frac{1}{2}[-\frac{1}{f_u}e^TQe - \frac{D^qf_u}{f_u})e^TPe - \frac{\alpha}{f_u}|B^TPe|] + \frac{1}{f_u}B^TPe[(\hat{\theta}^T\xi(z) + u_{rob} - \epsilon)f_{u_\mu} + \sigma(t) + w' + \bar{\theta}^T\beta_1^{-1}D^q\bar{\theta} + \frac{\bar{u}_rD^q\bar{u}_r}{\beta_2} + \frac{\bar{u}_cD^q\bar{u}_c}{\beta_3} + \frac{\bar{w}\prime D^q\bar{w}\prime}{\beta_4} \tag{36}$$

Using Assumptions 1 and 3 and Equation (36), we have:

$$D^qV \leq \frac{1}{2}[-\frac{1}{f_u}e^TQe - \frac{D^qf_u}{f_u})e^TPe - \frac{\alpha}{f_u}|B^TPe|] + \frac{|B^TPe|}{F}|w'| - B^TPe\hat{\theta}^T\xi(z) - |B^TPe|u_{rob} + |B^TPe|\epsilon - \frac{|B^TPe|}{F}w' + \frac{|B^TPe|}{F}D + \bar{\theta}^T\beta_1^{-1}D^q\bar{\theta} + \frac{\bar{u}_rD^q\bar{u}_r}{\beta_2} + \frac{\bar{u}_cD^q\bar{u}_c}{\beta_3} + \frac{\bar{w}\prime D^q\bar{w}\prime}{\beta_4} \tag{37}$$

After performing several mathematical manipulations, the following equation is established.

$$D^qV \leq \frac{1}{2}[-\frac{1}{f_u}e^TQe - \frac{D^qf_u}{f_u})e^TPe - \frac{\alpha}{f_u}|B^TPe|] - B^TPe\hat{\theta}^T\xi(z) + \bar{\theta}^T\beta_1^{-1}D^q\bar{\theta} - |B^TPe|u_r + \frac{|B^TPe|}{F}D + \frac{\bar{u}_rD^q\bar{u}_r}{\beta_2} - |B^TPe|u_c + |B^TPe|\epsilon + \frac{\bar{u}_cD^q\bar{u}_c}{\beta_3} + \frac{|B^TPe|}{F}|w'| - \frac{|B^TPe|}{F}\hat{w} + \frac{\bar{w}\prime D^q\bar{w}\prime}{\beta_4} \tag{38}$$

By substituting the adaptive law described in Equation (32), the above inequality can be rewritten as follows:

$$D^qV \leq -\frac{1}{2}[\frac{1}{f_u}e^TQe + \frac{D^qf_u}{f_u}e^TPe + \frac{\alpha}{f_u}|B^TPe|] \tag{39}$$

Based on the proposed assumptions, $D^qV \leq 0$ is satisfied. Then, the origin is Mittag-Leffler stable and consequently, the equilibrium point of the system is asymptotically stable. Thus, according to Theorem 1, the tracking error converges to the neighborhood of the origin. Furthermore, all the signals involved in the closed-loop system are bounded. Thus, the proof is finalized.

V. SIMULATION RESULTS

In this section, a FO fuzzy adaptive controller is proposed, and three nonlinear FO examples are presented to validate the methodology's influence. In all cases mentioned below, the Caputo approach applies to the derivative operator.

Case A: *Chaotic System*

Consider the duffing dynamics discussed in the following FO nonlinear equations.

$$\begin{cases} D^qx_1 = x_2 \\ D^qx_2 = (1 + \mu sin(\omega t))x_1 - rx_2 - x_1^3 + u \\ \end{cases} \tag{40}$$

where $\omega = 1$, $r = 0.2$, and $\mu = 1$. Five membership functions are defined for every input, and seven membership functions are considered for each output with 25 "If-Then" rules. Fig. s 3 and 4 show the phase portrait of the fractional-order duffing system.

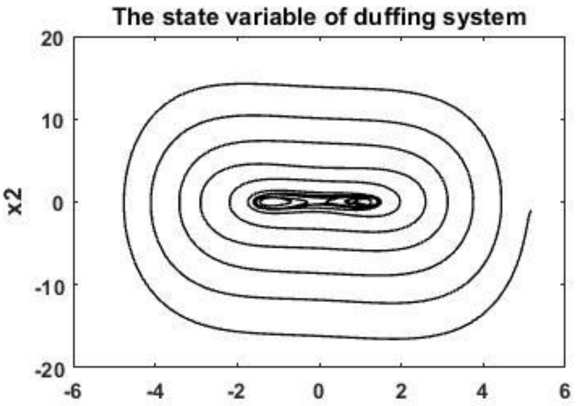

Fig. 3: The state variable of the duffing system with $[x_1(0), x_2(0)] = [5, -1]$.

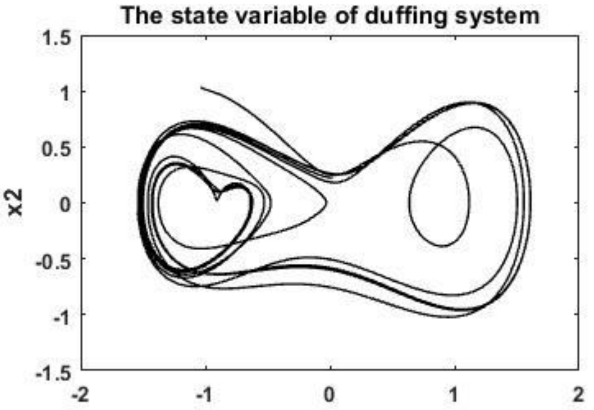

Fig. 4: The state variable of duffing system with $[x_1(0), x_2(0)] = [-1,1]$.

As it is obvious in Fig.s (3) and (4), the duffing chaotic system is sensitive to the initial values.

To reduce the sensitivity of the chaotic system to initial conditions and perform output tracking, we apply the planned controller, Equations (29) and (30), to the fractional-order Duffing system.

Fig. 5 presents the system's output and the desired trajectory under the planned controller.

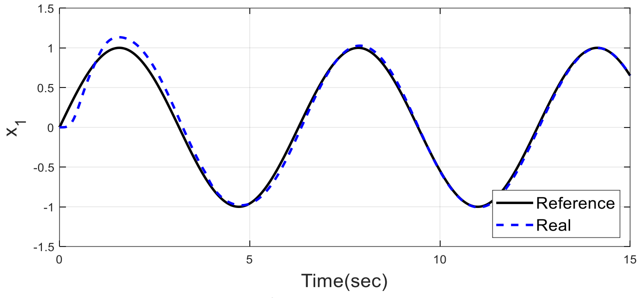

Fig. 5: Tracking trajectory of Case A

Fig. 6 depicts the tracking error as the difference between the system's output and its desired value.

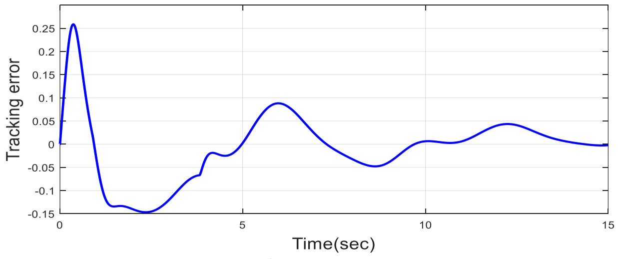

Fig. 6: Output Tracking error for case A

As shown in Fig. s 5 and 6, the performance of the proposed controller in the presence of external disturbances is satisfactory and furthermore denotes the convergence of tracking errors to zero in a considerably short time.

The control input of the system is depicted in Fig. 7.

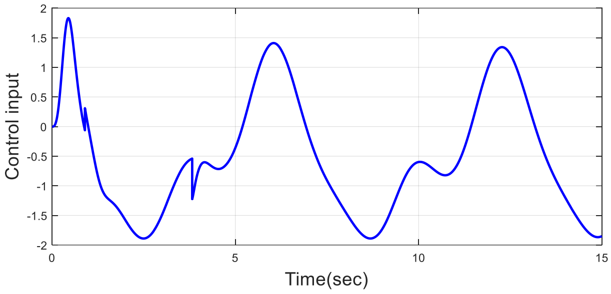

Figure 7: Control input for the FO Duffing system

As can be seen from Fig. s 5-7, it is evident that the proposed controller exhibits favorable performance. Furthermore, all signals involved in the closed-loop system are bounded in the above figures as proved by Theorem 2.

For comparing our approach with other methods, we apply a PID controller to the duffing system mentioned in Equation (40). The coefficients of the controller are tuned based on Ziegler-Nichols as $k_p = 2000, k_I = 100, k_D = 10$.

The reference signal and the system's output under the PID controller are depicted in Fig. 8.

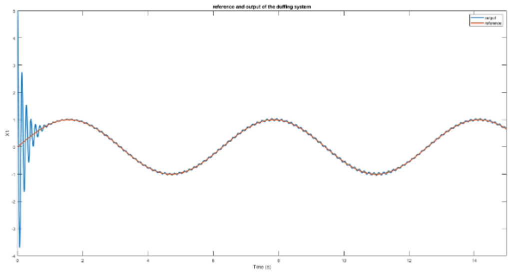

Fig. 8: Outputs of the system and reference signal under the PID controller.

The difference between the reference signal and the system's output is shown in Fig. 9.

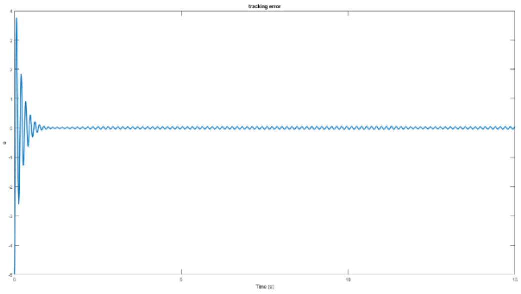

Fig. 9: Tracking error under the PID controller.

The control input of the system is illustrated in Fig. 10.

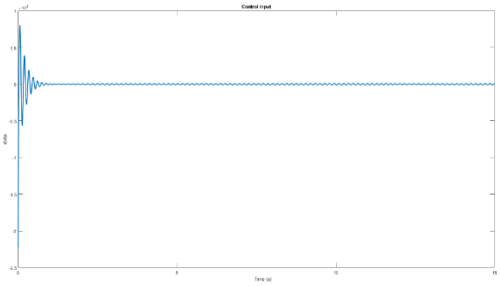

Fig. 10: Control input for the FO Duffing system under the PID controller

As shown in the above figures, it is clear that our approach outperforms the PID controller. However, the PID controller exhibits a faster convergence speed compared to our method. Moreover, the PID controller cannot eliminate the disturbances perfectly.

Case B: *Fractional order nonlinear Gyroscope*

To investigate the proposed methodology, we apply it to a fractional-order nonlinear gyroscope system. Thus, the fractional-order nonlinear nonaffine model of the gyroscope is:

$$D_t^q x_{1=} x_2$$

$$D_t^q x_2 = -100 \frac{\left(1-\cos\left(x_1^2(t)\right)\right)^2}{sin^3\left(x_1(t)\right)} - 0.5x_2(t) - 0.05x_2^3(t) + 35.5sin(25t)\, sin(x_1(t)) + sin(x_1(t)) + \Delta_f(x,t) + d(t) + u(t) \qquad (41)$$

where q stands for Caputo fractional order, x_1 is the rotation angle of a gyroscope, and x_2 shows the angular rotation speed. In our approach, the uncertainties and external disturbances are considered as [25]:

$$\begin{cases} \Delta_f = 4sin(x_1) + cos(x_2) \\ d(t) = 2cos(2t) \end{cases} \qquad (42)$$

Fig. 11 depicts the fractional-order nonlinear structure of the gyroscope [25].

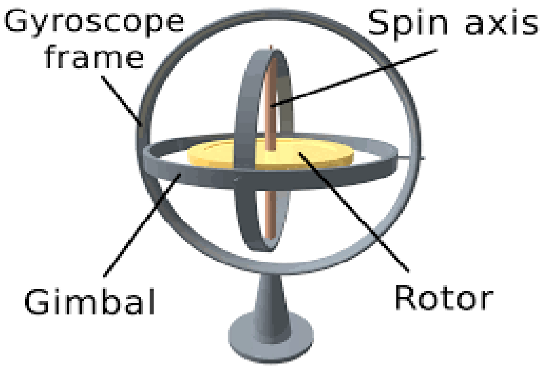

Fig. 11: Gyroscoper scheme [25]

In this case, five membership functions have been considered for input and seven for output. 25 “If-Then” rules are assigned for the fuzzy system.

Fig. 12 shows both the first state of the nonlinear fractional-order gyroscope controlled by a fuzzy adaptive controller, along with the reference signal.

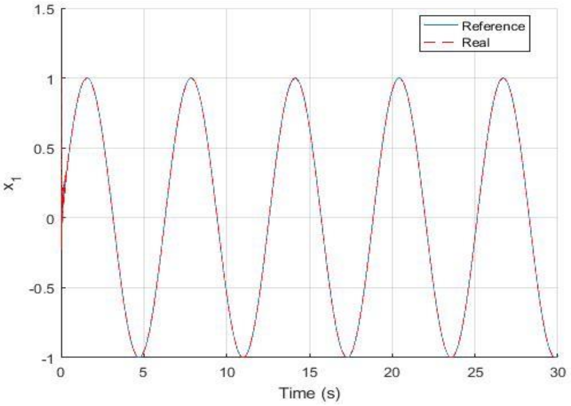

Fig.12: Tracking trajectory of gyroscoper system

The tracking error (difference between the first state of the nonlinear fractional-order gyroscope and the reference signal) is illustrated in Fig. 13.

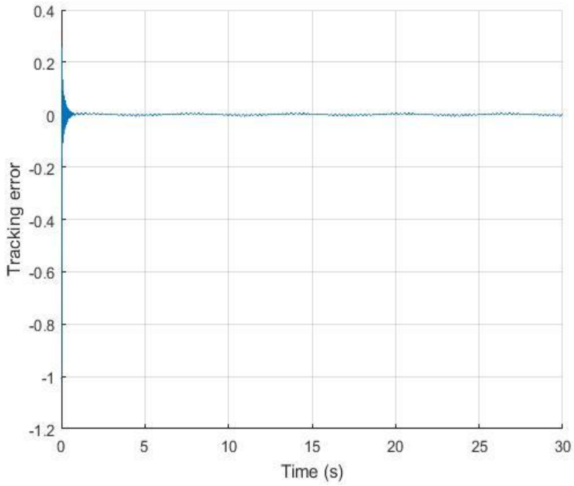

Fig.13: Tracking error of gyroscoper system.

As shown in Fig. s 12 and 13, the convergence of the tracking error to zero is guaranteed.

The control input of the gyroscope system (41) is demonstrated in Fig. 14.

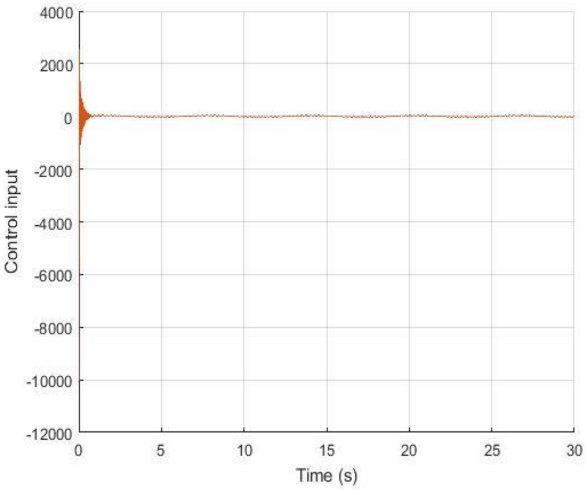

Fig. 14: Control signal of the gyroscoper system.

Based on Theorem 2 and Fig. 14, the control input is bounded. Fig. s 12- 14 show both the tracking error convergence to the origin and the boundedness of the signals of the closed-loop system, indicating that the proposed methodology has promising performance in the presence of external disturbances and uncertainties.

Case C: *Nonlinear inverted pendulum*

The planned policy is applied on a fractional-order nonlinear nonaffine inverted pendulum model, which is expressed below [33]:

$$aD_t^q x_{1=}x_2$$

$$aD_t^q x_2 = \frac{gsin(x_1) - mlx_2^2\cos(x_1) + \frac{\sin(x_1)}{m_c+m}}{\frac{\frac{4}{3lmcos2(x_1)}}{m_c+m}} + \frac{\frac{\cos(x_1)}{m_c+m}}{l\left[\frac{\frac{4}{3mcos2(x_1)}}{m_c+m}\right]}u + d(t) \qquad (43)$$

where x_1 and x_2 respectively indicate the swing angle and swing speed, d(t) as the external disturbance. This approach considers five membership functions for input and seven for output. 25 "If-Then" rules are designated for fuzzy systems. Fig. 15 shows the inverted pendulum scheme [33].

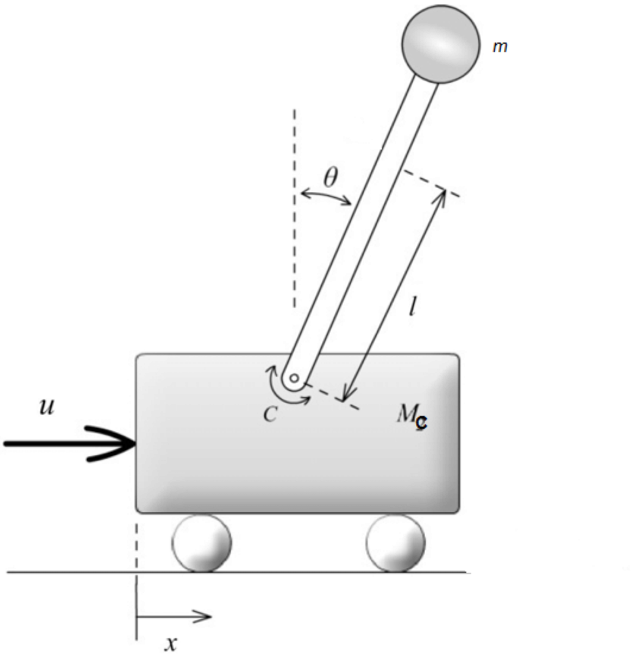

Fig. 15: Fractional order nonlinear Inverted Pendulum [33]

Table I summarizes the inverted pendulum parameters.

TABALE I

The Parameters of the Fractional-order Nonlinear Inverted Pendulum.

Symbols	Value	Unit
$\bar{g}$	gravitational acceleration	9.8 m/s^2
m_c	mass of the cart	1 Kg
m	mass of the pendulum	0.1 Kg
l	length to pendulum center of mass	0.5 m

The objective of control denotes the design of a fixed-time law in a way that the inverted pendulum motion tracks the assumed bounded reference trajectory as $r(t)$.

Both the tracking trajectory of the inverted pendulum using fuzzy adaptive methodology and the reference signal are shown in Fig. 16.

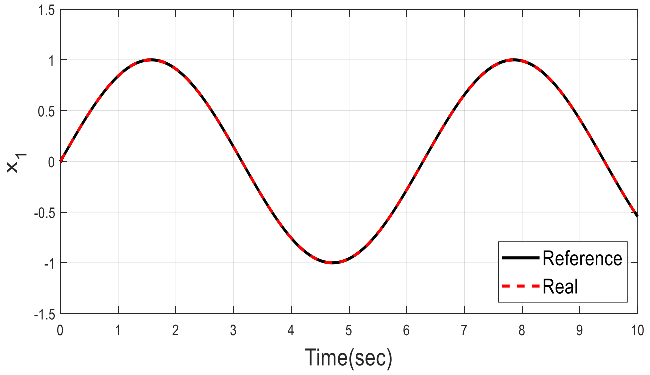

Fig.16: Tracking trajectory of the inverted pendulum.

The difference between the first state of (43) and the reference signal is presented in Fig. 17.

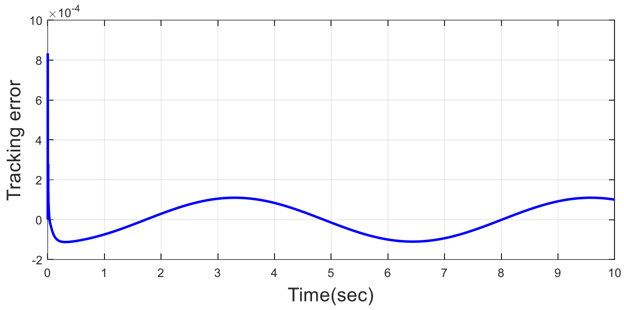

Fig. 17: Tracking error of the inverted pendulum

Fig. s 16 and 17 demonstrate that the system's output converges to the reference signal. Furthermore, the presence of uncertainties and disturbances can not affect the performance of the system. The control input is established in Fig. 18.

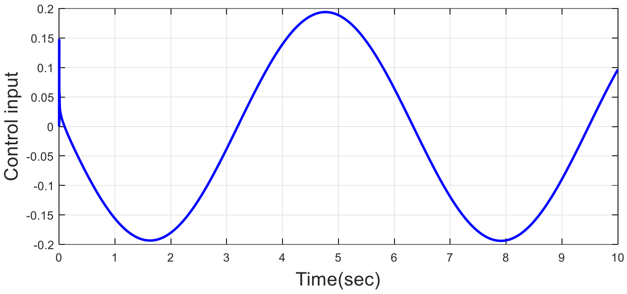

Fig. 18: Control input of the inverted pendulum

Fig. s 16 through 18 confirm the encouraging performance of the planned procedure.

This section clearly indicates that:

1- Convergence of the tracking error to zero is guaranteed.
2- Robustness against uncertainties and disturbances is guaranteed.
3- Boundedness of the signal involved in the closed-loop system is assured.

VI. CONCLUSION

This paper discusses a fuzzy adaptive output tracking methodology for fractional-order (FO) nonaffine nonlinear systems. Fuzzy logic is employed as a universal approximator, leveraging expert knowledge in the controller design process. The adaptation laws proposed in this study ensure both closed-loop stability, in accordance with Lyapunov's stability criteria, and the asymptotic convergence of the tracking error to a neighborhood around the origin. The main advantages of this methodology are: 1) the incorporation of expert knowledge in the controller design, and 2) robustness against disturbances, approximation errors, and model uncertainties. To demonstrate the effectiveness and performance of the proposed approach, it has been applied to three types of FO nonaffine nonlinear systems. Simulation results indicate that the method achieves an acceptable tracking error and a rapid response time. The main limitations of the proposed method are 1) applying Assumption 2 on the unknown function of the systems and 2) the complex controller structure in Section 3. The complexity of the proposed controller in sections 3 through 5 is due to both the structure and the unknown function of the system. In future work, we plan to explore the application of this methodology to real-world FO nonaffine nonlinear systems with input constraints.

ACKNOWLEDGMENTS

The authors gratefully acknowledge the support for this work that was provided by the University of Qom.

FUNDING

The author declares that there is no conflict of interest regarding the publication of this article.

AUTHORS' CONTRIBUTIONS

Conceptualization and study design: Reza Ghasemi, Bita Sadat Ghazanfarpour, Mahmood Mahmoodi.

Data collection and experimentation: Bita Sadat Ghazanfarpour, Farideh Shahbazi.

Data analysis and interpretation: Bita Sadat Ghazanfarpour, Farideh Shahbazi.

Manuscript writing and editing: Bita Sadat Ghazanfarpour, Farideh Shahbazi, Reza Ghasemi.

Supervision and project administration: Reza Ghasemi.

CONFLICTS OF INTEREST/COMPETING INTERESTS

The authors declare that they have no conflict of interest.

STATEMENT ON THE USE OF GENERATIVE AI

AI cannot be listed as an author. Only human authors take responsibility.

REFERENCES

[1] LX. Wang, "A Course in Fuzzy Systems and Control", Prentice Hall PTR, 1997.
[2] LX. Wang, JM. Mendel, "Fuzzy basis function, universal approximation, and orthogonal least square learning", IEEE Trans Neural Network 3(5), 807–814, 1993.
[3] HJ. Zimmermann, "Fuzzy Set Theory and Its Application, Kluwer Academic Publishers, 1996.
[4] B. Vinagre and V. Feliu, " Modeling and control of dynamic systems using fractional calculus: Application to electrochemical processes and flexible structures", in Proc. 41st IEEE Decision and Control Conference, 214-239, 2002.
[5] R. L. Magin, "Fractional calculus in bioengineering", Begell House, Redding, publisher, 2006.
[6] J. Sabatier, M. Aoun, A. Oustaloup, G. Grégoire, F. Ragot, and P. Roy, "Fractional system identification for lead acid battery state of charge estimation", Signal processing, vol. 86, pp. 2645- 2657, 2006.
[7] R. Hilfer, "Applications of fractional calculus in physics", World Scientific publisher, 2000.
[8] C. A. Monje, Y. Chen, B. M. Vinagre, D. Xue, and V. Feliu-Batlle, "Fractional-order systems and controls: fundamentals and applications", Springer Science & Business Media publisher, 2010.
[9] A. Oustaloup, X. Moreau, and M. Nouillant, "The CRONE suspension," Control Engineering Practice 4(1), 1101-1108, 1996.
[10] M. Zamani, M. Karimi-Ghartemani, N. Sadati, and M. Parniani, "Design of a fractional order PID controller for an AVR using particle swarm optimization," Control Engineering Practice 17(1), 1380-1387, 2009.
[11] N. Aguila-Camacho and M. A. Duarte-Mermoud, "Fractional adaptive control for an automatic voltage regulator," ISA transactions 52(1), 807-815, 2013.
[12] Y. He and R. Gong, "Application of fractional-order model reference adaptive control on industry boiler burning system," in 2010 International Conference on Intelligent Computation, Changsha, China, 2010.
[13] L. Jun-Guo, "Chaotic dynamics and synchronization of fractional-order Genesio–Tesi systems," Chinese Physics 14(8), 1517, 2005
[14] C. Li and G. Chen, "Chaos and hyperchaos in the fractional-order Rössler equations," Physica A: Statistical Mechanics and its Applications 31(3), 55-61, 2004.
[15] J. G. Lu, "Chaotic dynamics of the fractional-order Lü system and its synchronization," Physics Letters A 354(1), 305-311, 2006.

[16] Q. Yang and C. Zeng, "Chaos in fractional conjugate Lorenz system and its scaling attractors," Communications in Nonlinear Science and Numerical Simulation 15(2), 4041-4051, 2010.

[17] MR. Rahimi Khoygani, R. Ghasemi, "Neural estimation using a stable discrete-time MLP observer for a class of discrete-time uncertain nonlinear systems", Nonlinear Dynamics 84(4), 2517-2533, 2016.

[18] MR. Rahimi Khoygani, R. Ghasemi, A.R. Vali, "Intelligent nonlinear observer design for a class of nonlinear discrete-time flexible joint robot", Intelligent Service Robotics 8(1), 45–56, 2015.

[19] A. Sharafian, R. Ghasemi, "A novel terminal sliding mode observer with RBF neural network for a class of nonlinear systems", International Journal of Systems, Control and Communications 9(4), 369-385, 2019.

[20] F. Shahbazi, R. Ghasemi, M. Mahmoodi, "Fractional Nonsingular Terminal Sliding Mode Controller Design for the Special Class of Nonlinear Fractional-order Chaotic Systems", International Journal of Smart Electrical Engineering 11(2), 83-88, 2021.

[21] M. Ö. Efe, "Fractional fuzzy adaptive sliding mode control of a 2-DOF direct-drive robot arm", Systems, IEEE Transactions on Man and Cybernetics Part B: Cybernetics 38(1), 1561-1570, 2008.

[22] T.-C. Lin, T.-Y. Lee, and V. E. Balas, "Adaptive fuzzy sliding mode control for synchronization of uncertain fractional order chaotic systems," Chaos, Solitons & Fractals 44(2), 791-801, 2011.

[23] T.-C. Lin, C.-H. Kuo, T.-Y. Lee, and V. E. Balas, "Adaptive fuzzy H∞ tracking design of SISO uncertain nonlinear fractional order time-delay systems," Nonlinear Dynamics 69(3), 1639- 1650, 2012.

[24] T.-C. Lin and T.Y. Lee, "Chaos synchronization of uncertain fractional-order chaotic systems with time delay based on adaptive fuzzy sliding mode control," IEEE Transactions on Fuzzy Systems 19(2), 623-635, 2011.

[25] M. P. Aghababa, Comments on "Adaptive fuzzy H∞ tracking design of SISO uncertain nonlinear fractional order time-delay systems", [Nonlinear Dyn. 69 (2012) 1639–1650]. *Nonlinear Dynamics*, *70*(4), 2511-2513, 2012.

[26] S. Tong, H.-X. Li, and W. Wei, "Comments on Direct adaptive fuzzy-neural control with state observer and supervisory controller for unknown nonlinear dynamical systems", IEEE Transactions on Fuzzy Systems 11(2), 703-705, 2003.

[27] T.-C. Lin, C.-H. Kuo, and V. E. Balas, "Uncertain fractional order chaotic systems tracking design via adaptive hybrid fuzzy sliding mode control," International Journal of Computers Communications & Control 6(2), 418-427, 2011.

[28] Y. Li, YQ. Chen, I. Podlubny, "Mittag–Leffler stability of fractional-order non-linear dynamic systems", Automatica 45(8), 1965-1969, 2009.

[29] N. Aguila-Camacho, M. Duarte-Mermoud, J. Gallegos, "Lyapunov Functions for Fractional Order Systems", Communications in Nonlinear Science and Numerical Simulation 19(9), 2951-2957, 2014.

[30] P. Jafari, M. Teshnehlab, and M. Tavakoli-Kakhki, "Adaptive Type-2 Fuzzy System for Synchronization and Stabilization of Chaotic Nonlinear Fractional Order Systems," IET Control Theory & Applications 12(3), 183-193, 2017.

[31] P. Jafari, M. Teshnehlab, and M. Tavakoli-Kakhki, "Synchronization and stabilization of fractional order nonlinear systems with adaptive fuzzy controller and compensation signal," Nonlinear Dynamics 90, 1037-1052, 2017.

[32] L.X. Wang, "Adaptive Fuzzy Systems and Control: Design and Stability Analysis", Prentice-Hall, Inc., 1994.

[33] A. Kumar, V. Kumar, "An interval type-2 fractional order fuzzy logic controller employed to an uncertain nonlinear inverted pendulum", 14th IEEE India Council International Conference, 2017.

[34] L. Chen, J. Fang, "Adaptive continuous sliding mode control for fractional order systems with uncertainties and unknown control gain", Automation and Systems 20, 1509- 1520, 2022.

[35] N. Ullah, S. Han, MI. Khattak, "Adaptive fuzzy fractional order sliding mode controller for a class of dynamical systems with uncertainty", Transactions of the Institute of Measurement and Control 38, 402- 413, 2016.

[36] S. Mirzajani, MP. Aghababa, A. Heydari, "Adaptive T- S fuzzy control design for fractional order systems with parametric uncertainty and input constraint", Fuzzy Sets and Systems 365, 22- 39, 2019.

[37] X. Qin, S. Liu, "Adaptive fuzzy synchronization of uncertain fractional order chaotic systems with different structures and time delays", Advances in Difference Equations 174, 2019.

[38] X. Hu, Q. Song, M. Ge, R. Li, "Fractional order adaptive fault tolerant control for a class of general nonlinear systems", Nonlinear Dynamics 101, 379- 392, 2020.

[39] YX. Li, QY. Wang, S. Tong, "Fuzzy adaptive fault tolerant control of fractional order nonlinear systems", IEEE Transactions on Systems, Man, and Cybernetics: Systems 51, 1372- 1379, 2021.

[40] A. Mohammadzadeh, O. Kaynak, "A novel fractional order fuzzy control method based on immersion and invariance approach", Applied Soft Computing 88, 2020.

[41] O. Mofid, S. Mobayen, "Adaptive synchronization of fractional order quadratic chaotic flows with nonhyperbolic equilibrium", Journal of vibration and control 24, 2018.

[42] A. Sharafian, A. Ali, I. Ullah, T.R. Khalifa, X. Bai, L. Qiu, "Fuzzy adaptive control for consensus tracking in multiagent systems with incommensurate fractional-order dynamics: Application to power systems", Information Sciences 689(1): 121455, 2025.

[43] M.A.Z. Tajrishi, A. Akbarzadeh Kalat, "Fast finite time fractional-order robust-adaptive sliding mode control of nonlinear systems with unknown dynamics", Journal of Computational and Applied Mathematics 438: 115554, 2024.

Semnan University

Journal of Modeling & Simulation in Electrical & Electronics Engineering (MSEEE)

Journal homepage: **https://mseee.semnan.ac.ir/**

ISSN: 2821-0786

A Bi-Level Model for Optimal Placement and Sizing of EV Fast Charging Stations Considering Traffic and Power Network Interactions

Mohammad Alizadeh[1*] and Ali Godarzi Amlashi[2]

***Abstract*— This paper presents a bi-level optimization model for the siting and sizing of electric vehicle fast charging stations (FCSs), considering the constraints of the power distribution network. In the presented method, queuing theory and a user equilibrium-based traffic assignment model are used to determine the size of FCSs. The upper-level problem aims to maximize the profit of the FCS owner by determining optimal locations and capacities of FCSs. The lower-level problem minimizes the operational cost of the distribution network while considering power flow constraints and EV charging demands. The bi-level model is transformed into a single-level mathematical program using the Karush-Kuhn-Tucker (KKT) primal-dual optimality conditions of the lower-level problem due to the linearity of the LL problem. Simulation results on the IEEE 33-bus distribution system and a 25-node transportation network show that two FCSs are optimally installed at buses 25 and 32 with 9 and 7 chargers, respectively, yielding a daily profit of approximately $6,147 for the investor. Sensitivity analysis demonstrates that higher electricity selling prices lead to increased profitability and expansion of charging infrastructure, highlighting the effectiveness of the proposed framework in capturing the economic interaction between the DSO and private investors.**

Keywords: Bi-level Optimization, Karush-Kuhn-Tucker, Queuing Theory, Sizing of Electric Vehicle Charging Stations, Locational Marginal Prices

NOMENCLATURE

Sets and indices

r	Travel origin index
u	Travel destination index
k	The path index for moving from origin r to destination u

Parameters

fr_a	Traffic load of the road a
t_{a0}	Travel time on the road without traffic
a_K^F	Fixed cost in bus k
a_K^{LS}	Cost dependent on location and size of charging station on bus k
a^{CHF}	Cost of equipment required to build an FCS
C	Overall daily charging demand (times/day).
σ	percentage of EVs that are recharged at home by using standard wall outlets (%)
β	Choosing the ratio of charging posts

Received; 2025-10-27 Revised; 2025-12-16 Accepted; 2025-12-28

1. Faculty of Electrical and Computer Engineering, Imam Khomeini Naval University, Nowshahr, Iran
2. Faculty of Electrical and Computer Engineering, Imam Khomeini Naval University, Nowshahr, Iran
*Corresponding author: golmahalleh63@gmail.com

Cite this article as:
Alizadeh, A. and Godarzi Amlashi, A. (2025). A Bi-Level Model for Optimal Placement and Sizing of EV Fast Charging Stations Considering Traffic and Power Network Interactions. *Journal of Modeling & Simulation in Electrical & Electronics Engineering (MSEEE)*. Semnan University Press . 5 (4), 35-44.
DOI: https://doi.org/10.22075/MSEEE.2025.39439.1232

f_t^{trip}	Trip ratio in time t
$f_{k,t}$	Traffic flow captured by the kth FCS
μ	Mean service rate of FCS (vehicles/hour)
q_{ru}	Total traffic load between source r and destination u
ε	Interest rate
n_{FCS}	capital recovery factor
p^{FCS}	Nominal charging power of the fast charging facility.

variables

$fp_{r,u,k}$	Traffic load of the kth path between origin r and destination u
t_a	Travel time on the road a (hour)
$Fn_{k,t}$	The total traffic load of the arcs ending at node k
$\delta_{r,u,k,a}$	Binary variable indicating the existence of arc a on the kth path for moving from origin r to destination u
$\rho_{k,t}$	Occupation rate of fast charging facilities of the kth FCS in time t (%)
ρ_k^{RH}	Occupation rate of fast charging facilities of the kth FCS in the rush hour (%)
Z_k	Number of charges at the kth station
λ_k^{RH}	The number of vehicles entering the candidate charging station during peak hours (vehicles)
W_k^{RH}	Average waiting time for the charging service in the th FCS during the rush hour (hour)
$P_{k,t}^{FCS}$	Charging power of the kth FCS in time t (kW)
z_k	Size of the kth FCS
R^{FCS}	The revenue of the FCS investor ($)
$Cost^{FCS}$	The cost of the FCS investor ($)
C^{inv}	The investment cost of FCS ($)
U_i	Binary variable representing the establishment of an FCS at bus i
$Cost_{i,t}^{up}$	The cost of buying energy from the upstream network for the FCS investor ($)
$P_{g,t}$	Active power generation of generator g in time t (kW)
$P_{i,t}^{grid}$	Active power purchased from the electrical grid at bus i, in time t (kW)
$P_{i,t}^{LS}$	The amount of load shedding at bus i (kW)
$P_{l,t}^{flow}$	Active power flow through line l at time t (kW)
$\theta_{i,t}$	Voltage angle at bus i, in time t

Acronyms

DSO	distribution system operator
EV	Electric Vehicles
FCS	Fast-charging stations
KKT	Karush-Kuhn-Tucker
LL	Lower level
OPF	Optimal Power Flow
OD	Origin Destination
PSO	Particle Swarm Optimization
UL	Upper Level

I. INTRODUCTION:

The growing adoption of Electric Vehicles (EVs) highlights the urgent need to expand fast-charging infrastructure. Fast-charging stations (FCS) significantly reduce charging time, enhance travel convenience, and promote EV acceptance. However, their deployment requires careful planning due to high investment costs and grid capacity limits. Strategic integration of fast-charging stations within transportation and power networks ensures efficient energy delivery and supports the transition toward sustainable, low-emission transportation.

Recent studies have proposed various optimization approaches to address the complex problem of locating and sizing FCSs for electric vehicles. A bi-level optimization model is proposed in [1] to determine optimal fast-charging station locations in a metropolitan network, minimizing travel time and infrastructure costs while considering vehicle types and traffic congestion. Reference [2] uses a genetic algorithm to identify profit-maximizing locations and designs for fast EV charging stations, considering stochastic charging demand, user-equilibrium traffic, and the interdependence between congestion, station queues, and price-sensitive charging behavior. Reference [3] develops an optimization strategy for allocating FCSs for electric vehicles. The proposed mixed-integer programming model minimizes investment and operating costs while considering PV-integrated carports and battery energy storage systems as alternative planning options.

When the distribution system operator (DSO) owns and operates the FCSs, the planning problem becomes integrated, combining investment and operational decisions under network constraints. Reference [4] presents a multi-objective model to determine the optimal placement and sizing of FCSs along intra-city corridors, integrating transportation and electrical networks. Reference [5] addresses the optimization of FCS size and location, taking into account investment, operation, and maintenance costs, power system losses, and reliability costs. A Particle Swarm Optimization approach is employed to identify the optimal station sizes and locations. In [6], a strategic framework for ultra-fast EV charging station planning is proposed, optimizing locations and charger numbers using the Voltage Stability Index and Harris Hawk Optimization to minimize total costs. The model also accounts for uncertainties in charging behavior and electricity prices via the 2m-Point Estimate Method. In [7], an optimal allocation and sizing method for EV charging stations in the Allahabad distribution network is proposed. The approach minimizes installation costs while enhancing grid performance based on voltage profile and real and reactive power loss indices. The nonlinear mixed-integer problem is solved using an improved metaheuristic algorithm, the Balanced Mayfly Algorithm. In [8], a multi-objective optimization approach is presented for the optimal placement of FCSs, DGs, and shunt capacitors. A Pareto-based hybrid method combining Grey Wolf Optimizer and Particle Swarm Optimization is employed to minimize multiple objectives in a 118-bus radial distribution system.

Several studies have formulated the siting and sizing of FCSs as bi-level optimization problems to capture the interaction between DSO, FCS investors, and EV users. In [9], a bi-level multi-objective model is developed for EV charging station location planning, simultaneously considering user preferences and waiting times. The upper level optimizes station locations and capacities to minimize total cost and service delay, while the lower level allocates users to stations to minimize travel time. In [10], a bi-level optimization model for fast charging station allocation is proposed. The upper layer maximizes investor profits, while the lower layer coordinates the expected efficiency of the charging service supply. In [11], an online vehicle-charging assignment model is integrated into the fast-charging station location problem for dynamic ridesharing with electric vehicles. The bi-level optimization aims to minimize the fleet’s total daily charging time. In [12], a bi-level optimization model is developed for the location and sizing of EV charging stations by jointly considering transportation and energy demands. The lower level incorporates user equilibrium traffic conditions as constraints, while the upper level optimizes the location, capacity, and pricing of new stations alongside existing ones. In [13], a bi-level programming model is proposed to determine the optimal locations of EV charging stations, aiming to minimize drivers’ range anxiety. In [14], a strategic charging-behavior-aware model is formulated as a bi-level mixed-integer program. The lower level models drivers’ charging responses using a network equilibrium approach, while the upper level optimizes charging station location and sizing to minimize overall traffic time and investment costs. In [15], a bi-level optimization model addresses the strategic location and sizing of EV charging stations under stochastic vehicle flows and charging times. The upper level minimizes infrastructure costs while ensuring probabilistic service requirements on users’ waiting times, considering route choice responses. In [16], a bi-level planning model for EV charging stations is proposed, incorporating traffic conditions and energy consumption per unit distance. The lower level represents users’ charging decisions, while the upper level optimizes station location and capacity. The model is solved using the Improved Whale Optimization Algorithm and Voronoi diagrams. In [17], a bi-level optimization model considers the impact of non-system-optimal driver behavior on EV charging station capacity. The upper level addresses the provider’s station location decisions, while the lower level models drivers’ selfish charging choices to minimize stops. Reference [18] proposes a bi-level model where the lower level minimizes daily operating costs through bus scheduling and charging optimization, while the upper level designs charging stations using a tabu search algorithm

Several other studies have focused on bi-level optimization models that primarily consider the transportation network perspective, emphasizing traffic flow, user behavior, and route planning in EV charging station deployment. In [19], a bi-level optimization approach using Particle Swarm Optimization is proposed to determine optimal EV charging station locations while minimizing losses and operating costs. An integrated EV charging planning algorithm manages connections to avoid peak load issues and severe voltage drops. In [20], a MILP-based coordinated planning method is proposed for coupled power and transportation networks, optimizing new road deployment, EV charging station placement along these roads, and power network expansion to support the stations. In [21], a bi-level planning model considers both investor costs and user satisfaction. The upper level minimizes construction costs and network losses using an improved Particle Swarm Optimization, while the lower level evaluates user satisfaction by minimizing travel time and expenses, considering queue times and distances through Dijkstra’s algorithm and queuing theory. In [22], a bi-level programming model determines optimal EV charging station allocation in the presence of wind turbines. The upper level maximizes station profit, while the lower level minimizes power losses using available sources and dynamic feeder reconfiguration. The impacts of cryptocurrency miners and demand-side management are also considered. In [23], a combined road transport and electric distribution network model is proposed for strategic EV charging station deployment. A bi-level optimization approach minimizes user travel costs, power losses, and voltage deviations, employing PSO-DS for station placement, convex optimization for traffic equilibrium, and AC OPF for grid operation. In [24], a bi-level EV charging station planning model considers spatiotemporal load distribution under uncertainty. The lower level predicts charging demand using OD matrices, dynamic Dijkstra routing, and LHS, while the upper level minimizes station planning costs and user behavior, and also accounts for distribution operation costs and emissions from uncertain renewables. In [25], a bi-level planning model for EV charging stations in coupled distribution-transportation networks is proposed to enhance post-fault security. The upper level optimizes station locations and capacities, while the lower level designs EV charging routes to minimize overall travel costs.

Investment in FCSs is typically made by private investors whose economic objectives often differ from those of the DSO. Although many studies have addressed the siting and sizing of FCS, most focus on either transportation behavior or distribution network operation, and do not capture the economic interaction between private investors and the DSO, especially when electricity prices are determined through network-constrained optimal power flow. To address this gap, this paper proposes a multi-objective bi-level model that jointly determines FCS locations, capacities, and energy exchange prices. The main novelties of this study are as follows:

TABLE I
Comparative Analysis of Different Articles with the Proposed Model

Ref number	Objective function	Decision Variables			Traffic model	Optim model		Stakeholders Considered		Problem Focus		Methode of optimization
		Location	Size	Price		Bi-level	single-level	FCS owner	DSO	electrical	Transport	
[1]	minimizing travel time and infrastructure costs	✓	-	-	re-routing behaviours of travellers	✓	-	✓	-	-	✓	cross-entropy method
[2]	Maximizing profit	✓	-	-	user-equilibrium traffic	-	✓	✓	-	-	✓	GA
[4]	maximizing the traffic flow coverage	✓	✓	-	Driving Range-Based Traffic Flow Capturing Model	-	✓	-	✓	✓	✓	improved PSO
[5]	Minimizing total costs	✓	✓		simple	-	✓	-	✓	✓	✓	PSO
[6]	minimize total costs	✓	✓		simple	-	✓	-	✓	✓	✓	Harris Hawk Optimization
[9]	minimize total costs	✓	✓	-	simple	✓	-	-	✓	✓	✓	
[10]	maximizes investor profits	✓	✓	-	`simple	✓	-	✓	-	✓	✓	KKT trans
[11]	minimize the fleet's total charging time	✓	✓	-	online vehicle-charging assignment	✓	-	✓	-	-	✓	A surrogate-assisted optimi approach
[12]	minimizes infrastructure costs	✓	✓	-	User Equilibrium traffic assignment	✓	-	✓	-	✓	-	-
[14]	minimize overall traffic time and investment costs	✓	✓	-	User Equilibrium traffic assignment	✓	-	✓	-	-	✓	Descent algorithm
[18]	Minimizing installation costs	-	✓	-	simple	✓	-	✓	-	-	✓	tailored column generation-based heuristic algorithm
[19]	minimizing losses and operating costs	✓	-	-	-	✓	-	-	✓	✓	-	PSO
[23]	minimizes user travel costs, power losses,	✓	✓	-	traffic equilibrium	✓	-	-	✓	✓	-	PSO
Prop model	**maximizes investor profits**	✓	✓	✓	**user-equilibrium traffic +Queing theory**	✓	-	✓	✓	✓	✓	**KKT trans**

1- The integration of FCS private investor and DSO objectives within a bi-level framework.

2- the simultaneous optimization of FCS location, sizing, and electricity exchange pricing under network constraints, with the bi-level model transformed into a single-level formulation using Karush-Kuhn-Tucker (KKT) conditions.

The rest of this paper is organized as follows: the bi-level model for determining the location and capacity of FCSs and the DC optimal power flow of the distribution network is presented in Section II. Simulation results and sensitivity analysis are presented in Section III, and Section IV concludes the paper results and future works.

II. BI-LEVEL OPTIMIZATION APPROACH

In this paper, a two-level model is proposed to represent the interaction between the charging station owner and the distribution network operator. Before implementing the two-level model, the charging demand of each candidate station is first determined by considering the user equilibrium-based traffic assignment model and queuing theory. In the two-level model and at the high level, by determining the energy purchase price from the distribution network at the location of each FCS and maximizing the profit of the charging station owner, the locations of the charging stations are determined. By determining the locations of the charging stations and adding the electric power demand of these stations to the distribution network, and to minimize the cost of energy production for the distribution network operator, the energy sales price at each busbar is determined. This price will be the same as the energy sales price to the charging stations installed on the same busbar. The energy sales price to the charging stations is transferred to the high-level problem as a known parameter, and this process will continue until the final answer is reached. This model is shown in Fig. 1. The user equilibrium-based traffic assignment model, the queue theory, and the UL and LL problems are formulated below.

A. The User Equilibrium-based Traffic Assignment Model

In the proposed method, traffic information is used to simulate the behavior of electric vehicles and estimate charging demand. However, raw traffic flow data cannot be directly used in the planning of charging stations. As a result, daily origin-destination data are used to generate traffic flows. To obtain these data, an optimal system allocation model is used to generate and allocate traffic flows on each route of the transportation network [26]. The objective of the optimal system allocation model is to achieve the minimum travel cost, according to equations (1a) to (1b).

$$\min \sum_{a} fr_a . t_a \tag{1a}$$

$$\sum_{k} fp_{r,u,k} = q_{r,u} \quad \forall r, \forall u \tag{1b}$$

$$fp_{r,u,k} \geq 0 \quad \forall r, \forall u, \forall k \tag{1c}$$

$$fr_a = \sum_{r}\sum_{u}\sum_{k} fp_{r,u,k} . \delta_{r,u,k,a} \qquad \forall r, \forall u, \forall k \tag{1d}$$

$$t_a = t_a^0 \left[1 + b\left(\frac{fr_a}{c_a} \right)^{v} \right] \tag{1e}$$

Equation (1a) is the objective function of the problem, which represents the minimization of the travel cost. Equation (1b) guarantees the principle of network flow conservation. This relation means that the sum of the flow of all paths between each origin-destination is equal to the travel demand of that origin and destination. In this relation, the condition of non-negativity of the traffic flow on the kth path between origin r and destination u is also considered. Equation (1d) indicates that the traffic flow on road *a* is equal to the sum of the flows on all paths that include road *a*. The travel time on road *a*, given the accumulated flow on this road, is shown in (1e).

B. Capacity of Candidate FCSs Based on Queueing Theory

Queuing theory is often used to mathematically analyze the outcome of random arrivals of customers to receive service from the system. After obtaining the equilibrium traffic flow of each route, the random movement of vehicles and the capacity of charging stations are analyzed using queuing theory. The charging station service system is considered an M/M/S queue system. Queue service models are represented by the abbreviation (A/B/C), where A represents the distribution between two consecutive arrivals. Since the arrival time of each vehicle at the charging station is a random variable, in this paper, the arrivals of these vehicles are considered as a Poisson distribution. The second term, B, represents the distribution of the service duration, which is assumed to follow a uniform distribution, and the third term represents the number of service providers (chargers at a station).

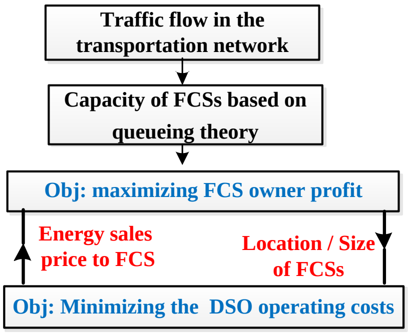

Fig. 1: The prposed bi-level model

One of the important parameters in the Poisson process is its mean value. It is assumed that electric vehicles have a similar driving pattern to conventional vehicles and that the average arrival rate of vehicles at each FCS is proportional to the traffic flow attracted by that FCS. Thus, the mean arrival rate of EVs in the *k*th FCS at time t can be calculated as:

$$\lambda_{k,t} = C(1-\sigma)(1-\beta)\frac{f_t^{trip}}{\sum_{t} f_t^{trip}} \frac{f_{k,t}}{\sum_{k} f_{k,t}} \quad \forall k, \forall t \tag{2a}$$

The capacity of charging stations can be calculated as a nonlinear integer programming model, assuming that qμ is independent of the vehicle arrival rate, based on a Poisson process and an exponential distribution of the service time of each device according to the M/M/S queue model. Here, M/M/S represents a queue model with identical servers, where arrival is determined by a Poisson process and service time follows a negative exponential distribution [27]:

$$Obj: \min\ z_k \tag{3a}$$

$$\lambda_k^{RH} = \max\left\{ \lambda_{k,t} \right\} \tag{3b}$$

$$W_k^{RH} \leq W^{allowed} \quad \forall k \tag{3c}$$

$$W_k^{RH} = \frac{\left(z_k . \rho_k^{RH} \right)^{z_k} . \rho_k^{RH}}{\lambda_k^{RH} \left(z_k \right)! \left(1 - \rho_k^{RH} \right)^2} \pi_{0,k} \quad \forall k \tag{3d}$$

$$\pi_{0,k} = \left[\sum_{n=0}^{z_k - 1} \frac{\left(z_k \rho_k^{RH} \right)^n}{n!} + \frac{\left(z_k \rho_k^{RH} \right)^{z_k}}{\left(z_k \right)! \left(1 - \rho_k^{RH} \right)} \right]^{-1} \tag{3e}$$

$$\rho_k^{RH} = \frac{\lambda_k^{RH}}{z_k \mu} \tag{3f}$$

The objective function shown in (3a) is to minimize the number of fast charging nozzles required in the FCS. Equation (3c) shows that the average waiting time for charging during peak traffic hours should be within a predefined range. Equation (3d) explains how to calculate the waiting time in the queue theory. The probability that there are no vehicles under charging service in the FCS is represented by $\pi_{0,k}$. By increasing the number of charging devices, the waiting time in the queue can be reduced. In general, proper charging service and service facilitation can significantly increase the penetration rate of electric vehicles. However, on the other hand, increasing the number of charging devices increases the investment in the project, which is not economically feasible. Therefore, in order to optimally install charging stations, a criterion is used to consider the tolerance threshold of wallowed customers for charging at each charging station. In this way, if the customer's waiting time exceeds a certain time, the customer will leave the charging station. Since obtaining the inverse functions and the direct solution of the relationship is a complex task, a counting method is used to solve it. In this method, an initial value for the number of charging devices is assigned to the candidate locations of charging stations according to the maximum $\lambda_{k,t}$ in the time periods. In each iteration, one unit is added to the number of charging devices, and W^{RH} is calculated, and its value is compared with $W^{allowed}$. This continues until the average waiting time for charging is less than a certain value. The obtained value Z_k will be the economic number of charging devices. Once the size of each FCS is obtained, the total charging demand at each time can be calculated according to (4a) and (4b).

$$P_{k,t}^{FCS} = \rho_{k,t} . z_k . p^{FCS} \quad \forall k,t \tag{4a}$$

$$\rho_{k,t} = \frac{\lambda_{k,t}}{z_k . \mu} \quad \forall k,t \tag{4b}$$

C. Upper-Level Problem

The UL problem objective is to determine the location and capacity of FCS installations, aiming to maximize the profits of the private owner.

$$\underset{UL}{Maximize}\left(R^{FCS} - \mathrm{Cos}\,t^{FCS} - C^{inv}\right) \tag{5a}$$

$$R^{FCS} = 365.C^{sell}.\sum_{i\in I}\sum_{t\in T} U_i . P_{i,t}^{FCS} \tag{5b}$$

$$Cost^{FCS} = 365\sum_{t\in T}\sum_{k\in K} Cost_{i,t}^{up} \tag{5c}$$

$$C^{inv} = \frac{\varepsilon(1+\varepsilon)^{n_{FCS}}}{(1+\varepsilon)^{n_{FCS}} - 1}\sum_k u_k\left(\alpha^{CHF} z_k + \alpha_k^{LS} z_k + \alpha_k^F\right) \tag{5d}$$

$$-U_i.bigM \le Cost_{i,t}^{up} \le U_i.bigM \tag{5e}$$

$$Cost_{i,t}^{up} \le \left(1 - U_i\right).bigM + \lambda_{i,t}.P_{i,t}^{fcs} \tag{5f}$$

$$Cost_{i,t}^{up} \ge -\left(1 - U_i\right).bigM + \lambda_{i,t}.P_{i,t}^{fcs} \tag{5g}$$

According to (5a), the objective function of the problem is to maximize the profit of the private owner, which includes the income from selling energy to electric vehicles, the cost of purchasing energy from the distribution network, and the cost of establishing FCSs, which are given in (5b) – (5c), respectively. According to (5e)– (5g), if an FCS is established, the cost of purchasing energy from the distribution network will be obtained by multiplying the purchased power by the hourly price of energy in the relevant bus.

It should be noted that the energy price per bus is the dual variable related to the constraint of equality of generated and consumed power per bus, which is obtained from the low-level problem.

D.Lower-Level Problem

The lower-level problem aims to minimize the energy production costs for the distribution network operator. For this purpose, DC optimal Power flow equations have been used, which are expressed in (6a)–(6g).

$$\underset{LL}{\text{Minimize}}\sum_t\sum_s \omega_s.\Big(\sum_g C_g P_{g,t,s} + C_{t,s}^{grid} P_{i=1,t,s}^{grid} + \sum_i C^{ls} P_{\mathrm{i},t,s}^{ls}\Big) \tag{6a}$$

$$\sum_{\square(\mathrm{g})=i} P_{g,t,s} + P_{i=1,t,s}^{grid} = P_{i,t,\mathrm{s}}^{L} - P_{i,t,s}^{LS} + P_{i,t}^{FCS} + \sum_{s(\mathrm{l})=i} P_{l,t,s}^{flow} - \sum_{r(\mathrm{l})=i} P_{l,t,s}^{flow} \quad \forall i,\mathrm{t},s \quad : \lambda_{i,t,s} \tag{6b}$$

$$P_{l,t,s}^{flow} = B_l\left(\theta_{s(\mathrm{l}),\mathrm{t,s}} - \theta_{\mathrm{r(l),t,s}}\right) \quad \forall l,t,s: \quad \rho_{l,t,s} \tag{6c}$$

$$-\overline{P_l} \le P_{l,t,s}^{flow} \le \overline{P_l} \quad \forall l,t,s \ : \mu_{l,t,s}^{-}, \mu_{l,t,s}^{+} \tag{6d}$$

$$p_{i=1,t,s}^{grid} \ge 0 \quad ;\delta_{i=1,t,s}^{1} \tag{6e}$$

$$0 \le P_{g,t,s} \le \overline{P_g} \quad \forall g, \forall \mathrm{t}, \forall s \quad : \delta_{g,t,s}^{-}, \delta_{g,t,s}^{+} \tag{6f}$$

$$0 \le P_{\mathrm{i},t,s}^{LS} \le PD_{i,t,s} \quad \forall i, \forall t, \forall s: \ \eta_{i,t,s}^{-}, \eta_{i,t,s}^{+} \tag{6g}$$

The primal set of variables for each LL problem is $\Xi^{primal} = P_{i=1,t,s}^{grid}, P_{g,t,s}, \theta_{l,t,s}, P_{i,t,s}^{LS}$ while its dual set of variables is

$$\Xi^{dual} = \lambda_{tis}, \rho_{lts}, \mu_{lts}^{+}, \mu_{lts}^{-}, \delta_{ts}^{1}, \delta_{gts}^{+}, \delta_{gts}^{-}, \eta_{lts}^{+}, \eta_{lts}^{-}$$

The objective function of the low-level problem, which is to minimize the operating costs of the distribution network, is shown in (6a). This cost includes DG's energy production costs, the cost of purchasing energy from the upstream grid, and the load shedding cost. The equation (6b) ensures equality of generation and consumption power on each bus. The DC load flow is expressed in (6c).

The minimum and maximum power passing through each line is shown in (6d). The equation (6e) indicates that the distribution network is connected to the upstream grid via Bus 1. The network only receives energy from the upstream grid, and the possibility of selling energy back is not considered. The minimum and maximum generator capacities, as well as the curtailed load, are specified in the (6f)-(6g).

It is worth noting that the dual variable of each constraint is written in the same equation.

E. Transforming the Bi-Level Model to a Single-Level

If the LL problem is linear and convex, the bi-level model can be transformed into a single-level model using the KKT conditions, which introduce inherently non-linear complementary constraints. Since the proposed model's LL problem is linear and convex, the KKT conditions are applied to convert it into a single-level problem. This single-level linear optimization problem, known as a Mathematical Program with Equilibrium Constraints (MPEC), can then be solved using solvers such as CPLEX.

$$\underset{\Xi UL}{\textbf{Maximize}}\ (1a) \tag{7a}$$

Subject to
(5b)-(5g),(6b),(6c) (7b)

$$C_{t,s}^{grid} - \lambda_{i,t,s} - \delta_{i=1,t,s}^{1} = 0 \qquad \forall i = 1, \forall t, \forall s \tag{7c}$$

$$\lambda_{i=r(l),t,s} - \lambda_{i=s(l),t,s} + \rho_{l,t,s} - \mu_{l,t,s}^{-} + \mu_{l,t,s}^{+} = 0 \qquad \forall l,t,s \tag{7d}$$

$$C^{ls} - \lambda_{i,t,s} - \eta_{i,t,s}^{-} + \eta_{i,t,s}^{+} = 0 \quad \forall i,t,s \tag{7f}$$

$$\rho_{r(i)=l,t,s} - \rho_{s(i)=l,t,s} = 0 \quad \forall i,t,s \tag{7g}$$

$$0 \le \left(\overline{P_l} - P_{l,t,s}^{flow}\right) \perp \ \mu_{l,t,s}^{+} \ge 0 \quad \forall l, \forall \mathrm{t}, \forall s \tag{7h}$$

MPEC

Optimal siting /sizing of FCSs

Maximizing the profit of FCS invester (UL objective function)

Subject to:

Upper-level constraint
lower level constraint
Optimization constraint of KKT
complementary constraint of KKT

Fig. 2: The framework of the proposed model as MPEC

$$0 \le \left(P_{l,t,s}^{flow} + \overline{P_l}\right) \perp \ \mu_{l,t,s}^{-} \ge 0 \quad \forall l, \forall t, \forall s \qquad (7i)$$

$$0 \le p_{i,t,s}^{grid} \ \perp \delta_{i,t,s}^{1} \ge 0 \quad \forall i = 1, \forall t, \forall s \qquad (7g)$$

$$0 \le P_{i,t,s}^{LS} \perp \ \eta_{i,t,s}^{-} \ge 0 \quad \forall i, \forall t, \forall s \qquad (7k)$$

$$0 \le \left(PD_{i,t,s} - P_{i,t,s}^{LS}\right) \perp \eta_{i,t,s}^{+} \ge 0 \quad \forall i, \forall t, \forall s \qquad (7l)$$

$$0 \le P_{g,t,s} \perp \delta_{g,t,s}^{-} \ge 0 \quad \forall g, \forall t, \forall s \qquad (7m)$$

$$0 \le \left(\overline{P_g} - P_{g,t,s}\right) \perp \ \delta_{g,t,s}^{+} \ge 0 \quad \forall g, \forall t, \forall s \qquad (7n)$$

$$0 \le P_{i,t,s}^{LS} \perp \ \eta_{i,t,s}^{-} \ge 0 \quad \forall i, \forall t, \forall s \qquad (7o)$$

$$0 \le PD_{i,t,s} - P_{i,t,s}^{LS} \ \perp \eta_{i,t,s}^{+} \ge 0 \quad \forall i, \forall t, \forall s \qquad (7p)$$

Eq. (7a) shows that the MPEC model objective function is the same as the UL problem function. Constraint (7b) contains the UL constraints and the equality constraints included in the LL problems. Equalities (7c)–(7g) and the complementarity conditions (7h)–(7p) are the KKT optimality conditions of the LL problems.

F. MPEC Linearization

The MPEC single-level model is a non-linear problem because of complementary constraints, in (7h)–(7p). Because the presence of non-linear complementary constraints makes the obtained single-level model non-linear, the suggested model is linearized using a technique based on auxiliary binary variables and suitably large integers. For example, linearization of 0 ⩽ a ⊥ b ⩾ 0 is (8): [28]

$$\begin{cases} 0 \le a \le U.M \\ 0 \le b \le \left(1-U\right).M \\ U \in \left[0,1\right] \end{cases} \qquad (8)$$

Note that the variables of the resulting MILP are those included in the set, as well as the auxiliary binary variables used for the linearization of the complementarity conditions. The framework of the proposed model as MPEC is illustrated in Fig. 2.

III. CASE STUDY

To implement the proposed concepts, the IEEE 33-bus system [29] (Fig. 3) and the transportation network presented in [30] (Fig. 4) have been used. The transportation network includes 24 traffic nodes and 21 Sioux Falls routes. This network consists of 76 paths, 24 nodes, and 552 origin-destination pairs. The loads at various buses of the distribution network follow a 24-hour load profile as shown in Fig. 5. The network operates at a voltage level of 12.66 kV and is fed from the substation located at bus 1. The maximum power passing through the lines is assumed to be 3000 kW. Additional information about this network can be found in [30]. Candidate locations for installing FCS and the investment costs associated with each location are provided in Table I.

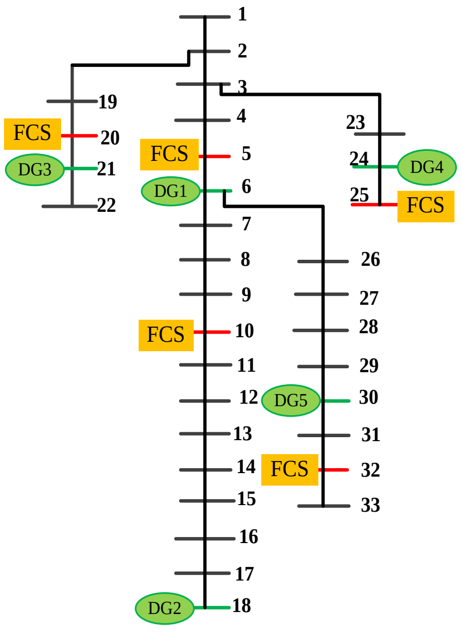

Fig. 3: IEEE 33-bus electrical network

TABLE I

Construction Costs of FCS

Candidate FCS	**1**	**2**	**3**	**4**	**5**
location	12[a] (5)[b]	3[a] (10)[b]	10[a] (20)[b]	15[a] (25)[b]	18[a] (32)[b]
$\alpha^{CHF}(10^4\$)$	2.35	2.35	2.35	2.35	2.35
$\alpha^{LS}(10^4\$)$	1.017	1.068	0.814	0.916	1.017
$\alpha^{k}(10^4\$)$	16.3	16.3	16.3	16.3	16.3

[a] node number in transportation network

[a] node number in electrical network

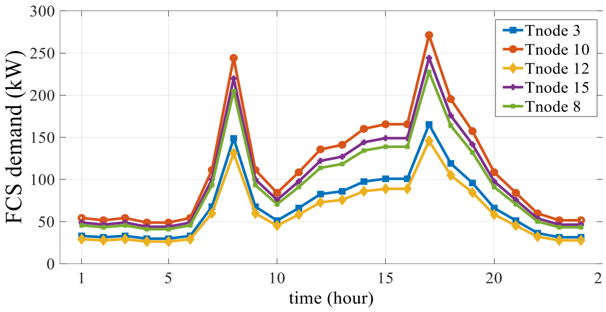

Fig. 6 : FCS hourly demand

Considering the candidate locations for installing FCSs and using the user equilibrium-based Traffic assignment and queuing theory models, the power demand of each candidate FCS is shown in Fig. 6. The electricity selling price to electric vehicles, which is one of the key factors influencing the charging station owner’s decision, is also shown in Fig. 7 .Other parameters required to implement the model are also given in the Table II.

TABLE II

Settings of Some Crucial Parameters

parameter	**value**	**parameter**	**value**
Z_{min}	6	Z_{max}	10
$W_{allowed}$	5 min	n_{FCS}	5
ε	10%	C_{LS}	2.5 $/kwh
B_{sell}	1.35 $/kwh		

TABLE III

Summary of Simulation Results

parameter	**value**
Optimal installation location	**[15,18]**
Charger number	**[9,7]**
FCS Owner's profit	**6,147 $**
Investment cost	**139,255 $**
FCS cost	**2,183,639 $**
FCS revenue	**2,329,041 $**

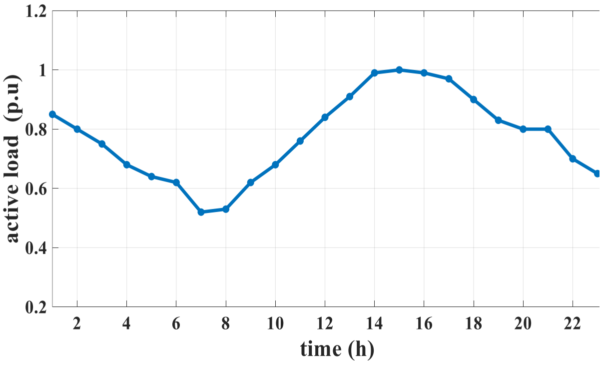

Fig.5: Load profile

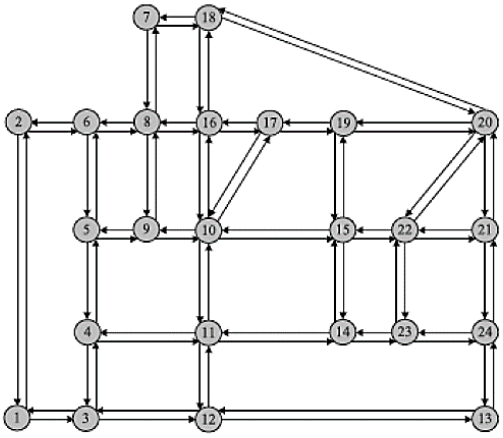

Fig. 4: Sioux Falls transportation network

A. Simulation and results analysis

The proposed MILP bi-level model was implemented in the GAMS software, and with the CPLEX solver, the results of which are given in Table III.

Analyzing the results, the FCS owner will establish two FCS at traffic nodes 15 and 18 (25 and 32 of the electrical network) with 9 and 7 chargers, respectively. By establishing these two stations, the station owner will earn a profit of $6,174, of which 139,255 $ will be spent on establishing the station and $2,183,369 on purchasing energy from the distribution network. There will also be an income of $2,329,041 from selling energy to electric vehicles.

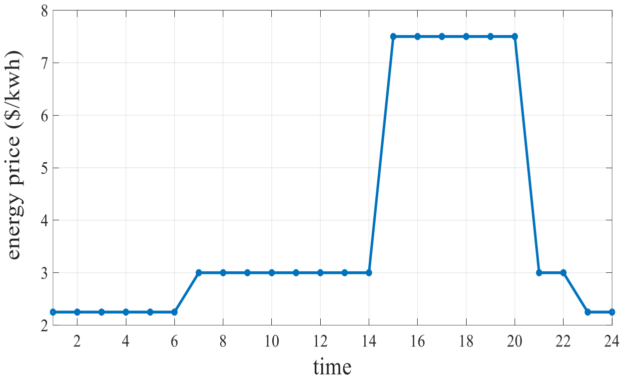

Fig. 7: Price of purchasing energy from the upstream network during the day

In this case, the cost to the DSO is 105,934,300 $. In this case, the cost of generating energy by DGs, the cost of purchasing energy from the upstream network, and the cost of LS in one day are 31,496 $, 246,440 $, and 12,293 $, respectively. Given the presence of three DGs in the distribution network, the active power generated by each DG is shown in Fig. 8

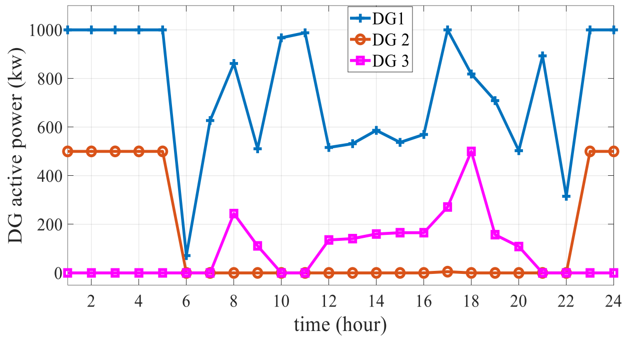

Fig. 8: DG active power

Fig. 9 illustrates the temporal and spatial variations of the nodal electricity prices across different buses over a 24-hour period. As shown, the LMP values are generally low and uniform during off-peak hours, indicating balanced power flow and low network congestion. However, during hours 16–19, a significant increase in the LMP is observed at several buses (particularly around buses 5 and 20), reflecting higher demand and possible local congestion in the distribution feeders. These higher nodal prices are directly linked to the power balance constraints in the lower-level optimization, where dual variables represent the marginal cost of supplying an Additional unit of power. These LMPs are used as the reference prices for energy transactions between the DSO and the FCS owners in the bi-level framework.

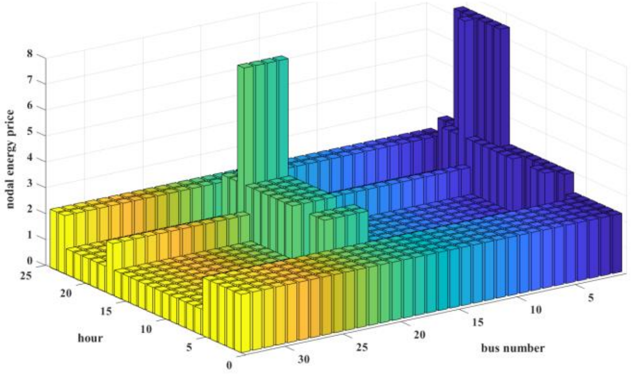

Fig. 9: nodal energy price

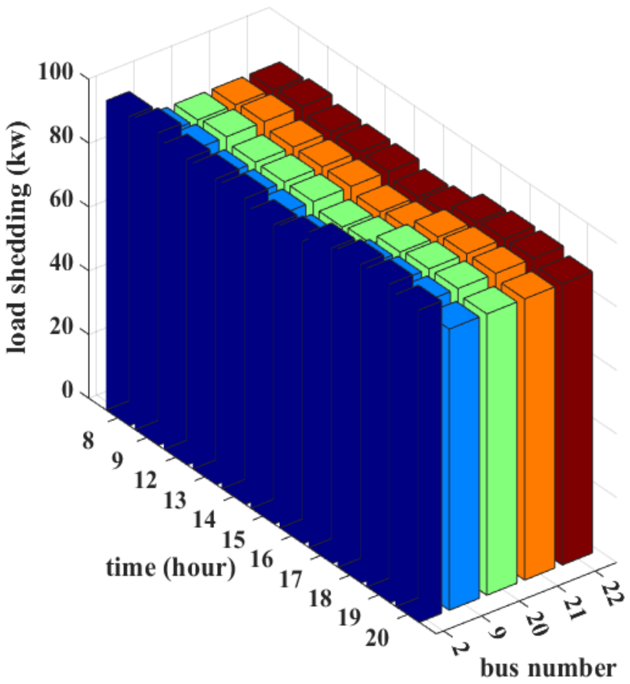

Fig. 10: Load shedding

TABLE IV
Optimal Locations and Number of FCSs Under Different Electricity Selling Prices to EV Drivers

Price ($/kWh)	profit	Bus number	Chargers number
1.35	6,146	25,32	9,7
1.36	23,398	25,32	9,7
1.37	40,650	25,32	9,7
1.38	59,390	5,25,32	6,9,7
1.39	86,037	5,10,25,32	6,8,9,7

The amount of LS on each bus over 24 hours is also shown in Fig. 10. As illustrated in the figure, during the early hours before 8:00, when the network load is relatively low, no load shedding occurs. However, as the demand increases after this period, certain buses experience load curtailment to maintain system stability and prevent overloading conditions.

B. Sensitive analysis:

To assess the robustness of the proposed model, a sensitivity analysis is performed on the electricity selling price to EVs, which directly impacts the profitability and, consequently, the location and capacity decisions of the charging stations.

As shown in Table IV, the location and number of FCSs change with variations in the electricity selling price to electric vehicles. At lower prices (1.35–1.37 $/kWh), the optimizer selects buses 25 and 32 as the most profitable locations, each with 9 and 7 chargers, respectively. In this range, the profit gradually increases with the selling price, while the optimal sites remain unchanged. When the price increases to 1.38 $/kWh, an additional station is installed at bus 5, indicating that higher revenues justify expanding the charging infrastructure. Finally, at 1.39 $/kWh, another station appears at bus 10, leading to a network of four charging stations and the highest total profit. This trend shows that as the selling price rises, the profitability of the investment improves, encouraging the deployment of more FCSs in additional locations across the network.

IV. CONCLUSION AND FUTURE WORK

In this study, a bi-level optimization framework is developed for the siting and sizing of fast-charging stations, considering the interaction between the distribution system operator and the FCS investor. The lower level minimizes network operational costs via a DC optimal power flow, generating locational marginal prices that are passed to the upper level. The upper level maximizes the investor’s profit by determining optimal FCS locations and capacities based on electricity prices and charging demand, modeled through a user-equilibrium traffic assignment and M/M/S queuing theory. The model is reformulated as a mixed-integer linear program using Karush–Kuhn–Tucker conditions and solved in GAMS. Simulation results on the IEEE 33-bus distribution system coupled with a 25-node transportation network demonstrate that the proposed approach identifies two optimal FCS locations with 9 and 7 chargers, resulting in a net daily profit of $6,147 for the investor, while maintaining feasible network operation. The derived locational marginal prices vary spatially and temporally, directly influencing investment decisions. Sensitivity analysis indicates that higher electricity selling prices shift optimal locations and increase investor profit.

In this study, the power demand at each candidate location for establishing FCSs was predefined. The selection or non-selection of a candidate site does not affect the charging demand of other stations. However, in reality, part of the charging demand from nearby stations may shift to the newly established ones. The dynamic behavior of charging demand among stations can play a significant role in the investor’s siting decisions as well as in satisfying the distribution network constraints. However, considering this dynamic behavior would make the cost of purchased energy from the DSO nonlinear, preventing the use of conventional solvers such as CPLEX to solve the problem.

ACKNOWLEDGMENT

The authors gratefully acknowledge the valuable support and constructive comments received during the preparation of this work. Their contributions significantly improved the quality of this study.

FUNDING STATEMENT

The authors declare that they have no known competing financial interests or personal relationships that could have appeared to influence the work reported in this paper.

CONFLICT OF INTEREST

The authors declare that they have no known competing financial interests or personal relationships that could have appeared to influence the work reported in this paper.

AUTHORS' CONTRIBUTIONS

Mohammad Alizadeh: Conceptualization, Methodology, Investigation, Software. Ali godarzi amlashi: Supervision, Validation, Writing – review & editing.

REFERENCES

[1] C. Q. Tran, D. Ngoduy, M. Keyvan-Ekbatani, and D. Watling, "Bi-level optimization for locating fast-charging stations in large-scale urban networks," in *2020 Forum on Integrated and Sustainable Transportation Systems (FISTS)*, 2020, pp. 205-210.

[2] Y. Huang and K. M. Kockelman, "Electric vehicle charging station locations: Elastic demand, station congestion, and network equilibrium," *Transportation Research Part D: Transport and Environment,* vol. 78, p. 102179, 2020/01/01/ 2020.

[3] C. dos Santos, A. J. C. G., O. W. A., and C. and Lyra, "Optimal allocation of fast charging stations for large-scale transportation systems," *International Journal of Production Research,* vol. 62, no. 14, pp. 5087-5107, 2024/07/17 2024.

[4] A. Kapoor, V. S. Patel, A. Sharma, and A. Mohapatra, "Optimal Planning of Fast EV Charging Stations in a Coupled Transportation and Electrical Power Distribution Network," *IEEE Transactions on Automation Science and Engineering,* vol. 21, no. 3, pp. 4261-4271, 2024.

[5] S. Silapan, S. Patchanee, N. Kaewdornhan, S. Somchit, and R. Chatthaworn, "Optimal Sizing and Locations of Fast Charging Stations for Electric Vehicles Considering Power System Constraints," *IEEE Access,* vol. 12, pp. 139620-139631, 2024.

[6] S. Nandi, S. R. Ghatak, P. Acharjee, and F. Lopes, "Multi-Scenario-Based Strategic Deployment of Electric Vehicle Ultra-Fast Charging Stations in a Radial Distribution Network," *Energies,* vol. 17, no. 17, p. 4204, 2024.

[7] L. Chen, C. Xu, H. Song, and K. Jermsittiparsert, "Optimal sizing and siting of EVCS in the distribution system using metaheuristics: A case study," *Energy Reports,* vol. 7, pp. 208-217, 2021/11/01/ 2021.

[8] A. K. Mohanty, P. Suresh Babu, and S. R. Salkuti, "Optimal Allocation of Fast Charging Station for Integrated Electric-Transportation System Using Multi-Objective Approach," *Sustainability,* vol. 14, no. 22, p. 14731, 2022.

[9] B. Zhang, Z. Meng, and X. Hu, "Location planning of electric vehicle charging station with users’ preferences and waiting time: multi-objective bi-level programming model and HNSGA-II algorithm," *International Journal of Production Research,* vol. 61, no. 5, pp. 1394-1423, 2023/03/04 2023.

[10] Y. Liu, Y. Xiang, Y. Tan, B. Wang, J. Liu, and Z. Yang, "Optimal Allocation Model for EV Charging Stations Coordinating Investor and User Benefits," *IEEE Access,* vol. 6, pp. 36039-36049, 2018.

[11] T.-Y. Ma and S. Xie, "Optimal fast charging station locations for electric ridesharing with vehicle-charging station assignment," *Transportation Research Part D: Transport and Environment,* vol. 90, p. 102682, 2021/01/01/ 2021.

[12] G. Ferro, R. Minciardi, L. Parodi, and M. Robba, "Optimal planning of charging stations and electric vehicles traffic assignment: a bi-level approach," *IFAC-PapersOnLine,* vol. 53, no. 2, pp. 13275-13280, 2020/01/01/ 2020.

[13] D. Hu, K. Zhou, and X. Lu, "A bi-level programming model for inter-city charging station location with heterogeneous range anxiety," *Energy,* vol. 316, p. 134619, 2025/02/01/ 2025.

[14] G. Zhou, Q. Dong, Y. Zhao, H. Wang, L. Jian, and Y. Jia, "Bilevel optimization approach to fast charging station planning in electrified transportation networks," *Applied Energy,* vol. 350, p. 121718, 2023/11/15/ 2023.

[15] Ö. B. Kınay, F. Gzara, and S. A. Alumur, "Charging Station Location and Sizing for Electric Vehicles Under Congestion," *Transportation Science,* vol. 57, no. 6, pp. 1433-1451, 2023.

[16] K. Shen, K. Li, Y. Yu, and W. Yang, "Bi-level planning of electric vehicle charging station considering energy consumption per unit mileage," *Journal of Physics: Conference Series,* vol. 2849, no. 1, p. 012081, 2024/09/01 2024.

[17] W. Makhlouf, M. Kchaou-Boujelben, and C. Gicquel, "A bi-level programming approach to locate capacitated electric vehicle charging stations," in *2019 6th International Conference on Control, Decision and Information Technologies (CoDIT)*, 2019, pp. 133-138.

[18] L. Zhang, Z. Zeng, and K. Gao, "A bi-level optimization framework for charging station design problem considering heterogeneous charging modes," *Journal of Intelligent and Connected Vehicles,* vol. 5, no. 1, pp. 8-16, 2022.

[19] R. Aazami, M. M. Badan, M. Shirkhani, and A. Azizi, "Bi-level programming model of location and charging electric vehicle stations in distribution networks," *Results in Engineering,* vol. 24, p. 103657, 2024/12/01/ 2024.

[20] K. Li, C. Shao, Z. Hu, and M. Shahidehpour, "An MILP Method for Optimal Planning of Electric Vehicle Charging Stations in Coordinated Urban Power and Transportation Networks," *IEEE Transactions on Power Systems,* vol. 38, no. 6, pp. 5406-5419, 2023.

[21] X. Ma, Z. Liu, and C. Li, "Bi-level Location Planning Model for Charging Stations Based on User Satisfaction," in *The Proceedings*

of the 11th International Conference on Traffic and Transportation Studies, Singapore, 2025, pp. 164-174: Springer Nature Singapore.

[22] F. Asgharzadeh, V. S. Tabar, and S. Ghassemzadeh, "Stochastic bi-level allocation of electric vehicle charging stations in the presence of wind turbines, crypto-currency loads and demand side management," *Electric Power Systems Research*, vol. 220, p. 109383, 2023/07/01/ 2023.

[23] S. Muthukannan and D. Karthikaikannan, "A Framework Model for EV Charging Station Deployment in Transportation Network Synchronized With Distribution Network by a Bi-Level Hybrid Optimization Algorithm," *IEEE Access,* vol. 12, pp. 75689-75700, 2024.

[24] H. Gan, W. Ruan, M. Wang, Y. Pan, H. Miu, and X. Yuan, "Bi-Level Planning of Electric Vehicle Charging Stations Considering Spatial–Temporal Distribution Characteristics of Charging Loads in Uncertain Environments," *Energies*, vol. 17, no. 12, p. 3004, 2024.

[25] H. Li, Y. He, W. Fu, and X. Li, "Bi-level planning of electric vehicle charging station in coupled distribution-transportation networks," *Electric Power Systems Research,* vol. 232, p. 110442, 2024/07/01/ 2024.

[26] Y. Sahrayi, A. Pahlavanhoseini, and M. S. Sepasian, "Multi-objective planning of charging stations considering benefits of distribution company and charging stations owners," (in eng), *Iranian Electric Industry Journal of Quality and Productivity,* Research vol. 9, no. 3, pp. 41-55, 2020.

[27] W. Yao *et al.*, "A Multi-Objective Collaborative Planning Strategy for Integrated Power Distribution and Electric Vehicle Charging Systems," *IEEE Transactions on Power Systems,* vol. 29, no. 4, pp. 1811-1821, 2014.

[28] S. J. Kazempour, A. J. Conejo, and C. Ruiz, "Strategic Bidding for a Large Consumer," *IEEE Transactions on Power Systems,* vol. 30, no. 2, pp. 848-856, 2015.

[29] A. Ameli, S. Bahrami, F. Khazaeli, and M. R. Haghifam, "A Multiobjective Particle Swarm Optimization for Sizing and Placement of DGs from DG Owners' and Distribution Company's Viewpoints," *IEEE Transactions on Power Delivery,* vol. 29, no. 4, pp. 1831-1840, 2014.

[30] H. Fredriksson, M. Dahl, and J. Holmgren, "Optimal placement of Charging Stations for Electric Vehicles in large-scale Transportation Networks," *Procedia Computer Science,* vol. 160, pp. 77-84, 2019/01/01/ 2019.

.

Semnan University

Journal of Modeling & Simulation in Electrical & Electronics Engineering (MSEEE)

Journal homepage: **https://mseee.semnan.ac.ir/**

ISSN: 2821-0786

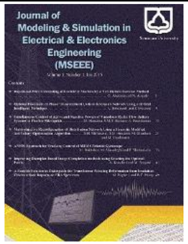

High-Fidelity Optical CNOT Gates Enabled by Rydberg-Mediated Phase Control

Ali Farmani [1]*and Anis Omidniaee[2]

***Abstract*--In this paper, we first design a photonic crystal laser chamber based on indium phosphide gallium arsenide and Zinc Oxide quantum dots due to the large energy gap of about 3.37 eV for laser beam propagation in terahertz applications. ZnO is easily grown in the form of nanorods, nanowires, and thin films and therefore can perform well in confined modes of photonic crystals. The results are obtained by examining the quality factor criteria of the dispersion temperature effect and the constant radius to lattice ratio to enhance spontaneous emission for improving optical pumping. In these materials, the quality factors for indium arsenide and aluminum oxide are 227.98 and 131.95, respectively, for the hybrid gain medium including gallium arsenide, aluminum oxide, and zinc oxide. Finally, the photonic crystal laser beam is driven to quantum logic gates, resulting in angle and rotation changes, and its probability function for quantum laser application are measured.**

***Index Terms*- Photonic Crystal, Quantum Dots, Gain Medium, CNOT Gate, Quantum Laser.**

I. INTRODUCTION

Due to their robust optical confinement and ease of transfer to non-native substrates, membrane photonic devices have garnered considerable scholarly attention [1]-[2]. The repositioning of electrodes to the device's lateral side [3] presents novel challenges in carrier injection technology, primarily because the membrane cladding layers are frequently composed of air or insulating materials. Carrier injection can transpire through two mechanisms: via a lateral pin junction, wherein the active material remains unaltered, or through a conventional vertical pin junction established during the epitaxial growth of the membrane [4]. Lateral doping, which is a regrowth technique, offers greater flexibility as the doping regions are localized and planar processing is maintained. When integrated with lateral injection and an embedded heterogeneous active region, it demonstrates enhanced efficiency. By creating a large-area standing wave coupled with light extraction in the vertical direction via first-order diffraction, the lateral coupling of light amplification and band-edge lasing is realized. The far-field pattern exhibits minimal divergence due to the extensive coherent resonance. In confined-mode nano lasers, the lasing threshold of colloidal quantum dots, when utilized alongside silicon nitride-based photonic crystals, can be as low as 10.5 kW/cm². This nano laser features a square lattice arrangement composed of cylindrical air holes within a dielectric plate having a refractive index of 10, with quantum dots embedded within. The power density is quantified at 5 kW/cm².

An even surface topography is paramount for effectively removing excess quantum dots from the surface in the confined state, ensuring complete filling of the air voids, and achieving a high-quality factor alongside a low lasing threshold [5]-[7].

The photonic crystal nano cavity is fabricated by superimposing two photonic crystal structures at a designated rotation angle, resulting in an exceptionally high-quality factor and significant

---

Received; 2025-10-31 Revised; 2025-12-06 Accepted; 2025-12-27

[1] Department of Nanoelectronics Engineering, Lorestan University, Khoramabad, Iran.
[2] Department of Nanoelectronics Engineering, Lorestan University, Khoramabad, Iran
*Corresponding author: Farmani.a@lu.ac.ir

Cite this article as:
Farmani, A. and Omidniaee, A. (2025). High-Fidelity Optical CNOT Gates Enabled by Rydberg-Mediated Phase Control. *Journal of Modeling & Simulation in Electrical & Electronics Engineering (MSEEE)*. Semnan University Press . *5 (4),* 45-53.
DOI: https://doi.org/10.22075/MSEEE.2025.39558.1237

light confinement within an extremely compact mode volume. In a twisted cavity, the resonance wavelength and optical mode distribution can be dynamically modified at the nanoscale through the random selection of the twist angle. These semiconductor nano lasers employ multiple quantum wells of indium gallium arsenide phosphide as the gain medium and demonstrate low lasing thresholds within the C-band. With a minimal area of approximately 25 μm² and a theoretical mode volume (Vm) of about 0.47 (λ/n)³, large-angle (5°) twisted photonic crystal nano lasers are optically pumped at ambient temperature, yielding single-mode emission with an extraordinarily low lasing threshold of approximately 1.25 kW/cm². Photonic crystal nano cavity lasers emit a continuous wave at a wavelength of 1540 nm, characterized by an extremely low threshold current of 10.2 μA. Indium phosphide-based photonic crystal lasers exhibit this threshold current of 10.2 μA [8]. The lateral pumping configuration of photonic crystal nano lasers experiences significant carrier leakage, which arises from unintended spontaneous emission at the pi interface, thus limiting the injection efficiency to a mere 3%, with a further decrease in efficiency observed at higher currents. Consequently, researchers have shifted their focus to the thermal stability of quantum dot materials derived from indium phosphide and aluminum gallium arsenide. The high density of the indium phosphide/aluminum gallium arsenide mixture enables accurate (001) orientation on gallium arsenide substrates; however, it necessitates relatively low substrate temperatures. [9]-[10].

However, indium phosphide/gallium arsenide quantum dot materials primarily have issues pertaining to material properties and growth dynamics. The relatively modest lattice mismatch of around 3. 2% in ArsinGaLiM, as opposed to around 7. 2%, reduces the strain energy during the Stransky Krastunov growth, which widens the size distribution of quantum dots. The presence of this inhomogeneity requires meticulous optimization of the growth process to achieve uniform and high-quality quantum dots. This is achieved by adjusting the layer thickness during the development of quantum dots in molecular beam epitaxy, utilizing a blend of indium phosphide and gallium arsenide deposition thickness, along with an altered indium alignment method in L and C-band quantum dot lasers. This approach leads to a low threshold current density of 21. 35 kA/cm[11]. The lower optical loss in the photonic crystal surface emitting laser designs with horizontal resonance and vertical emission in indium phosphide and gallium arsenide quantum dots, which have a larger single mode area, enables high power, single mode operation, and very low divergence angle.

To lower the threshold current to 80 mA, these nano lasers were created by implanting protons in the pcl adding layer. The laser wavelength is clearly dependent on the lattice constant, with each 5 nm increase in the lattice constant resulting in a 15 nm increase in the laser wavelength. The buried secondary epitaxial structure has shown exceptional performance, primarily due to the fact that the layer is close to the active region, which greatly enhances the optical confinement factor and improves the total device performance by increasing the optical feedback. The substrate side emission configuration allows for the side connection to the heat sink, therefore increasing thermal dissipation and enhancing the overall device performance. These discoveries offer useful guidance for the creation and optimization of high performance 1.3 m gallium arsenide-based surface emitting lasers [12]. Colloidal lead chalcogenide materials were regarded in quantum dot nanolasers. However, the exciton population was wiped out by high nonradiative Auger recombination caused by trap states, which degraded the light amplification and led to high gain thresholds. A binary mixture of colloidal lead quantum dots and zinc oxide nanocrystals was used to deactivate the trap states inside the sodium diethyl dithiophosphate gain medium. In addition, the transient absorption method reveals a fivefold enhancement in the Auger lifetime, indicating a reduction in trap-assisted Auger recombination. Consequently, the threshold for enhanced spontaneous emission at 1650 nm, with a linewidth of 1.23 nm, was halved. Despite this, these colloidal quantum dot nanolasers manage to achieve both stability and a high integration density at the same time. Research indicates that employing colloidal quantum dots with zinc selenide/cadmium selenide core-shell structures in a surface-based integrated circular Bragg resonator can result in a mode confinement factor approaching unity at 89% and a Purcell coefficient reaching as high as 22.7. This configuration also offers a significant confinement factor and a low laser threshold of 17 μJ/cm², which is 70% less than the threshold of 56 μJ/cm² observed in surface-emitting lasers with vertical cavity colloidal quantum dots [13]-[16]. Due to the self-assembled nature of StranskyKrastanov growth, conventional quantum dots encounter substantial difficulties in epitaxially controlling their spectral inhomogeneity and spatial nucleation position. In nanocavities integrated with small mode volumes, the cavity enhancement caused by the Purcell effect is weak in the coupling regime, even though thermal control and surface defect states continue to affect the high photon extraction efficiency of 85% in a circular Bragg grating resonator [17]. Buried photonic defects, which need little etching, may help microcavities made of these solve these issues. Selfassembly during epitaxial development results in their formation; their location is controlled at the quantum dot under a buried stress; hence, postgrowth lithography is not necessary [18]. Furthermore, the transient absorption technique demonstrates a fivefold increase in the Auger lifetime, suggesting a decrease in trap-assisted Auger recombination. As a result, the threshold for enhanced spontaneous emission at 1650 nm, which has a linewidth of 1. 23 nm, has been reduced by half. Nonetheless, these colloidal quantum dot nanolasers successfully combine stability with a high integration density. Studies show that using colloidal quantum dots with zinc selenide/cadmium selenide core-shell structures in a surface-mounted integrated circular Bragg resonator can achieve a mode confinement factor almost reaching unity at 89% and a Purcell coefficient as high as 22. 7. This setup also provides a notable confinement factor along with a low laser threshold of 17 μJ/cm², significantly lower than the 56 µJ/cm^2 threshold found in vertical cavity colloidal quantum dots from surface-emitting lasers. Additionally, selenide phosphide quantum dots display nonlinear features, including a modulation depth of 8. Additionally, selenide phosphide quantum dots display nonlinear features, including a modulation depth of 8.8%. [19].

The output power from these nanolasers reached 7 W, and they exhibited a brightness level of 180 mW/cm^2/s. However, during their development, particularly in structures made of gallium arsenide with certain structural constraints, a suspended bilayer torsional design linked to quantum dots in the near-infrared can easily be affected. Additionally, the mode field of the nanocavity primarily exists within the air gaps, which limits the effective interaction between the quantum dot and the cavity due to inadequate spatial overlap. Recently, researchers have been examining how a Moiré nanocavity interacts with a single quantum dot. Moiré nanocavities are created by the interaction of two identical photonic graphene layers that are twisted at a specific angle. When the Bloch modes of these layers couple, flat bands appear in the energy spectrum. These flat bands allow for light trapping that is not reliant on the momentum of the Bloch wave, leading to modes that have a group velocity of zero [20].

II. DESIGN AND STRUCTURE

A photonic crystal-based nano laser was developed utilizing the finite difference time domain numerical solution method. This design incorporated a hybrid gain medium consisting of a 10 nm thick layer of aluminum dioxide, which has a refractive index of 1. 75, alongside a gallium arsenide oxide dielectric layer. The primary objective of this configuration was to enhance optical pumping. This structure, as seen in Fig. 1, The photonic crystal profiles in the symmetric A-state and the antisymmetric B-state are shown in Fig. 1, is made up of a silicon substrate with a 40 nm thick aluminum gallium arsenide layer in the middle, and a gallium arsenide waveguide layer is formed on top of it with a 170 nm thickness, which is situated between two 40 nm thick aluminum gallium arsenide layers and two 5 nm thick gallium a layers, respectively. The membrane of the photonic crystal consists of a triangular lattice featuring air holes, with a lattice pitch, denoted as 'a', measuring 366 nm. In this context, a hole radius of 135. 4 nm, equivalent to 0. 37a, is considered. Photonic crystal nano lasers, which utilize thin semiconductor films in conjunction with single indium phosphide quantum dots, are particularly noteworthy due to their minuscule volume and ability to manipulate the magnetic field within the cavity, facilitating atom emission. This capability allows for the design of polarization-related patterns. The incorporation of silicon in these structures is advantageous due to its low cost, high integration potential, and compatibility with integrated circuit manufacturing processes. However, the optical pumping efficiency of these devices is constrained when paired with gallium arsenide and aluminum gallium arsenide materials. Research indicates that zinc oxide is a promising alternative, as it possesses a relatively high exciton binding energy of approximately 60 meV, which exceeds that of other materials.

$$n_{ave} = \sqrt{n^2{}_b(1-FF) + n_h{}^2 \cdot FF} \qquad (1)$$

where:

n_{ave} is the average (effective) refractive index of the composite photonic crystal medium. n_b represents the refractive index of the background (low-index) material, such as air or silica.$n_h$denotes the refractive index of the high-index material, such as semiconductors or dielectric rods embedded in the lattice FF is the fill factor, defined as the ratio of the volume (or area in two-dimensional structures) occupied by the high-index material to the total volume (or area) of the unit cell [21].

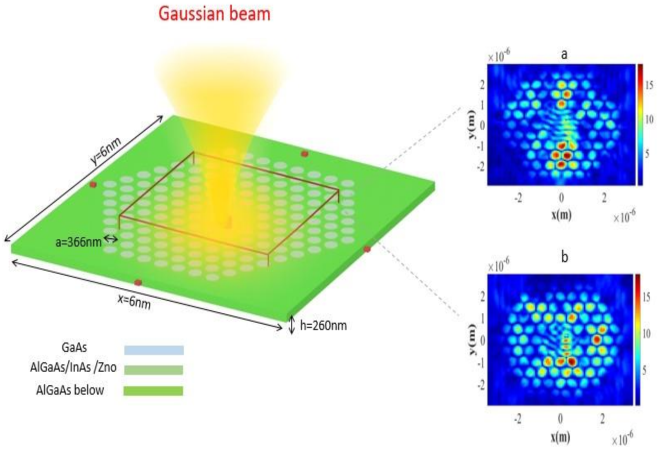

Fig. 1. Three-dimensional perspective of the photonic crystal nano laser architecture.

III. METHODS SECTION

In this work, we evaluate eight phase-shifting configurations, each defined by a unique combination of phase-step sequencing and modulation pattern. These configurations differ in their noise susceptibility, robustness to phase-step miscalibration, and sensitivity to harmonic distortions. Assessing all eight variants enables a systematic optimization of the reconstruction strategy and ensures that the selected configuration maximizes stability and accuracy under practical measurement conditions.

Step-by-Step Proposal of the Idea

Step 1: Selecting the Materials and Gain Media

The study begins by choosing suitable materials for the photonic crystal laser cavity: indium phosphide (InP), gallium arsenide (GaAs), aluminum oxide (Al_2O_3), and zinc oxide (ZnO) quantum dots. The rationale is based on their large energy gaps (~3.37 eV for ZnO), which make them appropriate for terahertz laser propagation and efficient optical pumping. ZnO is highlighted because it can be easily grown in nanorods, nanowires, or thin films, which helps achieve strong mode confinement in the photonic crystal cavity.

Step 2: Designing the Photonic Crystal Laser Cavity

A photonic crystal laser chamber is designed using these materials. The design considers dispersion effects, temperature dependence, and geometrical parameters such as the constant radius-to-lattice ratio to optimize the laser properties. The goal is to enhance spontaneous emission and overall optical pumping efficiency.

Step 3: Calculating Performance Metrics

The quality factor (Q-factor) of the cavity is evaluated to quantify performance. These calculations confirm that the cavity design supports efficient lasing and strong light-matter interaction.

Step 4: Application to Quantum Logic Gates

After optimizing the photonic crystal laser, it is applied to quantum logic gates. The study measures how the laser's angle, rotation, and probability function change in this context. This demonstrates the potential of the designed system for quantum laser applications, bridging photonic crystal laser technology with quantum information processing.

Step 5: Highlighting Novelty and Utility

The novelty lies in combining:

Hybrid gain media with high-Q factors. Nanostructured ZnO for strong confinement. Integration with quantum logic gates, showing practical quantum photonic applications.

IV. RESULTS AND DISCUSSIONS

The Gaussian emission spectrum is initially found at 1210 nm and 1110 nm, respectively, in the quantum dots' recombination of the ground state and first excited electron-hole pairs. The variation in size of the self-assembled quantum dots is shown by the width of each band. The hole emission spectrum, in contrast to the wide emission bands of the quantum dot array, displays distinct lines that span the spontaneous quantum dot emission band as the ratio of the nanohole radius to the lattice constant rises. The quality factor of the hole restricts the linewidth of the modes, which increases with the quality factor ratio of 131. 95. As shown in Figure 2, the mode intensity increases as the cavity modes enter into resonance with the majority of the quantum dots, i. e., near the peak position of the quasiGaussian band.

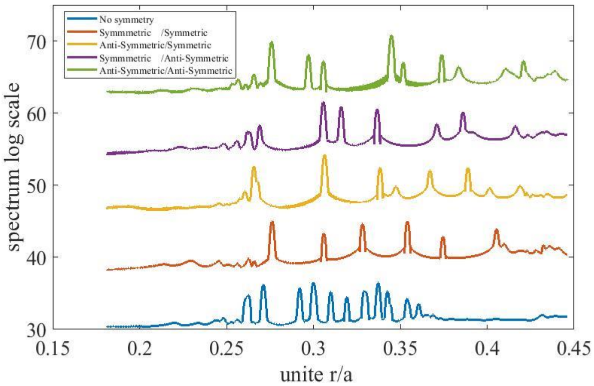

Fig.2. The Gaussian emission spectrum plot as a function of radius to lattice constant.

To enhance optical pumping within a waveguide made of aluminum gallium arsenide, quantum dots are positioned in the gallium interlayer. Additionally, aluminum oxide functions as a dielectric layer with a refractive index of 1.75, serving as a low refractive index material to confine the field for the gain medium.

As shown in Fig.3, the gallium arsenate gain material has a high refractive index of 3. 4. The effect of indium arsenic zinc oxide and gallium arsenate in increasing the confinement intensity of the gain medium is also determined by their quality factor in Fig.4, which is maximized at a frequency of 212 THz.

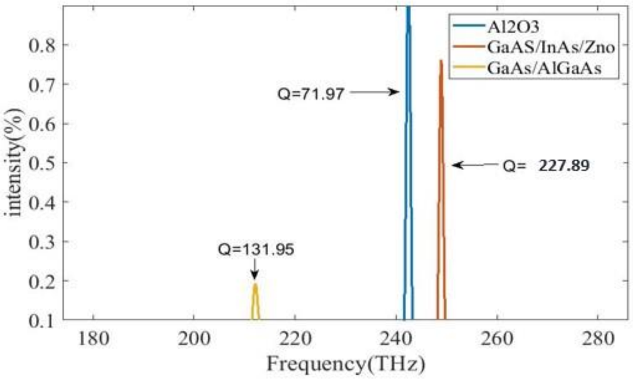

Fig.3.The emission intensity as a function of frequency, spanning from 180 to 280 terahertz, within a hybrid gain medium.

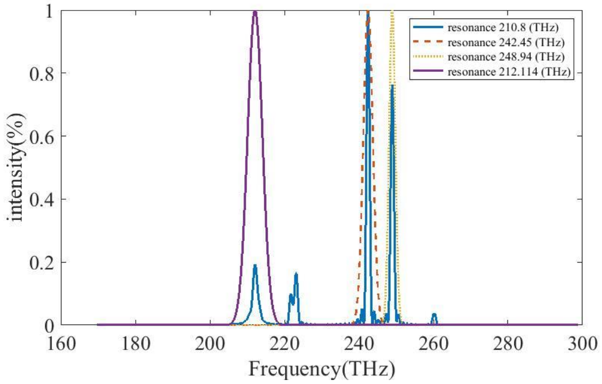

Fig.4. Emission intensity vs. frequency in the range of 180 to 280 terahertz.

The only well-defined current injection window identified is region I, as illustrated in Fig.5. The figure displays the curves for quantum dots with lattice constants of 366nm, along with injection apertures of 60 μm and 40 μm at a temperature of 10°C.

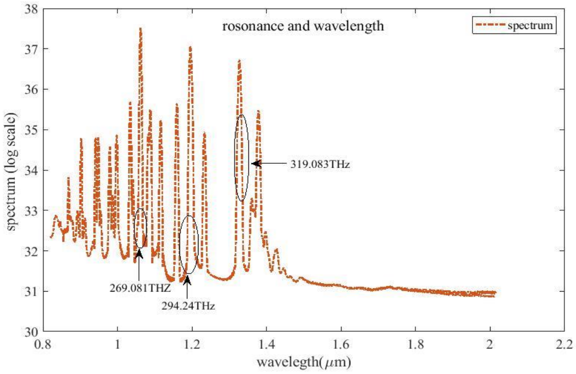

Fig 5. The Euler spectrum, which peaks at 212 terahertz, is shown in the graph.

In Fig.6, the parameter is presented. The current confinement provided by the gallium arsenide and zinc oxide layers leads to a decrease in the threshold current by around 0. 25 mA, even though there is an increase in the threshold current density. The device with a 0. 1-micrometer injection aperture did not exhibit a reduction in threshold current. The observed increase in threshold current density is linked to the discrepancy between the gain spectra and the limitations set by the photonic crystals. Furthermore, the current density tends to rise with increasing temperature.

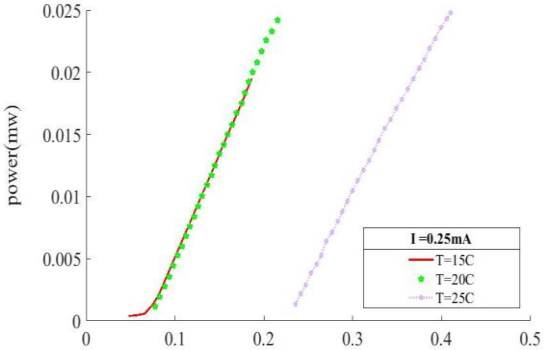

Fig.6. The output gain curve of a photonic crystal laser with current excitation in a gallium arsenic and zinc oxide gain environment as a function of temperature fluctuations.

Absorption is one of the most important factors determining the threshold, efficiency, linewidth, and output stability. Because nanolasers have very small dimensions, even a small amount of absorption can significantly change the optical and quantum behavior of the laser. Increasing absorption in the active material reduces the Q-factor, which in turn increases the optical pumping threshold. The effect of material absorption is examined in Fig.6, The results show that the use of the aluminum gallium arsenic/gallium arsenic material combination shows a lower absorption of 70% compared to the gallium arsenic/indium arsenic/zinc oxide material combination. In a similar vein, the indium arsenide quantum dot material's absorption impact has been examined in isolation throughout the wavelength range of 0. 5 to 1600 nm. The quality was evaluated by measuring the absorption at 1000 nm, yielding a result of 0. 8%, as demonstrated in Fig.7, The amount of light trapped in this area is estimated to be 1455. 3 times the factor. The variations in the gain environment are depicted in Fig.8, Zinc oxide, indium arsenic, and aluminum dioxide coatings have all been examined. The aluminum dioxide layer has a lower peak than the variations in time with the field intensity, and it is nearly identical for all of them: the indium, arsenic, and zinc oxide layers.

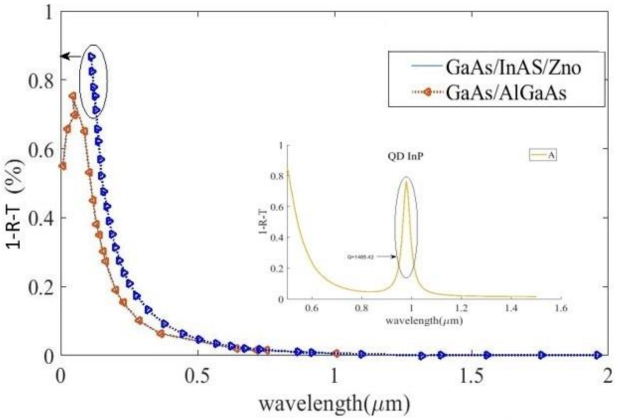

Fig.7.Absorption diagram of active hybrid materials in photonic crystal lasers in wavelength of 1000 nm.

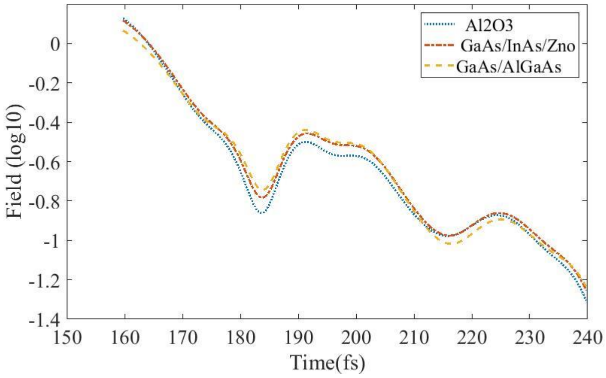

Fig.8. The curve shows the field versus time in the range of 1509 to 240 femtoseconds.

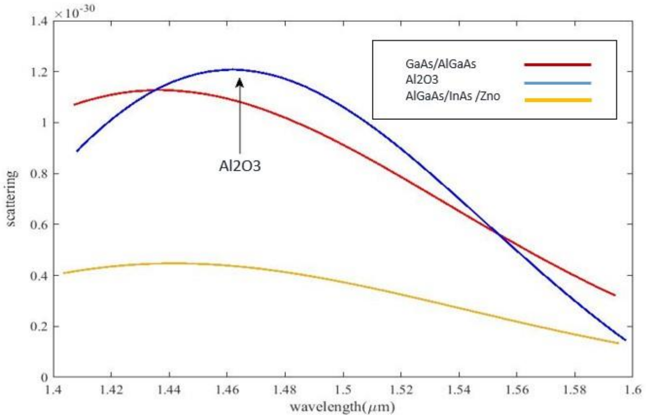

Fig.9. Scattering diagram of hybrid materials of photonic crystal lasers.

In Fig.9, Laser dispersion can depend on the threshold and quality factor of the laser. The dispersion diagram of the active hybrid materials of the photonic crystal laser shows that the combination of aluminum gallium arsenid material and indium arsenic quantum material/zinc oxide shows a 40% lower dispersion compared to the gallium arsenid/aluminum gallium arsenid material. Since the reduction in dispersion is inversely proportional to the quality factor, therefore, the reduction in dispersion increases the quality factor. This feature is effective in reducing the threshold of the photonic crystal laser. The gain and transmission of the active hybrid materials in the photonic crystal laser are examined below. The Fig.10, orange curve is the transmission at frequencies from 180 to 260 THz. The transmission value at around 200 THz is 0.8. As the frequency increases, the transmission of the material decreases. This behavior is related to the absorption frequency part of the active material. At lower frequencies, the absorption is low and the transmission is high near the band edge or resonance, and the absorption is high and the transmission is low. For the gain on the right side of the graph, a very sharp peak is seen. The peak value reaches about 0.99 (approximately 1). At a certain frequency, the gain grows suddenly. Then it drops back to near zero. This peak indicates the density of optical states at a frequency of 240 THz. There is a high-quality resonance mode (High-Q mode).

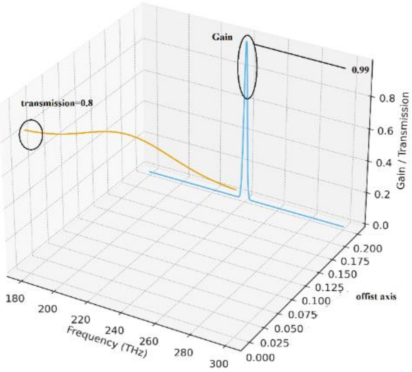

Fig 10. Gain and transmission graph of photonic crystal nano laser versus frequency in the THz range.

Apodization allows the removal of effects that occur near the beginning and/or end of the simulation from the Fourier transform of the monitors. This feature can be useful for filtering out short-term transients that occur when the system is excited by a dipole source and when studying high-Q systems that decay very slowly. Monitor apodization Fig.11, A applies a window function to the simulation fields before the monitor performs its Fourier transform of E(t) to obtain E(w). This allows the calculation of E(w) from a portion of the time signal. Start apodization can be used to ignore all transients that occur near the beginning of the simulation.

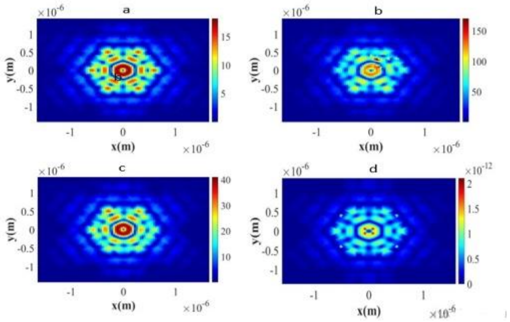

Fig.11. Mode profile of photonic crystals. A) In the state without apodization. B) In apodization. C) Apodization with its effect eliminated at the starting point. D) Apodization with its effect eliminated at the ending point.

V. LASER-BASED OPTIMIZATION OF QUANTUM LOGIC GATES

Recently, nanolasers have been used to control qubits due to their low power, frequency stability, and on-chip integration [21]. Nanolasers are challenging to couple with photonic qubits or other qubits (e.g., atomic or quantum dots) to provide high-quality photons or modulated light; coupling, losses, noise, and fabrication uniformity are complex. Long-term stability, environmental interference, and engineering issues (operating temperature, precise modulation, integration with other quantum components) are still serious obstacles [22]. A Gaussian laser pulse is added as an input (drive) to the quantum circuit. The Gaussian pulse (which has a unitary effect on the qubit) is obtained with a Unitary gate extracted from the pulse model. The Python software qiskit library is used for modeling. The Gaussian laser pulse is equated to a Unitary gate. This gate acts just like a "laser drive" on the qubit. This is the way Qiskit can model "light" or "laser".

Gaussian laser pulse is added as an input (drive) to the quantum circuit. The Gaussian pulse, which has a unitary effect on the qubit, is obtained with a Unitary gate extracted from the pulse model. The Python software qiskit library is used for modeling. The Gaussian laser pulse is equated to a Unitary gate. This gate acts just like a “laser drive” on the qubit. This is how Qiskit can model “light” or “laser”. Next, the laser is driven by a 3-qubit cont circuit. Since the use of laser beams in quantum circuits for angle control, and rotation. The schematic of the 3-qubit quantum circuit is shown in Fig.12.

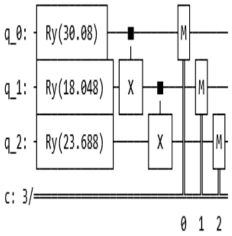

```
Counts: {'000': 608, '011': 265, '111': 370, '110': 99, '001': 90, '100': 462, '010': 102, '101': 52}
```

Fig.12. Three qubit CNOT quantum circuit with a Gaussian laser pulse.

The results on angle control and rotation are shown in Fig.13, As can be seen, the Gaussian pulse Q0 has the largest area and therefore the largest angle RY. Q1 has a shorter and shorter pulse, so the rotation angle is smaller. Q2 is located between these two. Pulse area → angle Rotation → The probability of superposition changes in the state |0⟩ and |1⟩. Table 1 also shows the results for each qubit. Table I. Investigation of the parameters of the elevation area and the rotation angle of each qubit with the Gaussian laser pulse.

TABLE I

The parameters of the laser

Qubit	***Omega0***	***Sigma***	***wavelength***	***With, Height***
0	1.2	10	Distinct peak, average width	Maximum area → maximum rotation angle
1	0.9	8	Shorter peak and lower	average rotation angle
2	1.05	9	Between Q0 and Q1	medium-high rotation angle

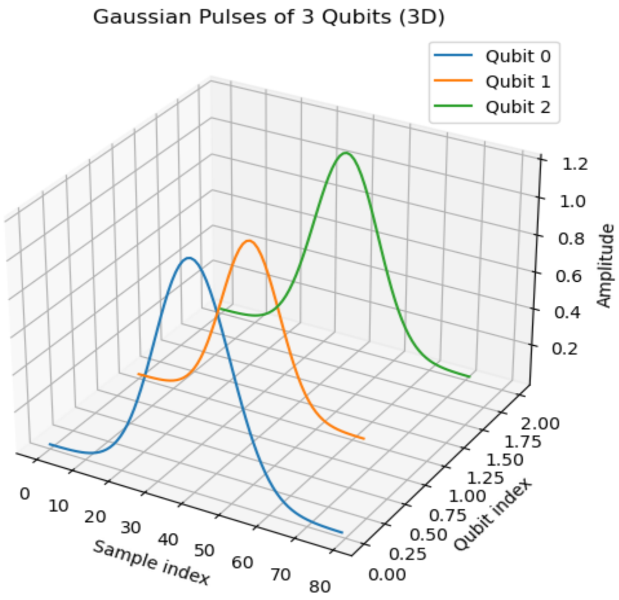

Fig.13.Gaussian wavelet plot for each qubit.

In Fig.14, the |000⟩ state has the highest probability (long column + light color) → indicates that most qubits were still close to |0⟩ before CNOT. The |111⟩ state has a significant probability indicates the CNOT chain effect that correlates Q0, Q1, and Q2. Intermediate states such as |001⟩, |010⟩, |101⟩ are less frequently observed. The combination of the RY angle and the CNOT effect makes the distribution non-uniform. The color of the columns is determined by the probability: columns with higher probability are brighter or warmer, and columns with lower probability are darker. The angle θ of each qubit is taken from the area of the Gaussian pulse: θ = Ω0 * σ * √(2π) Q0, with the largest θ → more likely to change → directly affect Q1 and Q2 via CNOT. Q1 and Q2 have intermediate angles → less likely to superpose → asymmetric probability distribution. Thus, the column |111⟩ indicates the generation of entanglement, since CNOT makes the qubits dependent.

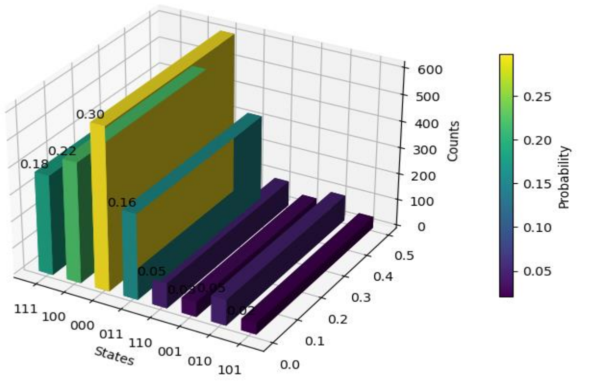

Fig.14. Probability density of qubits correlation with the Gaussian distribution.

These conditions have been routinely achieved in both cold-atom and thermal-vapor platforms, where strong dipole–dipole interactions and well-resolved EIT features have been reported. Previous studies have also demonstrated stable optical phase control and interaction-mediated nonlinearities at comparable Rydberg excitation densities, confirming that the interaction strengths and coherence times required for our scheme are already experimentally accessible. Taken together, these established capabilities indicate that the proposed approach is feasible with current technology and amenable to near-term experimental realization.

Despite the robustness to decoherence demonstrated in this work, several limitations remain. First, the system retains a degree of sensitivity to photon-loss channels, which may become more pronounced under strong driving conditions or in ultra-compact cavity geometries. Second, phase-matching requirements can impose constraints on efficient light–matter coupling, particularly when nonlinear processes or multi-mode interactions are involved. Finally, the scalability of atomic-hole and defect-based gain media is still restricted by fabrication uniformity, spectral inhomogeneity, and integration challenges at the wafer level. Addressing these issues will be essential for transitioning the proposed platform toward large-scale and fully integrated photonic architectures. Finally, the comparison table is provided as Table II.

TABLE II
The Comparison table

Ref.	Material	Q	Structure	Feature	Application
[24]	InAs/InP	>100	PhC	High-Q cavity,	quantum communication and networking
[25]	Optofluidic	200<	Ring resonator	High sensitivity	Quantum sensor
[26]	InAs/InGaAs	-	Quantum dot	Tunable power	Optical switching devices
[27]	InAs/GaAs	100<	SOA	Low power	Logical devices
This Work	Indium arsenide	227.98	PhC	High-Q cavity, strong light-matter interaction	Quantum logic gate
This Work	Aluminium oxide	131.95	PhC	Moderate Q in hybrid gain medium	Quantum logic gate

VI. CONCLUSION

In this paper, the hybrid gain medium of quantum dot photonic crystal nanolaser in the increase of the pumping of the var with aluminum oxide, zinc oxide, and gallium arsenide materials has been investigated, and the degree of confinement of the var with a quality factor of 227.89 for the indium arsenic layer and 122.26 has been obtained. Also, increasing the radius variation with a lattice constant rate of 0.37 increases the spontaneous emission, and the linewidth of the modes is limited by the quality factor of the hole. The photonic crystal laser beam is driven into the logic gates of the 3-qubit quantum CNOT circuit, and the results are measured in terms of angle and rotation variations and their probability function for quantum laser application. The Gaussian pulse Q0 has the largest area and therefore the largest RY angle. Q1 has a shorter and shorter pulse; the rotation angle is smaller. Q2 is between these two. Pulse area rotation angle superposition probability changes in the $|0\rangle$ and $|1\rangle$ states.

FUNDING STATEMENT

There was no Funding.

CONFLICTS OF INTEREST

All data is available upon reasonable request from the corresponding authors.

AUTHORS CONTRIBUTION STATEMENT

Anis Omidniaee: Conceptualization; Formal Analysis. Ali Farmani: Numerical Implementation; Theoretical Validation. Anis Omidniaee: Writing and Design of the Manuscript.

AI DISCLOSURE

The authors have not used Generative AI.

DATA AVAILABILITY

All data generated or analyzed during this study are included in this published article.

REFERENCES

[1] Q. Zhang, Y. Fu, Y. Zhang, J. Xing, and H. Zhang, "Halide perovskite semiconductor lasers: Materials, cavity design, and low threshold," Nano Letters, vol. 21, no. 5, pp. 1903–1914, 2021.

[2] Y. Jiao, T. Fujii, and T. Baba, "InP membrane integrated photonics research," Semiconductor Science and Technology, vol. 36, no. 1, p. 013001, 2020.

[3] K. Takeda, T. Fujii, K. Nozaki, and T. Baba, "Optical links on silicon photonic chips using ultralow-power consumption photonic-crystal lasers," Optics Express, vol. 29, no. 16, pp. 26082–26092, 2021.

[4] T. Tomiyasu, K. Takeda, K. Nozaki, and T. Baba, "20-Gbit/s direct modulation of GaInAsP/InP membrane distributed-reflector laser with energy cost of less than 100 fJ/bit," Applied Physics Express, vol. 11, no. 1, p. 012704, 2017.

[5] T. Aihara, K. Takeda, K. Nozaki, and T. Baba, "Heterogeneously integrated widely tunable laser using lattice filter and ring resonator on Si photonics platform," Optics Express, vol. 30, no. 10, pp. 15820–15829, 2022.

[6] Z. Wang, Y. Liang, K. Takeda, K. Nozaki, and T. Baba, "Continuous-wave operation of 1550 nm low-threshold triple-lattice photonic-crystal surface-emitting lasers," Light: Science & Applications, vol. 13, no. 1, p. 44, 2024.

[7] T.-Y. Lee, H. Lee, and H. Jeon, "Colloidal-quantum-dot nanolaser oscillating at a bound-state-in-the-continuum with planar surface topography for a high Q-factor," Nanophotonics, vol. 14, no. 10, pp. 1645–1652, 2025.

[8] Y. Wang, Z. Wang, K. Takeda, and T. Baba, "Large-angle twisted photonic crystal semiconductor nanolasers with ultra-low thresholds operating in the C-band," arXiv preprint, arXiv:2411.14772, 2024.

[9] E. Dimopoulos, K. Takeda, K. Nozaki, and T. Baba, "Electrically-driven photonic crystal lasers with ultra-low threshold," Laser & Photonics Reviews, vol. 16, no. 11, p. 2200109, 2022.

[10] P. Dhingra, A. W. Bett, and G. Tränkle, "Low-threshold visible InP quantum dot and InGaP quantum well lasers grown by molecular beam epitaxy," Journal of Applied Physics, vol. 133, no. 10, p. 103101, 2023.

[11] H. Jia, Y. Wang, Z. Wang, and T. Baba, "Low threshold InAs/InP quantum dot lasers on Si," in Proc. IEEE Silicon Photonics Conf. (SiPhotonics), 2025.

[12] P. Wang, Y. Liang, Z. Wang, K. Takeda, and T. Baba, "Room temperature CW operation of 1.3 μm quantum dot triple-lattice photonic crystal surface-emitting lasers with buried structure," Optics Express, vol. 33, no. 13, pp. 27429–27437, 2025.

[13] N. Taghipour, M. R. Biondi, S. Hoogland, and E. H. Sargent,"Low-threshold, highly stable colloidal quantum dot short-wave infrared laser enabled by suppression of trap-assisted Auger recombination," Advanced Materials, vol. 34, no. 3, p. 2107532, 2022.

[14] L. Yun, Y. Zhang, H. Liu, and J. Wang, "Low threshold and high power fiber laser passively mode-locked based on PbSe quantum dots," IEEE Photonics Technology Letters, vol. 36, no. 4, pp. 247–250, 2024.

[15] Y. Tan, J. Lim, Z. Wang, and H. Yang, "Low-threshold surface-emitting colloidal quantum-dot circular Bragg laser array," Light: Science & Applications, vol. 14, no. 1, p. 36, 2025.

[16] H. Zhong, Y. Liang, Z. Wang, and T. Baba, Ultra-low threshold continuous-wave quantum dot mini-BIC lasers,"Light: Science & Applications, vol. 12, no. 1, p. 100, 2023.

[17] J. Liu, A. J. Bennett, and D. J. P. Ellis, "Single self-assembled InAs/GaAs quantum dots in photonic nanostructures: The role of nanofabrication," Physical Review Applied, vol. 9, no. 6, p. 064019, 2018.

[18] C.-W. Shih, Y. Chen, H. Lin, and S. Chang,"Self-aligned photonic defect microcavity lasers with site-controlled quantum dots,"Laser & Photonics Reviews, vol. 18, no. 7, p. 2301242, 2024.

[19] M. Yoshida, K. De Greve, K. Ishibashi, and S. Noda, "High-brightness scalable continuous-wave single-mode photonic-crystal laser," Nature, vol. 618, no. 7966, pp. 727–732, 2023.

[20] S. Yan, Y. Zhang, H. Zhong, and X. Liu,"Cavity quantum electrodynamics with moiré photonic crystal nanocavity,"Nature Communications, vol. 16, no. 1, pp. 1–8, 2025.

[21] S. Pechprasarn, S. Sasivimolkul, and P. Suvarnaphaet, "Fabry–Perot resonance in 2D dielectric grating for figure of merit enhancement in refractive index sensing," Sensors, vol. 21, no. 15, p. 4958, 2021.

[22] S. Rodt and S. Reitzenstein, "Integrated nanophotonics for the development of fully functional quantum circuits based on on-demand single-photon emitters,"APL Photonics, vol. 6, no. 1, 2021.

[23] C. Shang, Y. Wan, Z. Wang, and J. Yao, "Perspectives on advances in quantum dot lasers and integration with Si photonic integrated circuits," ACS Photonics, vol. 8, no. 9, pp. 2555–2566, 2021.

[24] C. L. Phillips, A. J. Brash, M. Godsland, N. J. Martin, A. Foster, A. Tomlinson, R. Dost, N. Babazadeh, E. M. Sala, L. Wilson, and J. Heffernan, "Purcell-enhanced single photons at telecom wavelengths from a quantum dot in a photonic crystal cavity," Scientific Reports, vol. 14, no. 1, p. 4450, 2024.

[25] M. H. Mozaffari and A. Farmani, "On-chip single-mode optofluidic microresonator dye laser sensor," IEEE Sensors Journal, vol. 20, no. 7, pp. 3556–3563, 2019.

[26] M. Heydari, A. R. Zali, R. E. Gildeh, and A. Farmani, "Fully integrated, 80 GHz bandwidth, 1.3 μm InAs/InGaAs CW-PW quantum dot passively colliding-pulse mode-locked (CPM) lasers for IR sensing application," IEEE Sensors Journal, vol. 22, no. 7, pp. 6528–6535, 2022.

[27] A. Farmani, M. Farhang, and M. H. Sheikhi, "High-performance polarization-independent quantum dot semiconductor optical amplifier with 22 dB fiber-to-fiber gain using mode propagation tuning without additional polarization controller," Optics & Laser Technology, vol. 93, pp. 127–132, 2017.

BIOGRAPHIES

Ali Farmani is an Associate Professor from Lorestan University. The author has contributed to research in the topics: Advanced nano-opto-electronics. His interests mainly focus on fabrication, modeling, simulation, and characterization of Electronic, Photonic, and Plasmonic based Nanostructure devices, as well as the study of the state-of-the-art fields such as logical devices, optical storage devices, plasmonic devices, particularly in the terahertz to infrared region and advanced theoretical concepts related to two dimensional materials such as graphene and silicene and using FDTD.

Anis Omidniaee is a PhD Student from Lorestan University. The author has contributed to research in topics Advanced optoelectronics. Her interests mainly focus on Photonic and Plasmonic-based Nanostructure devices as well as the study of state-of-the-art fields such as quantum logical devices, optical devices, and plasmonic devices.